AIX-MARSEILLE UNIVERSITY

THESIS

submitted and defended in view of obtaining the degree of

DOCTOR OF AIX-MARSEILLE UNIVERSITY

Discipline: Material Science, Physics, Chemistry and Nanoscience
Doctoral School: Physics and Material Science

By

Déborah Fernand

Thesis defense: December 18th, 2014

POROUS NANOCOMPOSITES BASED OF METAL NANOPARTICLES: FROM SYNTHESIS TOWARDS APPLICATIONS IN THE FIELD OF ADSORPTION

Supervisor: Dr. Virginie Hornebecq
Co-supervisor: Dr. Philip Llewellyn

JURY

Pr. (full)	Bogdan Kuchta	Aix-Marseille University	President
Pr. (associate)	Vladimir Zeleňák	Pavol Jozef Šafárik University	Reviewer
Dr.	Alexandre Merlen	University of South, Toulon-Var	Reviewer
Dr.	Renaud Denoyel	Aix-Marseille University	Examiner
Dr.	Bénédicte Prélot	University of Montpellier II	Examiner
Dr.	Virginie Hornebecq	Aix-Marseille University	Ph.D. supervisor

I

thank God

for guiding me

a little bit more every day.

Dedicated to
Mum and Dad.

Acknowledgements

First of all, I would like to thank Philippe Knauth and Renaud Denoyel, former and current director of the Laboratoire MADIREL[*], for giving me the opportunity to carry out my Ph.D. work under their roof. I would further like to thank Philip Llewellyn who allowed me to work in his S2G[†] group.

I would like to express my gratitude to my supervisor Virginie Hornebecq for supervising my work, guiding me during these three years of Ph.D. and for giving me the opportunity to take part to several national and international workshops. I would really like to thank her for her patience, her availability, for the fruitful and stimulating discussions, and for correcting my writings. I really appreciated the freedom I was given.

I would further like to thank the members of the jury in addition to my supervisor: Bogdan Kuchta, Vladimir Zeleňák, Alexandre Merlen, Renaud Denoyel and Bénédicte Prélot for allowing me to defend my work on this day and for all the beneficial comments and for their interest in my work.

I feel grateful to Trang Phan (ICR[‡]) for the synthesis of block copolymers, to David Bergé-Lefranc (IMBE[§]) for making the calorimetric measurements in liquid phase, Carine Chassigneux (MADIREL) for performing the XRD measurements, to Martiane Cabié (CP2M[**]) for taking the TEM images, to Alain Tonetto (PRATIM[††]) for taking the SEM images, to Florence Chaspoul (IMBE) for the ICP-MS measurements, to Corine Reibel (ICG[‡‡]) for the magnetic properties experiments and to Philip Llewellyn for performing the calorimetric experiments in gas phase.

I am particularly indebted to Cédric Pardanaud (PIIM[§§]) for his help and for conveying me his knowledge about Raman spectroscopy during this work. I also kindly thank Grégory Giacometti for helping me also for some Raman spectroscopy experiments.

---

[*] MADIREL: Matériaux Divisés, Revêtements, Électrocéramique, Marseille.
[†] S2G: Séparation et Stockage de Gaz, Laboratoire MADIREL, Marseille.
[‡] ICR: Institut de Chimie Radicalaire, Equipe CROPS (Chimie Radicalaire Organique et Polymères de Spécialité), Marseille.
[§] IMBE : Institut Méditerranéen de Biodiversité et d'Ecologie marine et continentale, Marseille.
[**] CP2M: Centre Pluridisciplinaire de Microscopie électronique et de Microanalyse, Marseille.
[††] PRATIM: Plateforme de recherche analytique, technologique et imagerie, Fédération des Sciences Chimiques de Marseille, Marseille.
[‡‡] ICG: Institut Charles Gerhardt, Montpellier.
[§§] PIIM : Physique des Interactions Ioniques et Moléculaires, Marseille.

I extend my sincere thanks to all the members, staff of MADIREL for their welcome and moments passed here: Chrystelle, Sandrine, Marielle, Florence, Maryline, Vanessa, Bogdan, Dominique, Yvan, Pascal and all the others I haven't mentioned.

Great thanks to the Ph.D. students of MADIREL and other laboratories for their warm company, particularly Achouak, Marine, Brunella, Nareerat, Abir, Agnieszka, Astrid, Marco, Ali, Tracy, Luca, Hilal, Abdelaziz, Nicolas, Pierre-Henri and also to the other trainees that I met during my stay – Samia, Nora, Wafa, Naïma, Shabnam, Garima, Pierre, Alexander, etc. – for all the good times of entertainment during my stay in Marseille.

I would like to thank all my friends from French Guiana, Martinica, Marseille, and so on, for all the support they gave me. I am thinking particularly about Maryse (Mymyse), Leïla (Lilou), Nayenka (Nayou), Jessica (Jess), Nathalie (Natty), Laury (Laulau), Jessie (Jessie-Jess), Jessie (Jess), Fabienne (Fabby), Yasmine (Yas), Fatima (Toupit), Loubna, Damia and all the others I forgot to mention.

I would like also to thank all my relatives in French Guiana, Martinica and France that encouraged me since the beginning and forever: Mamie Georgette, all my aunts Marie-Jeanne, Lucile, Nelly, Elizabeth, Lucie, Marie-France, Lina and others, all my uncles Jean-Louis, Claude and others, my cousins Roxanne (Zinezine), Johan, Michella, and so on (you are so many!).

A special thank to Jean-Philippe, my sweetheart, for his understanding, his patience and for enduring my stress and yet encouraging me especially these last months.

Last but not least, my greatest thanks are to my family Papa, Maman, Giovanni and Luigi for their invaluable support since the beginning of this adventure, you encouraged me from so far away at any time and this was really important for me. Thanks so much!

Table of contents

Introduction

Introduction

A porous material can be defined by three intrinsic characteristics [1]: a tridimensional framework, pores (with different shapes: spherical, tubular, ink-bottle, and so on) and an internal surface as shown in **Figure Intro.1**. The framework presents physical properties (from thermal, electrical, magnetic, optical, mechanical, etc. origin) as well as chemical properties (acid-base nature, electric charge) inherent to its nature. The internal surface gives rise to various catalytic and adsorption properties. These specific properties are even more interesting as the internal surface is large. Besides, this internal surface can be functionalized with specific chemical groups. In addition, the volume constituted by the pores can be used as a tank for trapping of molecules. This free volume can also be used as a chemical nano-reactor for the insertion of size-controlled nano-objects in order to functionalize the material, which is then called 'nanocomposite'.

Porous materials gave rise to a worldwide investigation owing to their potential applications in various material based research fields such as adsorption technology [2–4], molecular separation [5,6], catalysis [7,8], filtration [9], electronics [10], optics [11,12], gas sensing [13,14], drug delivery [15,16], templating [17,18], etc. Designing of organized, uniformly sized and shaped pore texture combined with specific functionalities in porous compounds at the nanoscale has expanded greatly since it brings additional benefits generating optimization of performances.

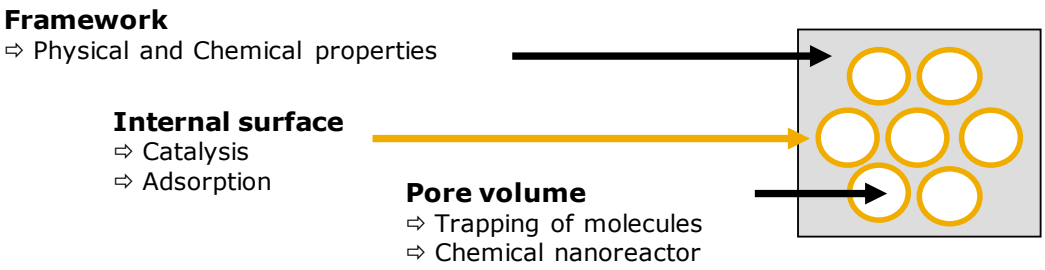

Figure Intro.1: General characteristics of porous solids and the related principal properties. Adapted from reference [1].

In this context, this thesis will focus on the study of porous materials, combining high specific surface area and functionalization with metal nanoparticles, by targeting mainly two applications in the field of adsorption: the first one in the liquid phase and the other one in the gas phase.

The first application is related to the detection of molecules in the liquid phase at low concentrations. Indeed, the development of a detection method that is simple and fast is a major challenge in the medical and pharmaceutical fields because current methods are proving to be quite complex and time consuming. Among the different techniques available, one possibility for this purpose is the detection by surface enhanced Raman scattering (SERS); indeed the reported exaltation factors are expected to exceed the limits of detection. Generally, studies are focused essentially on the Raman response of a molecule towards a substrate for the SERS effect, but adsorbed amounts and Raman response are rarely studied simultaneously. Therefore, the aim is to study different porous substrates functionalized with noble metal nanoparticles, i.e. silver and gold, by coupling thermodynamics and Raman spectroscopy. Several parameters will be varied in order to highlight the characteristics of SERS effect and the parameters that permit decrease of the detection threshold.

The second application is related to the storage of hydrogen. Although hydrogen is a promising energy vector in the current energy context, technological and scientific key issues still must be overcome in order to achieve efficient storage in high surface area materials. The reversibility of the storage is one of the major challenges. Indeed, the hydrogen and the material must have specific interactions leading to not only large adsorbed amounts of gas but also to a desorption that is not too expensive from an energetic point of view. In this context, porous materials functionalized with transition metal nanoparticles, i.e. nickel, will be studied. Indeed, transition metals are reported to develop the specific interactions with hydrogen that are mentioned above. The hydrogen adsorption properties at low temperature and low pressure of the nanocomposites will be investigated by coupling adsorption manometry and microcalorimetry allowing the determination of the adsorbed amounts and the related energies of interaction.

This thesis is thus divided into three main chapters which are described as follows:

Chapter 1 will present primarily a general review on the synthesis of ordered porous materials through soft-templating routes. It is especially focused on porous silica and carbon materials. Then, the synthesis procedures and characterization of the porous silicas and carbon prepared during this work using block copolymers as structure directing agents will be presented.

In Chapter 2, the study of nanocomposites for the sensing of low-dose molecules using Raman spectroscopy will be presented. These porous nanocomposites are based on a mesoporous silica matrix in which nanoparticles of noble metals are inserted; they are denoted as $Ag@SiO_2$ and $Au@SiO_2$. The synthesis procedure of these nanocomposites will first be described, followed by details of their characterization. Then, the detection properties of these different samples towards a model molecule, the rhodamine 6G (R6G), will be examined for initial concentration

ranging from $1\,10^{-4}$ M to $1\,10^{-7}$ M. The influence of the presence of metal particles and the chemical nature of the metal on detection properties will be presented and discussed. Finally, the influence of the solvent, the excitation wavelength and the chosen model molecule will be introduced.

Further in Chapter 3, nanocomposites for the storage of hydrogen will be investigated. The establishment of an appropriate method of reduction of nickel is an important step in this work and will be presented. Then, synthesis procedures and characterization of the nanocomposites based of mesoporous silica and carbon matrices in which nickel nanoparticles are incorporated, namely Ni@SiO_2 and Ni@Carbon, will be developed. Finally, the hydrogen adsorption properties of the different materials will be presented and discussed.

General conclusions summarizing the main results of this work will be given and perspectives for future work will be proposed.

References

[1] G. Férey, L'actualité chimique, 304 (2007) III.

[2] W.J. Son, J.S. Choi, W.S. Ahn, *Micropor. Mesopor. Mater.*, 113 (2008) 31.

[3] J.W. Wei, J.J. Shi, H. Pan, W. Zhao, et al., *Micropor. Mesopor. Mater.*, 116 (2008) 394.

[4] C. Knöfel, C. Martin, V. Hornebecq, P.L. Llewellyn, *J. Phys. Chem. C*, 113 (2009) 21726.

[5] A. Katiyar, N.G. Pinto, *Small*, 2 (2006) 644.

[6] L.H. Chen, G.S. Zhu, D.L. Zhang, et al., *J. Mater. Chem.*, 19 (2009) 2013.

[7] A. Corma, *Chem. Rev.*, 97 (1997) 2373.

[8] A. Taguchi, F. Schuth, *Micropor. Mesopor. Mater.*, 77 (2005) 1.

[9] M.A. Alvin, T.E. Lippert, J.E. Lane, *Am. Ceram. Soc. Bull.*, 70 (1991) 1491.

[10] C.G. Wu, T. Bein, *Science*, 264 (1994) 1757.

[11] G. Wirnsberger, P.D. Yang, B.J. Scott, et al., *Spectroc. Acta Pt. A-Molec. Biomolec. Spectr.*, 57 (2001) 2049.

[12] L.N. Sun, H.J. Zhang, C.Y. Peng, et al, *J. Phys. Chem. B*, 110 (2006) 7249.

[13] T. Yamada, H.S. Zhou, H. Uchida, et al., *Micropor. Mesopor. Mater.*, 54 (2002) 269.

[14] T. Yamada, H.S. Zhou, H. Uchida, et al., *J. Phys. Chem. B*, 108 *(*2004) 13341.

[15] Y.F. Zhu, J.L. Shi, W.H. Shen, et al., *Angew. Chem.-Int. Edit.*, 44 (2005) 5083.

[16] M. Vallet-Regi, F. Balas, D. Arcos, *Angew. Chem.-Int. Edit.*, 46 (2007) 7548.

[17] Y.J. Han, J.M. Kim, G.D. Stucky, *Chem. Mater.*, 12 (2000) 2068.

[18] Y.Y. Wu, T. Livneh, Y.X. Zhang, et al., *Nano Lett.*, 4 (2004) 2337.

Chapter 1

Synthesis of micro-/mesoporous materials via soft-templating routes

Table of contents

Chapter 1: Synthesis of micro-/mesoporous materials via soft-templating routes

In literature, two different approaches are available for preparation of nanostructured porous materials: the **soft-templating** and the **hard-templating** approach. The term soft-templating, also known as *endotemplating*, refers to a synthesis procedure that uses, surfactants (derived from '*surf*ace-*act*ive *a*g*ents*'), which at a specific stage, as *structure directing agents*, form *lyotropic liquid crystalline phases* in order to obtain porosity; this pathway will be described in the following text. In contrast, the term hard-templating, known as *exotemplating* or *nanocasting*, refers to a synthesis procedure in which a rigid mold with a specific porous structure in the nanometer scale is used. In the latter, the void of the mold is first filled with a precursor of the desired material to be molded – obviously a mold that does not chemically react with the precursor is preferable – then subsequent in situ processing is applied and afterwards the mold is removed by a specific treatment. [1] The resulting material has a reversed molded shape: it is the negative replica of the hard template parent used. A large variety of replica materials can be tailored according to the structure of the hard template parent. [2] Nanostructured porous solids such as silica or carbon materials are generally used as hard templates; they can be easily removed by chemical (diluted hydrofluoric acid HF or concentrated sodium hydroxide NaOH etching for silica) or thermal (combustion under an oxidizing atmosphere for carbon) treatments – evidently the final replica must be stable during the treatment used for the template removal.

The aim of this chapter is to give some background information on the synthesis of porous silica and carbon materials via soft-templating routes. Firstly, a detailed presentation of the soft-templating concept will be given including the mechanism principle, and the origin and role of the structure-directing agents. Then the synthesis procedures for obtaining porous silica and carbon materials via soft-templating routes will be presented.

I.1. State of the art

I.1.1. The soft-templating concept

The preparation of micro-/mesoporous materials, including silica, non-siliceous and carbon materials [3,4], based on the so-called soft-templating route, relies on the self-assembly of *structure directing agents* – surfactant molecules – and the building of the desired network using inorganic, organic (or hybrid) *precursors*. Basically, the synthesis occurs as follows: a polymerization mechanism sensitive to synthesis conditions allows precursors to form an in-/organic (or hybrid) network around the templates generated by the structure-directing agent.

This polymeric network is commonly called the hybrid mesostructure. A simplified pathway is schematically presented in **Figure 1.1**.

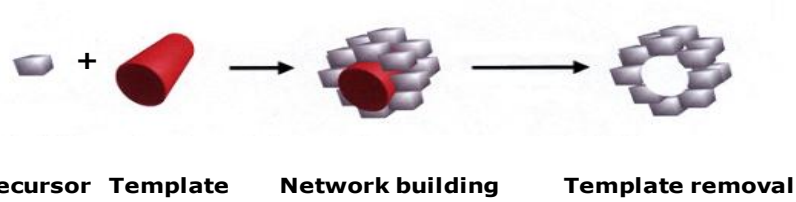

Figure 1.1: Simplified schematic representation of micro-/mesoporous material formation via a surfactant-templated polymerization.

Two different mechanisms are considered to be involved in the surfactant-templated polymerization leading to formation of the hybrid mesostructure. [4,5] The first one assumes mesostructure around which the 'polymerization' will occur. The second one assumes a cooperative self-assembly between the surfactant molecules and the precursors of interest during the network building.

In order to obtain the desired organization for the final hybrid mesostructure, it is important to take into account three fundamental types of interactions [1,6]: (i) the (in-)organic-(in-)organic precursor interactions that govern the network formation, (ii) the surfactant-surfactant interactions that influence the micellization process, and finally (iii) the in-/organic precursor-surfactant interactions that direct the organization of the hybrid phase. Furthermore, the molecular structure and organization of the surfactant template in the corresponding solvents should also be considered. Employing ternary (or more) phase diagrams, combining the solvent and the co-solvent, is then crucial to understand their behavior and will help predicting the different possible phases according to the concentration of these different components. [6,7]

Finally, the organized porous structure of the materials is obtained after removal of the templates. This last step can be achieved via different methods including thermal treatment [8–10], specific solvent extraction [11–14], supercritical fluids extraction [15–17], Soxhlet extraction [18,19], microwave digestion [20–22], photocalcination [23] and soon.

I.1.2. Structure directing agent: surfactant, micellization, lyotropic liquid crystalline phase and pore size tuning.

I.1.2.a. Preliminary definition

The structure directing agents are amphiphilic surfactant molecules that possess both hydrophilic (polar) and hydrophobic (non-polar) groups. The hydrophilic group is generally named as head, the hydrophobic one as tail with a hydrocarbon composition. The first has a

strong attraction for the solvent (water) while the other one has neither repulsion nor attraction towards the solvent. [7,24,25]

The surfactants can be classified according to the charge (or lack of charge) of their hydrophilic head group. Three main groups can be identified: the *ionic* surfactants that can be categorized into two types the *cationic* and the *anionic* ones, the *non-ionic* surfactants and the *amphoteric* surfactants (also known as *zwitterionic*) that possess both anionic and cationic groups in their head moiety. [7,24,25] The surfactants generally used for the synthesis of mesoporous materials are either ionic or non-ionic:

- The cationic surfactants. As their name indicates, the cationic surfactants possess a positively charged hydrophilic part and an anion counterpart. They are essentially cationic alkyltrimethylammonium, e.g. the alkyltrimethylammonium halides.
- The anionic surfactants. In opposition with the cationic ones, the anionic surfactants possess a negatively charged hydrophilic part and a cation counterpart. They are mainly anionic alkylsulfonates or alkylphosphates.
- The non-ionic surfactants are neutral. They can be divided into three main types: the oligomeric alkyl-poly(ethylene oxide) surfactants, the alkylamine surfactants and finally the block copolymer surfactants. The block copolymer surfactants can be diblock, triblock or multiblock copolymers. Generally, the hydrophobic blocks used are poly(propylene oxide) (PPO), polystyrene (PS) or polybutadiene (PB), and the hydrophilic block is usually poly(ethylene oxide) (PEO).

I.1.2.b. Micellization

Above a certain concentration known as the *critical micellar concentration (CMC)*, surfactant molecules tend to self-assemble in solution into small aggregates called *micelles*. [7,24–27] The micelle formation leads to the separation of the two incompatible aqueous and organic phases.

The micellization phenomenon is driven by a balance between hydrophobic and hydrophilic effects. The hydrophobic effect is attributed to the non-polar tail attraction that causes the micelle formation: this attraction is actually mainly due to a compromise between the strong attractive forces in-between water molecules (forces arising from the presence of these non-polar tails) and the strong affinity of the polar head to water; the 'tail-to-tail' interactions having a minor contribution to this effect. The hydrophilic effect is due to the electrostatic and steric repulsion of the polar head groups that work in the opposite sense. [26–30].

Besides, two micelle configurations can be encountered: either the *direct* or the *inverse* one. In the direct configuration, the polar solvent is a continuous medium while the non-polar solvent is

confined inside the isolated micelles: the non-polar tails are directed inside the micelles. Contrarily, in the inverse one, exactly the reverse occurs: the polar solvent is confined in closed regions and the non-polar solvent is the continuous medium, the non-polar tails pointing outward towards the latter. A single representation of a surfactant molecule and of direct and inverse micelles is presented in **Figure 1.2**.

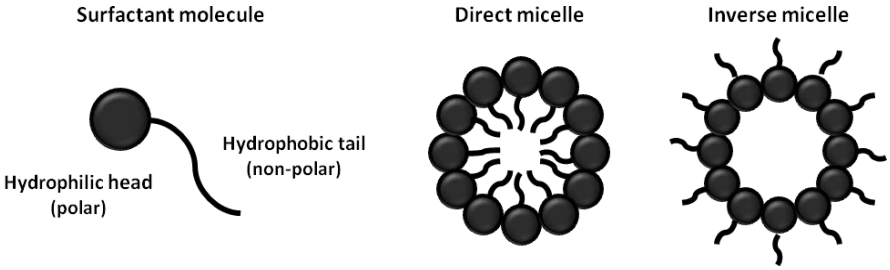

Figure 1.2: Simplified schemes of a surfactant molecule and direct and inverse micelles in a polar (aqueous) solution.

Furthermore, different classes of micellar phase structures [4], permitting the coexistence of the aqueous and organic phases, can be distinguished, as shown on **Figure 1.3**: the spherical (*A*) and cylindrical (*B*) direct micellar phases, the planar bilayer phase (*C*, known as 'lamellae'), the reverse micellar phase (*D,* here only the spherical phase is represented), and the liposomes (*F*, solvent-containing bilayers). Other more complex arrangements such as the sponge-like bicontinuous phase (*E,* continuous solvent-containing bilayers) are possible. Generally, the most interesting ones for the synthesis of porous materials are the direct micellar phases (A and B) and the bicontinuous phase (E).

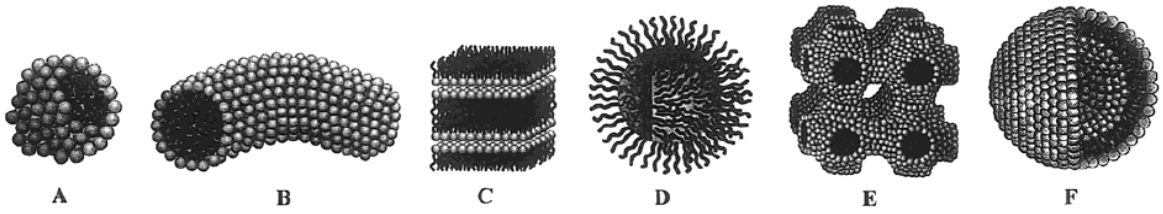

Figure 1.3: Schemes of typical micellar phase structures. [4]

I.1.2.c. Lyotropic liquid crystalline phase formation

A typical feature of surfactant molecules is that, upon increasing surfactant concentration and prevailing conditions (temperature, pH), they do not only form micellar solution but also since the distance between the formed micelles decreases the latter tend to form specific ordered arrangements called *lyotropic liquid crystalline phases* by aggregation in the solution. In the liquid crystals, the basic units display orientational order and even positional order along some directions. [26,31,32] However, the formation of the liquid crystalline structure strongly

depends on the conditions of the solution such as temperature, concentration and pH-value. [4–7,26,32]

Furthermore, with regard to the surfactant concentration, we can theoretically observe the formation of different arrays according to the following phase transition sequence [31]: a cubic array I_1 of spherical micelles, a cylindrical hexagonal array H_1, a bicontinuous cubic array V_1, a lamellar array L_α and the reverse arrays V_2, H_2 and I_2, **Figure 1.4**. Additional intermediate mesophases, for instance rectangular (or ribbon-phases), rhombohedral, tetragonal, monoclinic and orthorhombic phases can be formed between the lamellar phase and the direct and reverse cylindrical phases. [6,33–43]

However, all these structures are not necessarily present in the surfactant phase diagrams. The concepts of the thermodynamics, the interaction energies and the packing constraints of the surfactant molecules combined together allow understanding and determining the possibility that specific liquid crystalline phases can be formed. [28,29,44,45] Indeed, the formation of a specific liquid crystal depends not only on the geometry of the surfactant micelles but also on the interactions at the in-/organic precursor-surfactant interface [4]. Therefore, knowledge of size, charge and shape of the surfactant are essential structure determining parameters [4,44,46].

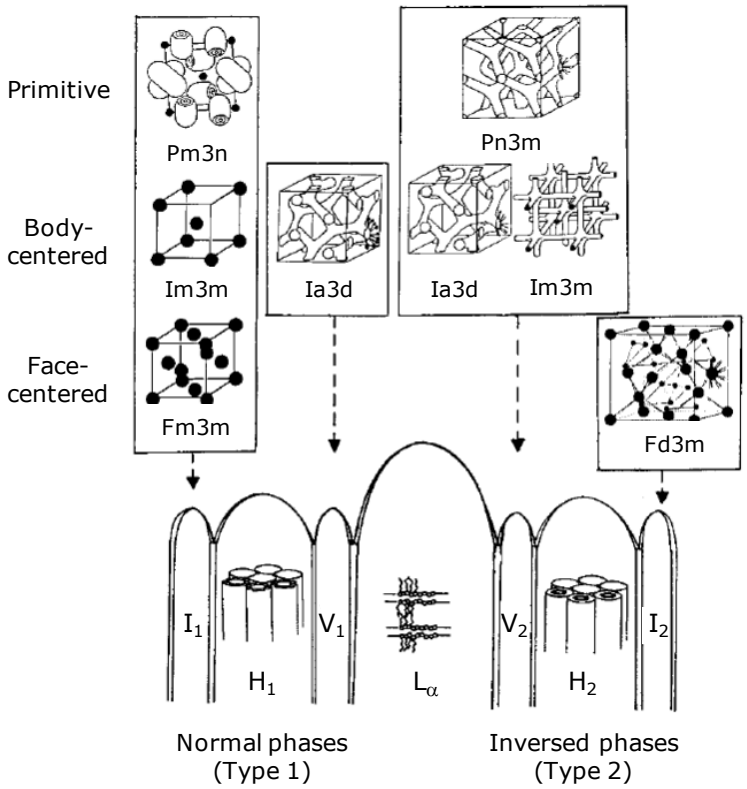

Figure 1.4: Schemes of the principal lyotropic liquid crystalline arrays with increasing concentration from left to right. [31]

The theory of packing constraints is a physical concept that gives rise to a simple model based on the idea of minimizing the interfacial curvature energy for a given micellar structure and thus allows predicting the mesostructure of the liquid crystalline phase by considering what is called the *effective packing parameter g*, **Equation 1.1**. [29,44,47]

Equation 1.1

$$g = \frac{V}{a_0 \times l}$$

Where: g is the effective packing parameter

V is the volume of the surfactant hydrophobic tail(s)

a_0 is the effective optimal surface area of the surfactant hydrophilic head group at the hydrophilic-hydrophobic interface

l is the chain length *o*f the surfactant hydrophobic tail(s)

To ensure the tail fluidity, l must be lower than the maximum chain length l_c. The latter can be estimated knowing the number of carbon atoms in the hydrocarbon tail. The smaller is the g value, the bigger is the micelle interface curvature, leading to spheres. The micellar isotropic phases are labeled L_1 and L_2, for direct and inverse configurations respectively. The micelles will tend to form a cubic I_1 or Hexagonal 3D (hexagonal close packing) array. As the g value increases, the micelle interface curvature decreases: the micelles will tend to form successively cylindrical hexagonal H_1, bicontinuous cubic V_1 (or Intermediate) and lamellar L_α arrays. When g is bigger than one, the micelles will tend to form inverse arrays. The expected mesostructures of the liquid crystalline phase as a function of the g parameter [29,41,45,46] are presented in **Table 1.1**. In analogy with the tendency developed earlier in **Figure 1.4**, a homologous consistent correlation is observed between the effective packing parameter g and the liquid crystalline phase changes.

Table 1.1: Expected micellar phase structures and their corresponding liquid crystalline phase arrays as a function of the critical effective packing parameter. [4,29,45,46]

g	Micellar phase structures	Liquid crystalline phase array
< 1/3	Spherical micelles	Cubic I_1 or Hexagonal 3D
1/3–1/2	Cylindrical micelles	Hexagonal 2D H_1
1/2–1	Bicontinuous (or Intermediate) phases	Cubic V_1 or (Intermediate)
1	Planar bilayers	Lamellar L_α
>1	Inverses	Inverse

I.1.2.d. Pore size tuning

Here is presented a non-exhaustive summary of the different strategies available in order to tailor the porosity of the matrices obtained. Indeed, fine-tuning of the pore size for different materials could be achieved by varying one or more of the synthesis parameters. Adjustment of the reaction medium composition is one strategy: e.g. modulation of the starting materials concentration ratio for instance surfactant/matrix precursor(s) [48] or precursor/precursor ratio [49,50]; changes in the composition of the surfactant for instance by using surfactant with higher molecular weight [51–53] or by adjusting the chain length of the surfactant [54–56]; use of additive expanders so-called swelling agents [57–59] (these are hydrophobic organic molecules interacting with the micelle core resulting in an increase of the size of the latter [59]); or addition of solvent that act as co-surfactant inducing an increase in pore size by 'co-micellizing' with the surfactant [60,61]. Variation of the processing parameters is another interesting strategy that can be used during the synthesis: e.g. modification of the pH by addition of acid or base; higher temperatures and/or longer reaction time. [62–64]

I.2. Synthesis of silica matrices

Over the last two past decades, tremendous work has been carried out on the preparation and characterization of ordered mesoporous silica materials. These porous materials were commonly synthesized following the *sol-gel* chemistry. Indeed this process presents several advantages concerning the synthesis conditions of what is called the *soft chemistry* such as low temperatures, low pressures and low energies [65] and thus allows obtaining high degree of purity and stoichiometry of the resulting materials. Moreover combined with the knowledge of self-assembly mechanism of the liquid crystalline phases (cf. *Section I.1.*), this relatively simple process permits the use of different kinds of precursors and structure directing agents. In this way, a large variety of mesoporous silica materials with numerous pore shape structure and size have been synthesized.

During this work, two types of mesoporous silica have been synthesized. The first is a SBA-16–type silica based on the work of Stucky et al. The second was prepared using laboratory-made amphiphilic poly(ethylene oxide)-*b*-polystyrene (PEO-*b*-PS) diblock copolymer as structure directing agent according to a previous work reported by this group; this silica was named SEO (for **S**tyrene **E**thylene **O**xide).

I.2.1. General synthesis procedure

I.2.1.a. Sol-gel chemistry [66]

The formation of silica materials through the sol-gel route involves the controlled *hydrolysis* and *condensation* of a soluble source of silica in an aqueous solution leading to what is called a *sol*. A sol is a homogeneous suspension of submicroscopic solid particles in a liquid.

The sol-gel process is highly pH-dependent; it is frequent to use an acid or base catalyst during the synthesis according to the desired final product morphology (particles, fibers, thin films, bulk gels, etc.). Generally basic catalysis yields in highly condensed *particulate* sol: colloidal particles can be obtained. Whilst the acid one yields a weakly cross-linked *polymeric* sol, the sol particles grow and condense forming a continuous polymeric network containing trapped solvent which is called a *gel*: thin films or bulk gels can be obtained. The overall process will be described in the followings.

The silica source is an important factor for the reaction conditions. Popular silica precursors are alkoxysilanes ($Si(OR)_4$ where R is an alkyl) because they react readily with water. The most common ones are tetramethoxysilane ($Si(OCH_3)_4$) and tetraethoxysilane ($Si(OC_2H_5)_4$), also known as tetramethyl orthosilicate and tetraethyl orthosilicate and abbreviated in the literature as TMOS and TEOS respectively. It is worth noting that water and alkoxysilanes are immiscible, the use of a co-solvent acting as homogenizing agent, such as alcohol for instance, is then necessary.

As stated before, the first step of the polymerization is the formation of silanol groups by hydrolysis of the silica alkoxide precursor in the aqueous solution as follows:

$$Si(OR)_4 + H_2O \rightarrow HO\text{-}Si\text{-}(OR)_3 + ROH$$

During this reaction, water is consumed and alcohol is formed. Depending on the amount of water and catalyst present, the hydrolysis may go to completion (so that all the alkoxide groups OR are replaced by hydroxyl groups OH):

$$Si(OR)_4 + 4\ H_2O \rightarrow Si(OH)_4 + 4\ ROH$$

Or stop while the silicon is only partially hydrolyzed:

$$Si(OR)_4 + 4\ H_2O \rightarrow (OR)_{4-n}\text{-}Si\text{-}(OH)_n \quad (n<4)$$

The next step of the polymerization is the link of two partially hydrolyzed molecules together through water- or alcohol-producing condensations (oxolations or alcoxolations). Under most conditions, condensation starts before hydrolysis is complete. The condensation reaction of two

silanol groups (•Si-OH) yields to the release of one water molecule while that of one silanol group with one alkoxysilane group (•Si-OR) results in the formation of one alcohol molecule. These two condensation reactions lead to the creation of a siloxane bond (Si-O-Si):

$(OR)_3$-Si-OH + HO-Si-$(OR)_3$ → $(OR)_3$-Si-O-Si-$(OR)_3$ + H_2O (Release of water)

$(OR)_3$-Si-OH + RO-Si-$(OR)_3$ → $(OR)_3$-Si-O-Si-$(OR)_3$ + ROH (Release of alcohol)

This type of reactions can continue to build larger silica network resulting in the formation of a viscous gel. The next step to gelation is ageing (during which the rigidity of the gel increases due to supplementary condensation reactions) and then syneresis (spontaneous shrinkage during solvent evaporation) leading to cracking of the gel.

I.2.1.b. Self-assembly synergy [4]

As mentioned previously, the formation of the ordered mesoporous silica materials through the soft-templating route arises from the self-assembly of the structure directing agents with the silica precursors. The hybrid mesostructure formation step strongly depends on the type of surfactant-precursor interactions. Different attempts have been proposed to understand this synergy according to the type of surfactant used.

In the case of ionic surfactants, these interactions are generally of electrostatic origin. Whatever the ionic surfactant type (anionic or cationic), in the simplest case, the surfactant and silica precursor are of opposite charges in the synthesis conditions. If a cationic surfactant is used, the silica synthesis should be performed in basic medium (pH significantly higher than the isoelectric point of silica (pH $>>$ 2) to ensure negatively charged silica. Contrarily, if an anionic surfactant is used, the silica synthesis should be performed in acidic medium (pH $<$ 2) in order to have positively charged silica. The corresponding interactions are denoted as S^+I^- and S^-I^+ respectively, and are described as *direct* interaction mechanisms. In the usual nomenclature for mesostructured materials, *S* stands for the surfactant template and I^- for the inorganic species. Two additional *indirect* counterion-mediated interaction mechanisms [67] are available if surfactant and silica precursor are of similar charges. The counterion (X^- or M^+) acts as a charge compensating species. X^- stands for halogenide anions and M^+ stands for alkaline cations. The corresponding interaction mechanisms are denoted as $S^+X^-I^+$ and $S^-M^+I^-$.

In the case of non-ionic surfactants, the interactions are mainly governed by H-bonding or are of dipolar type. Several attempts are proposed depending on the synthesis conditions. If the synthesis is performed at the isoelectric point of silica (pH $\sim 2-3$), the corresponding interaction mechanism is denoted as S^0I^0. If the synthesis is performed in acidic medium

(pH < 2), the interaction mechanism is denoted as $S^0H^+X^-I^+$ [68], where: S^0H^+ is the neutral surfactant in interaction with a hydronium ion, or in a simplified notation $S^0X^-I^+$. However, there seems to be an abuse of terminology when supposing neutral silica species 'I^0' when pH > 2. Besides, in neutral medium (pH = 7), one should note that the silica is negatively charged although the negative charge remains low [59].

I.2.1.c. Milestones

Different milestones families of mesoporous silica can be found in the literature. A brief overview of the pioneering ones, focused on the structure directing agents used and the final pore structure obtained, is given here:

- The M41S- or MCM-family – from **M**obile **C**omposition of **M**atter – was the first family of ordered silica materials to be obtained in the mesoscopic range. Cationic quaternary ammonium surfactants were used and two-dimensional (2D) hexagonal, three-dimensional (3D) cubic and lamellar symmetries were obtained for MCM-41 [69], MCM-48 (bicontinuous) and MCM-50 respectively [57,70,71].
- The FSM-family – from **F**olded **S**heet **M**esoporous materials-n – appeared at about the same period also as highly ordered mesoporous silicas. The number n in FSM-n depends on the length of the surfactant alkyl chain. Cationic alkyltrimethylammonium surfactants were used and hexagonal symmetry was obtained for FSM-16. [72]
- The HMS-family [73] and MSU-family [74] – from **H**exagonal **M**esoporous **S**ilica and **M**ichigan **S**tate **U**niversity – were the first families of porous silica materials to be synthesized with non-ionic surfactants: alkylamines, oligomeric alkyl-poly(ethylene oxide) and block copolymer surfactants. However these materials displayed short-range order hexagonal and worm-like disordered structures, respectively. Some years later, by optimizing the synthesis conditions, disorder in some MSU-X materials has been overcome leading to hexagonal structure. [75]
- The KIT-family [76] – from **K**orea Advanced **I**nstitute of Science and **T**echnology: the KIT-1 materials synthesized using cationic surfactants, hexadecyltrimethylammonium chloride, presented disordered 3D worm-like pore structure. Later, ordered structures were obtained KIT-5, KIT-6.
- The SBA-family [11,77] – from **S**anta **B**arbara **A**morphous materials – regroups well ordered mesoporous silica materials obtained with non-ionic surfactants, more precisely oligomeric poly(alkylene oxide) and di- and triblock copolymer surfactants. Several materials were derived with various symmetries including 3D cubic, 3D hexagonal, 2D hexagonal and lamellar: e.g. SBA-11, SBA-12, SBA-15 [77] and SBA-16.

I.2.2. Synthesis procedure of SBA-16–type silica

The SBA-16–type mesoporous silica synthesized within this work was carried out via the sol-gel route, at room temperature and in acidic conditions according to the procedure described by Stucky et al. but slightly modified.

The source of silica was tetramethoxysilane (TMOS – $Si(OCH_3)_4$) and the structure directing agent was Pluronic F127 ($PEO_{106}PPO_{70}PEO_{106}$). The solvent and co-solvent were respectively distilled water (H_2O) prepared-in-house and butan-2-ol (or *sec*-Butanol, ButOH – $CH_3CH(OH)CH_2CH_3$). The latter is mainly located at the hydrophilic-hydrophobic interface stabilizing the micellar aggregates of the template [78]. The Pluronic F127 is a non-ionic surfactant, therefore in order to reach the isoelectric point of silica the pH was set to 2. Besides, the acidity of the medium will favor condensation in the ending chains leading to the formation of a polymeric gel. This phenomenon is known as acid catalysis of the polymerization as explained earlier. The acid medium was created using hydrochloric acid (HCl) at 0.01 M.

SBA-16 was synthesized according to the literature [79]. The mass ratio between the starting materials was set to 1 : 0.44 : 0.19 : 0.69 [TMOS : Pluronic F127 : ButOH : HCl]. The silica precursor TMOS was diluted in the butan-2-ol under soft stirring. The hydrochloric acid was added once a monophase was formed. Finally, the Pluronic F127 was added to the homogeneous resulting mixture under vigorous stirring in order to avoid flocculation. The stirring was continued until a colorless gel was formed. The gelation process takes $\sim 2-3$ h to occur and once the gel point was reached the viscous gel was solidified. The latter was aged for one week in air at room temperature. Afterwards, the as-prepared transparent gel was thermally treated in air in order to remove the structure directing agent. The final SBA-16 silica material was obtained as a white powder.

I.2.3. Synthesis procedure of SEO–type silica

The SEO–type mesoporous silica synthesized within this work was also carried out via the sol-gel route in acidic conditions according to a procedure previously reported in this group [56].

The source of silica was tetramethoxysilane (TMOS – $Si(OCH_3)_4$) and the structure directing agent was laboratory-made poly(ethylene oxide)-*b*-polystyrene ($PEO_{114}PS_{48}$) diblock copolymer. The solvent and co-solvent were respectively distilled water (H_2O) and ethanol absolute anhydrous (EtOH – $CH_3CH_2(OH)$). The $PEO_{114}PS_{48}$ is a non-ionic surfactant then the synthesis was performed at the isoelectric point of silica. The pH was set to 2 with hydrochloric acid (HCl) at 0.01 M.

SEO was synthesized with the following starting material mass ratio 1 : 0.5 : 3.5 : 0.5 [TMOS : $PEO_{114}PS_{48}$: EtOH : HCl]. The $PEO_{114}PS_{48}$ surfactant is hardly soluble ethanol due to the high molecular weight of the PS block, thus it was first gently dissolved in ethanol using an air blower set at 50°C then subsequently at 120°C up to bubbling in order to allow its dissolution. The complete solubilization of the copolymer was achieved once a monophase was formed under stirring at room temperature. Finally, the hydrochloric acid and the silica precursor TMOS were added in the homogeneous resulting mixture under vigorous stirring, a slightly yellowish mixture was obtained. The stirring was continued during the gelation process that lasts around two days until solidification occurred. The solid gel was aged for one week in air at room temperature. Afterwards, the as-prepared transparent gel was thermally treated in air in order to remove the structure directing agent. The final SEO matrix was obtained as a white powder.

I.2.4. Structure directing agent removal for as-synthesized SBA-16 and SEO–types silica materials

The as-synthesized SBA-16 and SEO–types silica gels were examined by thermogravimetric analysis (TGA) in order to determine the appropriated thermal treatment (calcination) programs for the template removal.

As shown in **Figure 1.5**, the TGA profiles of as-synthesized SBA-16 and SEO silica gels can be decomposed into several regions corresponding to different phenomena occurring during the thermal treatment.

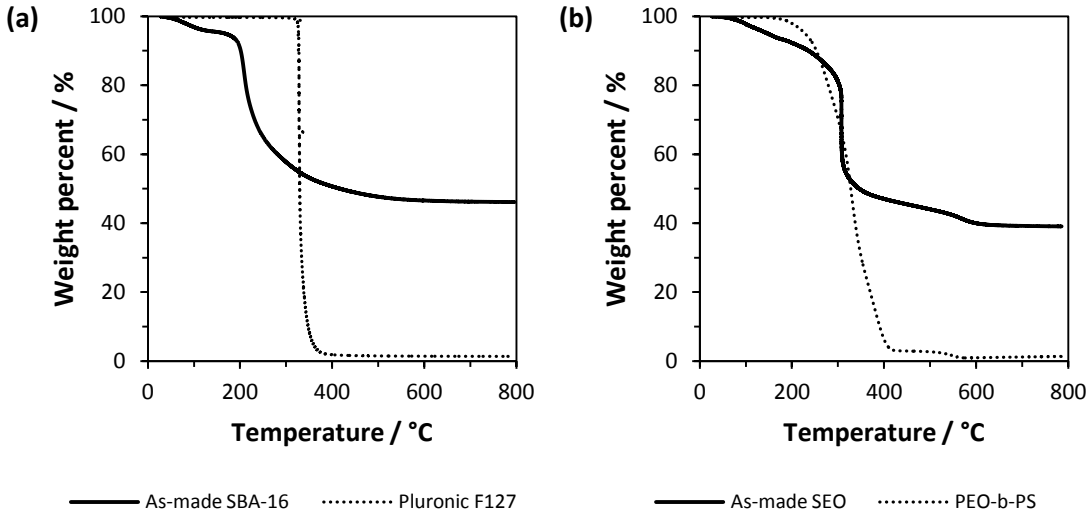

Figure 1.5: TGA profiles of as-synthesized SBA-16 (a) and SEO (b) silica gels and their structure directing agents Pluronic F127 and $PEO_{114}PS_{48}$, respectively.

For as-synthesized SBA-16 silica gel, four regions can be observed, **Figure 1.5 (a):** (i) the first one, from room temperature to 100°C, can be correlated to desorption of physisorbed species (water, alcohol), (ii) the second one, from 100°C to 200°C, is associated to removal of chemisorbed species (mainly water), (iii) the third one, from 200°C to 550°C, corresponds to the decomposition of organic species (unreacted silica precursor and template molecules), (iv) the fourth one, temperatures above 550°C, where there is negligible weight loss. Therefore, in order to eliminate the Pluronic F127 template, the following thermal procedure was applied**:** the sample was heated to 300°C using a heating rate of 150°C. h^{-1} and held at this temperature for 2 h, then it was heated to 550°C with a rate of 100°C. h^{-1} and maintained at this temperature during 7 h, finally it was cooled down to room temperature with a rate of 100°C. h^{-1} (**Figure 1.6 (a)**).

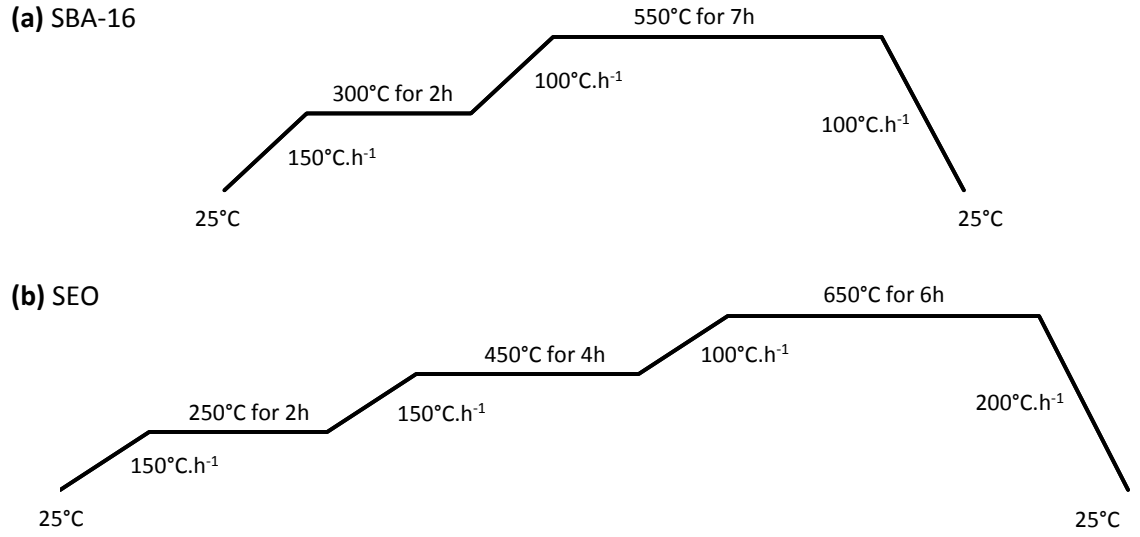

Figure 1.6: Calcination routes for removal of the template of SBA-16 (a) and SEO (b) silica gels.

Similarly, for as-synthesized SEO silica gel, five regions can be detected, **Figure 1.5 (b)**: (i) from room temperature to 100°C, physisorbed species are removed (water, alcohol), (ii) from 100°C to 250°C, chemisorbed species are desorbed (mainly water), (iii) from 250°C to 450°C, there is decomposition of organic species (unreacted silica precursor and template molecules), (iv) from 450°C to 650°C, there is residual organic species (template molecules) decomposition, (v) above 650°C, there is negligible weight loss. Therefore, in order to eliminate the $PEO_{114}PS_{48}$ template, the following thermal procedure was applied: the sample was heated to 250°C then subsequently to 450°C and held at these temperatures for 2 h and 4 h respectively, using a heating rate of 150°C. h^{-1}, then it was heated to 650°C with a rate of 100°C. h^{-1} and maintained at this temperature during 6 h, finally it was cooled down to room temperature with a rate of 200°C. h^{-1} (**Figure 1.6 (b)**).

I.2.5. Characterization of porous SBA-16 and SEO−types silica matrices

The textural properties of the calcined SBA-16 and SEO silica materials were investigated using nitrogen adsorption/desorption measurements at 77 K (**Figure 1.7**). The isotherms are characterized by an initial sharp uptake at relative pressures below 0.05 followed by a more gradual adsorption then a second sharp upswing between 0.5 and 0.7 for SBA-16 and between 0.7 and 0.8 for SEO. A final plateau ends the adsorption branch. According to the IUPAC, such isotherms are characterized as mixed type *I* and *IV,* which are attributed to samples containing both microporosity and rigid mesoporosity. [80] A hysteresis loop of type *H2* and *H1*, characteristic of adsorbent with ink-bottle shaped pores [81] (with narrow neck and wide body) are present for SBA-16 and SEO respectively. Indeed due to the smaller pore entries, the nitrogen molecules are not desorbed progressively being in a quasi-liquid state because of capillary condensation, but they are retained until a sudden desorption step originating from cavitation effect [82] occurs at relative pressures closed to 0.45 for SBA-16 and 0.5 for SEO. This indicates that the pore entries are smaller than 5 nm. For SEO silica matrix, an additional step is present in the desorption branch of the isotherm: this highlights the presence of two different pore neck sizes. The equivalent surface areas were calculated using BET method (the term 'equivalent' is used since the BET surface area is estimated including the presence of microporosity). The microporous and total pore volumes were determined by *t*-plot analysis. The mean pore size was derived from the adsorption branch using BJH method. The textural properties of the two silica matrices are summarized in **Table 1.2**.

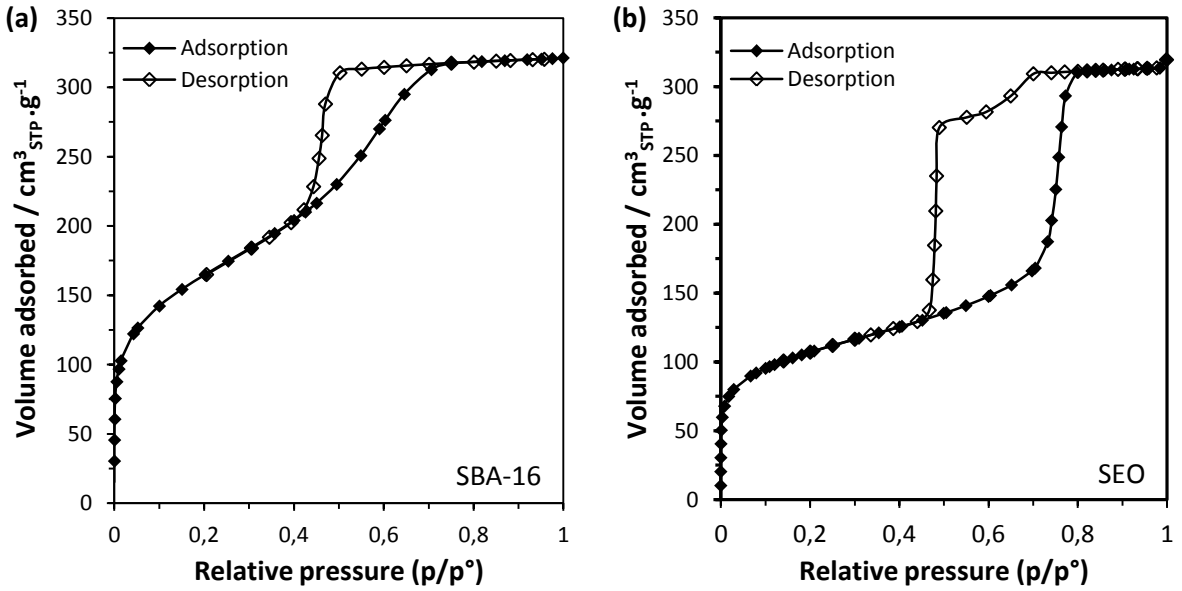

Figure 1.7: Nitrogen ad-/desorption isotherms at 77 K of SBA-16 (a) and SEO (b) silica matrices.

Table 1.2: Textural properties of SBA-16 and SEO silica matrices.

Sample	S_{BET} [a] $/m^2.g^{-1}$	$V_{\mu porous}$ [b] $/cm^3.g^{-1}$	$V_{total\ pore}$ [c] $/cm^3.g^{-1}$	D_{pore} [d] /nm
SBA-16	580	0.04	0.50	4.5
SEO	380	0.05	0.50	8.5

a BET surface area
b Microporous volume
c Total pore volume
d Pore size at the maxima of pore size distribution

Transmission electron microscopy permits the identification of the pore system organization and the pore size of the porous silica matrices. For SBA-16 silica, TEM images show a homogenous and ordered pore structure with little variation in size ($D_{pore} \sim 5$ nm), **Figure 1.8**. A 3D body centered cubic pore arrangement corresponding to the $Im\bar{3}m$ space group, characteristic of SBA-16 silica materials [11], has been previously evidenced by small angle X-ray scattering (SAXS) analysis [79(b)]. For SEO silica, TEM images show a homogenous and ordered pore structure with little variation in size ($D_{pore} \sim 8 - 9$ nm), **Figure 1.9**. A 3D primitive cubic pore arrangement corresponding to the $Pm\bar{3}m$ space group has been previously evidenced by SAXS [56].

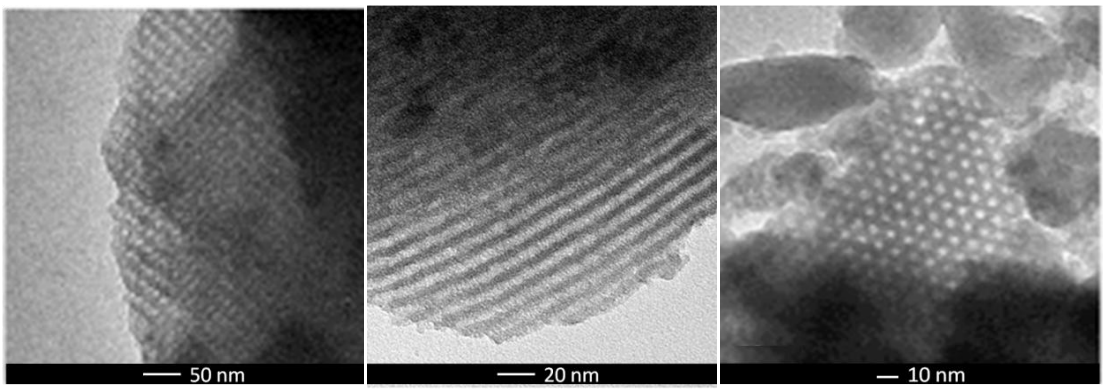

Figure 1.8: TEM images of porous silica SBA-16. TEM images from reference [79(b)].

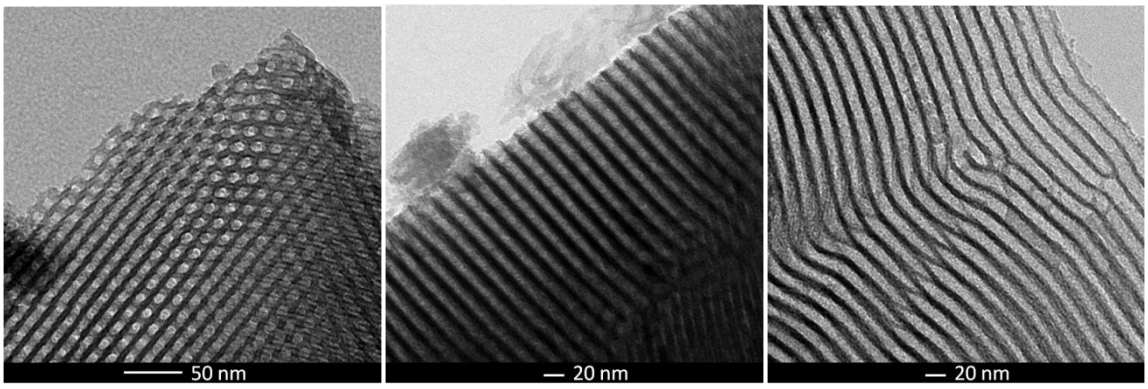

Figure 1.9: TEM images of porous silica SEO.

I.3. Synthesis of carbon matrices

I.3.1. Milestones

About a dozen years ago, the first successful syntheses of ordered bimodal micro-/mesoporous carbons was realized through the nanocasting strategy by using ordered MCM-48–type porous silicas (bicontinuous) as hard templates. The porous carbon structure was obtained by an infiltration of the porous silica mold with sucrose in acidic medium (sulfuric acid catalyst) [85] or phenol/formaldehyde resin [86] as carbon precursors, followed by their polymerization upon heat treatment and subsequent carbonization under inert atmosphere (leading to a carbon-silica composite) and finally removal of the template by hydrofluoric acid etching. The resulting carbon materials, named CMK-1 – from **C**arbon **M**esostructured by **K**orea Advanced Institute of Science and Technology – and SNU-1 were *not exact* negative replicas of the MCM-48 templates since they displayed symmetry somewhat lower. Indeed the pore architecture of MCM-48 consists of three-way intersection intertwined channel systems which are not interconnected. Thus, the silica removal leads to a gradient displacement of the resulting carbon sub-frameworks relative to each other and the resulting space group is $I4_1/a$ [87].

Shortly after, the first *exact* carbon negative replica was obtained using ordered SBA-15–type porous silica (2D hexagonal) and sucrose as hard template and carbon precursor respectively [88]. This carbon material, named CMK-3, consisted of uniformly sized interconnected linear carbon rods arranged in a 2D hexagonal pattern reflecting the parent silica matrix pore structure. Indeed the interconnecting intra-wall pores of SBA-15 properly filled with the carbon precursor acted as structure-supporting links between the carbon rods.

Afterwards, owing to the large variety of porous silicas available, different types of porous carbon materials possessing great diversity in pore system, connectivity, etc. could be prepared using diverse carbon sources in the presence of an appropriate catalyst. The carbon precursors supplied high carbon yield and stability (not thermally decomposable) during the carbonization step e.g. furfuryl alcohol, acenaphthene, polydivinylbenzene, acetylene, acrylonitrile, etc. and catalysts such as aluminum sites, oxalic acid, iron chloride, etc. were common. [89] The CMK-n–type negative carbon replicas were the most prominent.

Additionally, varying the filling degree of the carbon precursor, by controlling the synthesis conditions, gave rise to new carbon materials with different structure and texture. For instance, in case of solely coating the pore walls of SBA-15 and KIT-6 silica materials with a carbon layer rather than complete pore filling, ordered networks of hollow carbon tubes are obtained, namely CMK-5 [90] and CMK-9 [91], instead of CMK-3 [88] and CMK-8 [92] (similar to CMK-1 yet exact negative replica with interconnected structure) respectively. The porosity of these types of

materials arises from both the channel system inner part and the void originated from the silica templates.
For further details concerning ordered mesoporous carbon materials synthesized through hard templating pathway, a review from Lee et al. can be recommended. [93]

Since then, extensive research activity directed to the soft-templating concept were developed in order to find an alternative to the synthesis of porous carbon via hard-templating pathway as it is a time-consuming, laborious, costly, and thus industrially unfeasible method. However, the preparation of mesoporous carbon materials with ordered open pore structures was extremely difficult in solution by this time and remained challenging because of the high formation energy of C–C bonds. Therefore, the interactions between firstly both organic precursors and structure directing agents and secondly the organic precursors themselves (i.e. polymerization kinetics) should be considered in an organic-organic assembly for preparing ordered porous carbons with diversified structures [94–96], similarly to the inorganic-organic assembly in the preparation of the porous silica materials for instance. Moreover, the organic framework formed around the template easily collapsed upon the thermal treatment conducing to carbonization [97]. Consequently, significant research efforts have been undertaken to explore the different possibilities available in this area for a better understanding and control of the self-assembly process.

Based on the so-called solvent evaporation-induced self-assembly (EISA) strategy, the two first reported syntheses giving rise to ordered mesoporous carbons through direct self-assembly involved resorcinol and formaldehyde (RF) as carbon sources. In the first synthesis, the diblock copolymer polystyrene-*b*-poly(4-vinylpyridine) (PS-*b*-P4VP) was used as structure directing agent in a N,N'-dimethylformamide (DMF) medium; the carbons were prepared through a stepwise assembly approach: the resorcinol precursor was self-assembled with the template and then polymerized in situ with gaseous formaldehyde through a gas-solid reaction [98]. The second synthesis employed, under strong acidic conditions, the triblock copolymer Pluronic F127 ($PEO_{106}PPO_{70}PEO_{106}$) as surfactant and triethyl orthoacetate (EOA) was added as a carbon co-precursor [99]; the later seemed to stabilize the mesostructure, it might decrease the polymerization rate of resorcinol and formaldehyde and enhance the interaction between them and the surfactant templates [94,95,100]. The RF having many hydroxyl groups allowing hydrogen bonding interaction with the surfactant, the organic-organic self-assembly was driven by hydrogen bonding interaction with the surfactant hydrophilic moiety (P4VP [101] and PEO [102–104] respectively). Simple thermopolymerization at low temperatures (~100°C) was necessary before the template removal in order to create a rigid polymeric framework that will not collapse during pyrolysis. Upon thermal treatment under inert atmosphere, the mesoporous

carbon materials, obtained in the form of films, were generated directly with (in the first case) or subsequently to (in the second case) the removal of the templates and exhibited 2D hexagonal pore symmetry. The carbon obtained in the last synthesis was named COU-1 – referring to the **O**saka **U**niversity.

Not long after, using the EISA strategy under nearly neutral conditions, a novel family of FDU-n–type ordered porous carbon materials (films and powders) with diverse mesostructures emerged from the **F**u**d**an **U**niversity: C-FDU-14, C-FDU-15, C-FDU-16 [94,100], C-FDU-17 [105] and C-FDU-18 [106,107]. The carbon source was resol, a mixture of pre-polymerized phenol and formaldehyde (PF). Besides being cheaper than resorcinol, phenol has fewer and more inert reactive sites than those in resorcinol which implies lower polymerization rate due to fewer interactions in-between the polymer resin precursors [94]. Consequently, the assembly of phenolic resins and templates into ordered mesostructures is achieved more readily; notably, resol possesses a large number of hydroxyl groups (–OH) which can strongly interact with the templates via hydrogen-bonding [102,104]. The organic-organic self-assembly occurred during the preferential solvent evaporation. Amphiphilic PEO-*b*-PPO-*b*-PEO triblock copolymers were used as structure directing agents for the carbons C-FDU-n with $14 \leq n \leq 16$. The various carbon structures could be obtained by simply varying the phenol/template ratio and the PEO/PPO segment in the surfactants (i.e. Pluronic F127, Pluronic P123 $PEO_{20}PPO_{70}PEO_{20}$ and Pluronic F108 $PEO_{132}PPO_{50}PEO_{132}$). Amphiphilic reverse PPO-*b*-PEO-*b*-PPO ($PPO_{53}PEO_{136}PPO_{53}$) triblock copolymer was used as structure directing agent for the carbon C-FDU-17. Whilst for the carbons designated as C-FDU-18, amphiphilic poly(ethylene oxide)-*b*-polystyrene ($PEO_{125}PS_{230}$) or poly(ethylene oxide)-*b*-poly(methyl methacrylate) ($PEO_{125}PMMA_{144}$) diblock copolymers were used. As previously, thermopolymerization at low temperatures yielded to a rigid polymeric framework. The removal of surfactants and the subsequent carbonization were performed via thermal treatment under inert atmosphere.

A carbon film with a cubic pore symmetry (C-FDU-16) could be obtained using resorcinol-formaldehyde and Pluronic F108 in a non-aqueous basic solution and applying a direct carbonization in inert gas [95]; as mentioned before, the RF has many hydroxyl groups allowing hydrogen bonding interaction with the surfactant during the self-assembly [102,104], and thermopolymerization at low temperature was performed before template removal.

Besides, in the syntheses cited, shrinkage of the carbon structures could be observed during the pyrolysis resulting in small pore sizes and limited specific surface areas. A tri-constituent co-assembly strategy based on EISA approach has been developed to incorporate rigid components such as inorganic silicates into carbon frameworks in order to reduce the structural shrinkage [96,108]. Resols, pre-hydrolyzed TEOS and Pluronic F127 were used as organic and inorganic precursors and structure directing agent respectively. Resol and silicate oligomers

having plenty of hydroxyl groups could interact via hydrogen bonding interaction with the hydrophilic part of the surfactant as explained earlier. The thermopolymerization step was also present. The template removal and the subsequent carbonization were achieved under inert atmosphere. Further, silica removal was performed through hydrofluoric etching. The carbon powder obtained displayed a 2D hexagonal pore symmetry as for C-FDU-15 and reflected appreciable reduced shrinkage which implied larger pore size after template removal and carbonization as compared to the later. The rigid silicates acted as 'reinforcing-steel-bar' in the carbon structure and moreover caused the formation of small pores in the carbon framework which leaded to larger surface area than for C-FDU-15.

The EISA strategy, showing a multi-step pathway, has the advantage of dividing the cooperative self-assembly process into two: on the one hand the assembly of surfactants and on the other hand the polymerization of carbon precursors; this allows independent control of both processes. [109] Though this method is a considerable improvement as compared to the hard-templating one, it always involves the evaporation of organic solvent in large quantities and the products are generally obtained as thin films or monoliths. In addition, this pathway is still relatively complicated and requires multistep procedures (pre-polymerization, solvent evaporation, thermal solidification and finally carbonization). These disadvantages make it hardly feasible in a large scale due to the engineering difficulties such as sample collection, reactor design (large surface vessel), etc. [109–111] Therefore, other pathways based on the soft-templating concept needed to be explored to set facile and industrially feasible procedures. The aqueous precursor-surfactant-assembly approach widely used for the synthesis of ordered porous silica materials is an attractive route since pore sizes, pore symmetries and morphologies can be easily tailored. Besides, the aqueous route shows better reproducibility and unlimited fabrication batch size which are required in the industrial scale productions. Moreover, contrary to EISA route no extra thermal solidification is needed. [109,111]

A dilute aqueous induced self-assembly route using resol and triblock copolymers (Pluronic F127 and P123) has been proposed to prepare ordered mesoporous carbon materials with various structures under atmospheric pressure and relatively low temperatures ($\sim 60-70°C$) [110,111]. The mesoporous carbon powders C-FDU-14 and C-FDU-16 with cubic pore symmetries and C-FDU-15 with 2D hexagonal pore structure could be obtained. The cooperative self-assembly was driven by hydrogen-bonding. As well as in the EISA strategy, the key to the success of this synthesis is to well-separate into two the processes the cooperative self-assembly. It takes about 24 h to get the precipitation of organic precursor-template composites and about 5 to 7 days to complete the reaction due to the slow reaction rates: this leads to high quality products. The template removal and the subsequent carbonization were

achieved under inert atmosphere after sedimentation, collection and drying in air of the final products. Moreover, another unique feature of the aqueous route is that the morphology can be controlled on the scale of millimeters or micrometers. Besides, even single crystals can be derived from this synthesis approach [112,113].

Recently, a dilute aqueous induced self-assembly route using resorcinol and hexamine (also known as hexamethylenetetramine HMT) as carbon source and Pluronic F127 as surfactant was also used to synthesize ordered mesoporous carbons with cubic and 2D hexagonal structures under mild conditions (80°C) [109]. Contrary to the previous, this synthesis is a one-pot route with no additional pre-polymerization step of the carbon source. Indeed the HMT carbon precursor as a crucial role: it acts as a slow release source of formaldehyde and then control the kinetics of the polymerization reaction. The organic precursor-template composites precipitation occurred within half an hour and the reaction could be completed in one day. The mesoporous carbons were obtained after template removal and subsequent carbonization under inert atmosphere, sedimentation, collection and drying in air.

I.3.2. Synthesis procedure of C-FDU-16–type carbon

During this work, the mesoporous carbon was synthesized following an aqueous induced self-assembly route based on the soft-templating concept. The synthesis was performed under mild temperatures and in basic conditions according to procedures reported previously by Zhang et al. [110,111]

The carbon source was phenol/formaldehyde 38 wt% (PF) and the structure directing agent was Pluronic F127 ($PEO_{106}PPO_{70}PEO_{106}$). The solvent was distilled water (H_2O) prepared-in-house. A solution of sodium hydroxide (NaOH) of 0.1 M was used to create a basic medium.

It is well-known that the polymerization of phenol with formaldehyde can be catalyzed by an acid or a base. [114] The choice of catalyst affects the resulting frameworks. Base-catalyzed processes can result in phenolic resins with a 3-D network structure with benzene rings as three or four cross-linking sites. In contrast, acid catalysts induce linear polymerization according to previous reports. [114]

The mass ratio between the starting materials was set to 1 : 2.5 : 2.4 : 25 : 25 [Phenol : Formaldehyde : Pluronic F127 : H_2O : NaOH]. In a typical procedure, phenol was dissolved in formaldehyde and the resulting mixture was diluted in the NaOH solution under soft stirring at 72°C for 0.5 h; a clear solution was obtained. Meanwhile, temperature-aided dissolution of Pluronic F127 was performed in the distilled water. Once both mixtures were prepared, they were mixed together under vigorous stirring at room temperature for 3 h; a transparent solution

was obtained. The solution was then continuously stirred at 64°C for 120 h. After about 48 h, the solution turned dark red then brown reddish some 48 h later when the precipitation occurred. It was afterward stirred at 72°C for additional 48 h. The brown powder products, namely FDU-16, were collected by sedimentation, filtration and air-drying at room temperature. Finally, the as-made composite was thermally treated in a tubular furnace under N_2 flow in order to remove the structure directing agent and to perform the carbonization of the as-made polymer material. A black powder was obtained after the complete pyrolysis.

I.3.3. Structure directing agent removal for as-synthesized FDU-16 polymer composite material

In order to identify an appropriated thermal treatment for the template removal as well as for the carbonization of the FDU-16 polymer composite, the pyrolysis program was established according to the thermogravimetric analysis (TGA) of the as-synthesized sample.

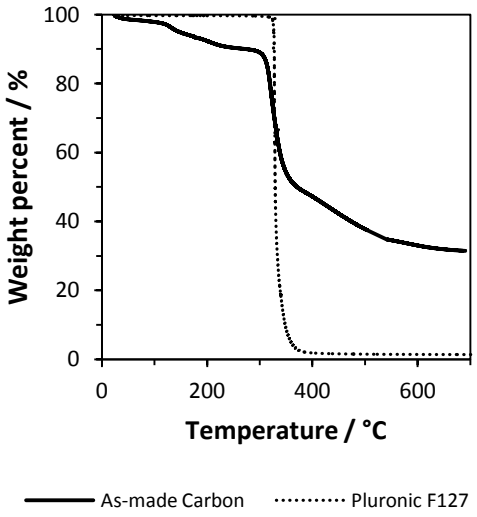

Figure 1.10: TGA profile of as-synthesized 'carbon' polymer composite and Pluronic F127 template in inert atmosphere.

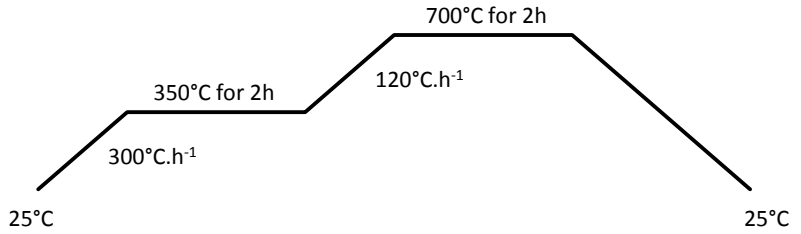

Figure 1.11: Calcination route for removal of the template of 'carbon' polymer composite.

Different weight loss ranges corresponding to different phenomena occurring during the thermal treatment can be observed in the TGA profile of the 'carbon' polymer composite, as shown on **Figure 1.10**: (i) the first one, from room temperature to 100°C, is correlated to desorption of physisorbed species (water), (ii) the second one, from 100°C to 250°C, is associated to removal of chemisorbed species (water), (iii) the third one, from 250°C to 350°C, corresponds to the decomposition of template molecules, (iv) the fourth one, from 350°C to 600°C, is assigned to the decomposition of the carbon precursor polymer network and (v) finally above 600°C, there is negligible weight loss showing total conversion into carbon (carbonization) of the polymer matrix. Therefore, in order to eliminate the Pluronic F127 template, the following thermal procedure was applied, **Figure 1.11**: the sample was heated to 350°C and held at this temperature for 2 h, then it was heated to 700°C and maintained at this temperature during 2 h, finally it was cooled down to room temperature. The heating rate was set to 300°C. h^{-1} and 120°C. h^{-1} before and after 350°C respectively.

I.3.4. Characterization of porous C-FDU-16 carbon matrix

The textural properties of the carbon matrix C-FDU-16 were investigated using nitrogen adsorption/desorption measurements at 77 K (**Figure 1.12**). The isotherm is characterized by an initial sharp uptake at relative pressures below 0.05 followed by a more gradual adsorption and a final plateau ends the adsorption branch. According to the IUPAC, such isotherm is characterized as mixed type *I* and *IV*, which are attributed to samples containing both microporosity and mesoporosity. [80] The absence of a sharp upswing before the ending plateau implies the presence of only primary mesopores. A hysteresis loop of type *H4*, commonly found in microporous carbon adsorbents is also present due to cavitation effect [82] and suggests that the pores are ink-bottle shaped (with narrow neck and wide body).

The equivalent surface areas were calculated using BET method (the term 'equivalent' is used since the BET surface area is estimated including the presence of microporosity). The microporous and total pore volumes were determined by *t*-plot analysis. The pore size was derived from the adsorption branch using BJH method. The textural properties of the carbon matrix are summarized in **Table 1.3**.

Transmission electron microscopy permits the identification of the pore system organization and the pore size of the porous carbon matrix. TEM images show a homogenous and ordered pore structure with little variation in size ($D_{pore} \sim 3$ nm), **Figure 1.13**. A 3D body centered cubic pore arrangement corresponding to the $Im\bar{3}m$ space group, characteristic of C-FDU-16 carbon material previously reported [111], is evidenced.

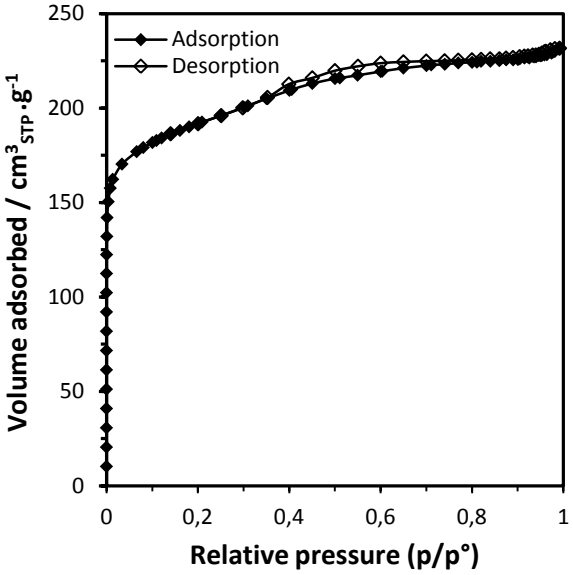

Figure 1.12: Nitrogen ad-/desorption isotherm at 77 K of carbon matrix.

Table 1.3: Textural properties of carbon matrix.

Sample	S_{BET} [a] $/m^2.g^{-1}$	$V_{\mu porous}$ [b] $/cm^3.g^{-1}$	$V_{total\ pore}$ [c] $/cm^3.g^{-1}$	D_{pore} [d] /nm
Carbon	700	0.2	0.35	< 2 + 2.5-3
a BET surface area		**c** Total pore volume		
b Microporous volume		**d** Pore size at the maxima of pore size distribution (for D_{pore} > 2 nm)		

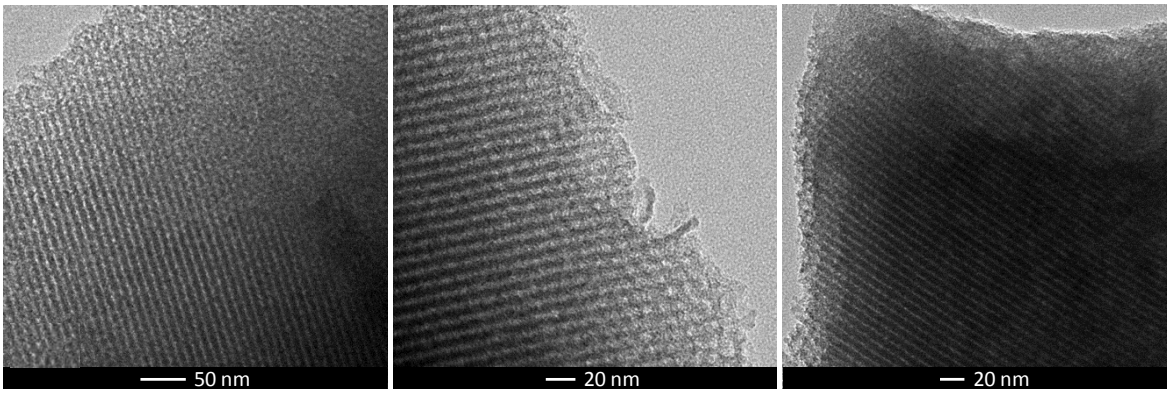

Figure 1.13: TEM images of porous carbon.

References

[1] F. Schüth, *Chem. Mater*., 13 (2001) 3184.

[2] (a) Y.S. Xia, J. Liu, L. Zeng, et al., *Synth. React. Inorg. Me.,* 44 (2014) 1312. (b) R. Ryoo, S.H. Joo, S. Jun, *J. Phys. Chem. B.*, 103 (1999) 7743. (c) S. Jun, S.H. Joo, R. Ryoo, et al., *J. Am. Chem. Soc.*, 122 (2000) 10712.

[3] (a) F. Liebau, *Micropor. Mesopor. Mater.,* 58 (2003) 15. (b) F. Schüth, W. Schmidt, *Adv. Mater.,* 14 (2002) 629.

[4] G.J.D. Soler-Illia, C. Sanchez, B. Lebeau, et al., *Chem. Rev.*, 102 (2002) 4093.

[5] A. Monnier, F. Schuth, Q. Huo et al., *Science,* 261 (1993) 1299.

[6] G.J.T. Tiddy, 'Surfactant Liquid Crystals' in *Handbook of Applied Surface and Colloid Chemistry*, John Wiley and Sons: New York, Vol. 1 (2002) pp. 465–468.

[7] P. Ekwall, in *Advances in Liquid Crystals*, Academic Press: New York, Vol. 1 (1975) pp. 1–142.

[8] N. Kitazawa, H. Namba, M. Aono, et al., *J. Non-Cryst. Solids* 332 (2003) 199.

[9] V. Boonamnuayvitayaa*,* C. Tayamanona, S. Sae-ungb, et al., *Chem. Eng. Sci.*, 61 (2006) 1686.

[10] Y. Wang, D. Zhao, *Chem. Rev.*, 107 (2007) 2821.

[11] D.Y. Zhao, Q.S. Huo, J.L. Fenget al., *J. Am. Chem. Soc.*, 120 (1998) 6024.

[12] T Asefa, M.J MacLachlan, N Coombs, et al., *Nature*, 402 (1999) 867.

[13] B.J Melde, B.T Holland, C.F Blanford, et al., *Chem. Mater.*, 11 (1999) 3302.

[14] M. Kruk, M. Jaroniec, C.H. Ko, et al., *Chem. Mater.,* 12 (2000) 1961.

[15] J.J. Watkins, T.J. McCarthy, *Chem. Mater.*, 7 (1995) 1991.

[16] W.-H. Zhang, X.-B. Lu, J.-H. Xiu, et al., *Adv. Funct. Mater*., 14 (2004) 544.

[17] L. Huang, C. Poh, S.C.Ng, et al., *Langmuir*, 21 (2005) 1171.

[18] Y. Liang, M. Hanzlik, R. Anwander, *Chem. Commun*., (2005) 525.

[19] N. Leventis, S. Mulik, X. Wang, et al., *J. Non-Cryst. Solids*, 354 (2008) 632.

[20] K.W. Gallis, C.C. Landry, *Adv. Mater*., 13 (2001) 23.

[21] B. Tian, X. Liu, C. Yu, et al., *Chem. Commun*.,(2002), 1186.

[22] B. Tian, X. Liu, L.A. Solovyov, et al., *J. Am. Chem. Soc*., 126 (2004) 865.

[23] A. Hozumi, Y. Yokogawa, T. Kameyama, et al., *Adv. Mater.,* 12 (2000) 985.

[24] W.C. Preston, *J. Phys. Colloid Chem.,* 52 (1948) 84.

[25] J.N. Israelachvili, 'Physical principles of surfactant self-association into micelles, bilayers, vesicles and microemulsion droplets' in *Surfactants in Solution*. Plenum Press: New York, Vol. 4 (1986) pp. 3–33.

[26] B. Lindman, H. Wennerström, *Top. Curr. Chem.*, 87 (1980) 1.

[27] G. Gunnarsson, B. Joensson, H. Wennerstrom, *J. Phys. Chem.,* 84 (1980) 3114.

[28] C. Tanford, *The Hydrophobic Effect: Formation of Micelles and Biological Membranes*, Second Ed., John Wiley and Sons: New York, (1980).

[29] J.N. Israelachvili, *Intermolecular and Surface Forces,* Third Ed., Academic Press: Burlington, (2011).

[30] S.M. Gruner, *J. Phys. Chem.*, 93 (1989) 7562.

[31] K. Borisch, S. Diele, P. Göring, et al., *J. Mater. Chem.*, 8 (1998) 529.

[32] J.M. Seddon and R.H. Templer, 'Polymorphism of lipid-water systems' in *Handbook of Biological Physics*, Elsevier Science B.V.: London, Vol. 1 (1995) pp. 97–160.

[33] S. Alperine, Y. Hendrikx, J. Charvolin, *J. Phys. Lett.*, 46 (1985) L27.

[34] Y. Hendrikx, J. Charvolin, *Liq. Cryst.*, 3 (1988) 265.

[35] G.C. Shearman, N.J. Brooks, G.J.T. Tiddy, et al., *Soft Matter*, 7 (2011) 4386.

[36] F. Husson, H. Mustacchi, V. Luzzati, *Acta Crystallogr.*, 13 (1960) 668.

[37] V. Luzzati, in *Biological membranes*, Academic Press: London, Vol. 1 (1968) pp. 71–123.

[38] V. Luzzati, A. Tardieu, T. Gulik-Krzywicki, *Nature,* 217 (1968) 1028.

[39] P. Kékicheff, B. Cabane, *J. Phys.-Paris*, 48 (1987) 1571.

[40] H. Hagslatt, O. Soderman, B. Jonsson, *Liq. Cryst.*, 17 (1994) 157.

[41] M.C. Holmes, *Curr. Opin. Colloid In.*, 3 (1998) 485.

[42] M.C. Holmes and M.S. Leaver, in *Bicontinuous Liquid Crystals*, CRC Press - Taylor & Francis Group: Boca Raton, Vol. 127 (2005) pp. 15–39.

[43] S.T. Hyde, G.E. Schröder, *Curr. Opin. Colloid In.*, 8 (2003) 5.

[44] J.N. Israelachvili, D.J. Mitchell, B.W. Ninham, *Biochim. Biophys. Acta*, 470 (1977) 185.

[45] S.T. Hyde, *Pure Appl. Chem.,* 64 (1992) 1617.

[46] Q. Huo, D.I. Margolese, G.D. Stucky, *Chem. Mater.,* 8 (1996) 1147.

[47] J.N. Israelachvili, D.J. Mitchell, B.W. Ninham, *J. Chem. Soc., Faraday Trans. 2*, 72 (1976) 1525.

[48] P. Li, Y. Song, Q.G. Guo, et al, *Mater. Lett.*, 65 (2011) 2130.

[49] S. Cabrera, *Chem. Commun.*, (1999) 333.

[50] U. Ciesla, M. Froba, G. Stucky, et al., *Chem. Mater.,* 11 (1999) 227.

[51] M. Templin, A. Franck, A. DuChesne, et al., *Science*, 278 (1997)1795.

[52] C.G. Goltner, B. Berton, E. Kramer, et al., *Adv. Mater.*, 11 (1999) 395.

[53] Y.H. Deng, T. Yu, Y. Wan, et al., *J. Am. Chem. Soc.*, 129 (2007)1690.

[54] A. Boeckler, 'Tuning the pore size in electro deposited ZnO films using surfactants as structure-directing additives', at E-MRS Fall Meeting, Symposium B, Warsaw (2007).

[55] E. Bloch; T. Phan, D. Bertin, et al., *Micropor. Mesopor. Mater.*, 112 (2008) 612.

[56] E. Bloch, P.L. Llewellyn, T. Phan, et al., *Chem. Mater.,* 21 (2009) 48.

[57] J.S. Beck, J.C. Vartuli, W.J. Roth, et al., *J. Am. Chem. Soc.*, 114 (1992) 10834.

[58] S.K. Jana, A. Mochizuki, S. Namba, *Catal. Surv. Asia*, 8 (2004) 1.

[59] G.J.D. Soler-Illia, E.L. Crepaldi, D. Grosso, et al., *Curr. Opin. Colloid In.*, 8 (2003) 109.

[60] H. Fang, M. Zhang, W.-H.S. Shi, et al., *J. Non-Cryst. solids*, 352 (2006) 2279.

[61] F. Kleitz, T.-W. Kim, R. Ryoo, *Langmuir*, 22 (2006) 440.

[62] D. Khushalani, A. Kuperman, G. A. Ozin, *Adv. Mater.*, 7 (1995) 842.

[63] Y. Gogotsi, A. Nikitin, H.H. Ye, et al, *Nat. Mater.*, 2 (2003) 591.

[64] I. Agirrezabal-Telleria, J. Requies, M.B. Gueemez, et al., *Appl. Catal. B-Environ*, 115 (2012) 169.

[65] L.L. Hench, K.J. West, *Chem. Rev.,* 90 (1990) 33.

[66] C.J. Brinker, G.W. Scherer, *Sol-gel science: The Physics and Chemistry of Sol-Gel Processing*, Academic Press: San Diego, (1990).

[67] Q. Huo, D.I. Margolese, U. Ciesla et al., *Nature*, 368 (1994)317.

[68] W.J.J. Stevens, M. Mertens, S. Mullens, et al., *Micropor. Mesopor. Mater.*, 93 (2006) 119.

[69] C.T. Kresge, M.E. Leonowicz, W.J. Roth, et al., *Nature*, 359 (1992) 710.

[70] J.C. Vartuli, K.D. Schmitt, C.T. Kresge, et al., *Chem. Mater.*, 6 (1994) 2317.

[71] J.S. Beck, J.C. Vartuli, G.J. Kennedy, et al., *Chem. Mater.*, 6 (1994) 1816.

[72] (a) S. Inagaki, Y. Fukushima, K. Kuroda, *J. Chem. Soc., Chem. Comm.*, (1993) 680. (b) S. Inagaki, Y. Fukushima, K. Kuroda, 10th International Zeolite Conference, Garmisch Partenkir (1994).

[73] P. Tanev, T.J. Pinnavaia, *Science*, 267 (1995) 865.

[74] S.A. Bagshaw, E Prouzet, T.J. Pinnavaia, *Science*, 269 (1995)1242.

[75] C. Boissière, A. Larbot, A. Van Der Lee, et al., *Chem. Mater*., 12 (2000) 2902.

[76] R. Ryoo, J.M. Kim, C.H. Ko, et al., *J. Phys. Chem*., 100 (1996) 17718.

[77] D.Y. Zhao, J.L. Feng, Q.S. Huo, et al., *Science*, 279 (1998) 548.

[78] P. Holmqvist, P. Alexandridis, B. Lindman, *J. Phys. Chem. B*, 102 (1998) 1149.

[79] (a) P. Holmqvist, P. Alexandridis, B. Lindman, *Macromolecules*, 30 (1997) 6788. (b) C. Knöfel, J.°Descarpentries, A. Benzaouia, et al., *Micropor. Mesopor. Mater.,* 99 (2007) 79.

[80] K.S.W. Sing, D.H. Everett, R.A.W. Haul, et al., *Pure Appl. Chem.*, 57 (1985) 603.

[81] (a) P.I. Ravikovitch, A.V. Neimark, *Langmuir*, 18 (2002) 1550. (b) P.I. Ravikovitch, A.V. Neimark, *Langmuir*, 18 (2002) 9830.

[82] F. Rouquerol, J. Rouquerol, K.S.W. Sing, *Adsorption by Powders and Porous Solids: Principles, Methodology and Applications*, First Ed. Academic Press: London, (1999).

[83] C.F. Cheng, Y.C. Lin, H.H. Cheng, et al., *Chem. Phys. Lett*., 382 (2003) 496.

[84] Y. Sakamoto, M. Kaneda, O. Terasaki, et al., *Nature*, 408 (2000) 449.

[85] R. Ryoo, S.H. Joo, S. Jun, *J. Phys. Chem. B.*, 103 (1999) 7743.

[86] J. Lee, S. Yoon, T. Hyeon, et al., *Chem. Commun.*, 21 (1999) 2177.

[87] M. Kaneda, T. Tsubakiyama, A. Carlsson, et al., *J. Phys. Chem. B*, 106 (2002) 1256.

[88] S. Jun, S.H. Joo, R. Ryoo, et al., *J. Am. Chem. Soc.*, 122 (2000) 10712.

[89] (a) M. Kruk, M. Jaroniec, R. Ryoo, et al., *J. Phys. Chem. B*, 104 (2000) 7960. (b) R. Ryoo, S. H. Joo, M. Kruk, et al., *Adv. Mater.* 13 (2001) 677. (c) A.H. Lu, F. Schuth, *C. R. Chim.*, 8 (2005) 609. (d) F. Cheng, Z. Tao, J. Liang, et al., *Chem. Mater.*, 20 (2008) 667. (e) J. Lee, S. Yoon, T. Hyeon, et al., *Chem. Commun*., (1999) 2177. (f) J. Lee, S. Han, T. Hyeon, *J. Mater. Chem.*, 14 (2004) 478. (g) A.H. Lu, A. Kiefer, W. Schmidt, et al., *Chem. Mater*., 16 (2004) 100.

[90] (a) R. Ryoo, S.H. Joo, M. Kruk, et al., *Adv. Mater.,* 13 (2001) 677. (b) S.H. Joo, S.J. Choi, I. Oh, et al., *Nature*, 412 (2001) 169. (c) S.N. Che, K. Lund, T. Tatsumi, et al., *Angew. Chem. Int. Ed.,* 42 (2003) 2182.

[91] L.A. Solovyov, T.W. Kim, F. Kleitz, et al., *Chem. Mater.*, 16 (2004) 2274.

[92] F. Kleitz, S.H. Choi, R. Ryoo, *Chem. Commun.*, (2003) 2136.

[93] J. Lee, J. Kim, T. Hyeon, *Adv. Mater.,* 18 (2006) 2073.

[94] Y. Meng, D. Gu, F. Zhang, et al., *Chem. Mater.,* 18 (2006) 4447.

[95] C. Liu, L. Li, H. Song, et al., *Chem. Commun*., (2007) 757.

[96] R. Liu, Y. Shi, Y. Wan, et al., *J. Am. Chem. Soc.*, 128 (2006) 11652.

[97] Z. Li, W. Yan, S. Dai, *Carbon,* 42 (2004) 767.

[98] C.D. Liang, K.L. Hong, G.A. Guiochon, et al., *Chem., Int. Ed.,* 43 (2004) 5785.

[99] S. Tanaka, N. Nishiyama, Y. Egashira, et al., *Chem. Commun.*, (2005) 2125.

[100] Y. Meng, D. Gu, F. Zhang, et al., *Angew. Chem. Int. Ed.,* 44 (2005) 7053.

[101] (a) O.T. Ikkala, J. Ruokolainen, G. ten Brinke, et al., *Macromolecules*, 28 (1995) 7088. (b) A. Sidorenko, I. Tokarev, S. Minko, et al., *J. Am. Chem. Soc.,* 125 (2003) 12211.

[102] P.P. Chu, H.D. Wu, *Polymer,* 41 (2000) 101.

[103] H. Kosonen, J. Ruokolainen, M. Torkkeli, et al., *Macromol. Chem. Phys.*, 203 (2002) 388.

[104] C.D. Liang, S. Dai, *J. Am. Chem. Soc.,* 128 (2006) 5316.

[105] Y. Huang, H. Cai, T. Yu, et al., *Angew. Chem. Int. Ed*., 46 (2007) 1089.

[106] Y.H. Deng, T. Yu, Y. Wan, et al., *J. Am. Chem. Soc*., 129 (2007) 1690.

[107] Y.H. Deng, C. Liu, D. Gu, et al., *J. Mater. Chem.,* 18 (2008) 91.

[108] H.Q. Li, R.-L. Liu, D.Y. Zhao, et al., *Carbon*, 45 (2007) 2628.

[109] D. Liu, J.-H. Lei, L.-P. Guo, et al., *Carbon*, 50 (2012) 476.

[110] F.Q. Zhang, Y. Meng, D. Gu, et al*., J Am Chem Soc,* 127 (2005) 13508.

[111] F.Q. Zhang, Y. Meng, D. Gu, et al., *Chem Mater,* 18 (2006) 5279.

[112] F.Q. Zhang, D.Gu, T. Yu, et al., *J Am Chem Soc,* 129 (2007) 7746.

[113] D Gu, H. Bongard, Y. Meng, et al., *Chem Mater,* 22 (2010) 4828.

[114] A. Knop, L.A. Pilato, *Phenolic Resins: Chemistry, applications, and performance. Future directions*, Springer-Verlag: Berlin, (1985).

Chapter 2

Nanocomposites for the sensing of low-dose molecules using Raman spectroscopy

Table of contents

Chapter 2: Nanocomposites for the sensing of low-dose molecules using Raman spectroscopy

II.1. Context and scientific approach

The sensitive and selective detection and identification of small analyte molecules at very low concentrations is of great importance in the medical field, for instance for the diagnosis of diseases, the study of human and animal physiology, and in the environmental field for applications such as the monitoring of environmental integrity and product quality. A large number of highly innovative approaches have emerged in order to overcome this challenge. Most of them use nanotechnologies and are based on biological, spectroscopic, or imaging techniques.

Among the different techniques exploited, surface-enhanced Raman spectroscopy (SERS) has been and is still extensively studied for the detection of low-concentration molecules. This technique holds great potential and appears as a powerful analytical tool. [1–5] Indeed, in one hand, the Raman scattering, which is specific to different vibrational modes, can provide a unique 'fingerprint' of any Raman-active analyte molecule and information about its chemical structure and local environment. On the other hand, enhancement in Raman signal is observed when Raman-active molecules are in the vicinity (near or on) of 'nanostructured' or roughened metal surfaces. [1–5] Moreover, the fluorescence interference (arising from the analyte excitation) is quenched in such system configuration (analyte molecule–metal nanoparticle-based substrate) thanks to the presence of metal which provide non-radiative pathways for the decay of excited states. Besides since slight variations yield in measurable shifts in the location of SERS spectral peaks, minor changes in the orientation of the analyte can be detected. [5] Consequently the combination of all these characteristics offers a very sensitive chemical analysis through surface-enhanced Raman scattering (SERS) effect.

In the literature, two primary mechanisms of Raman signal enhancement are reported: namely the chemical enhancement (CE) mechanism and electromagnetic (EM) one. [6–9] The EM mechanism implies a strong local enhancement of the electric field (so-called 'hot spot') due to plasmon excitation of the metallic structure upon appropriate incident light. This subsequently enhance the scattering signal intensity of the analyte molecules that are located near or adsorbed on the hot spots present on the substrate metal nanoparticle surface. It provides the same enhancement for any type of molecule; it is therefore a chemically non-selective amplifier towards analyte for Raman scattering. [2,7,10] Besides, the EM enhancement depends strongly on the particle composition, size and shape, as well as on the distance between particles and

between the analyte and the particles. [2,5,11] Concerning the CE mechanism, it is reported to involve either molecule–metal surface interactions (resonant charge-transfer mechanism (CT) and non-resonant chemical mechanism (CHEM)) in which case the analyte molecule is chemically adsorbed on the metal or a molecular mechanism arising from the incident light being resonant with a molecule–molecule interaction. [12–16] It has been shown that it is very difficult to study the chemical enhancement mechanism selectively. Indeed, both types of enhancement mechanism may be present simultaneously in SERS. Moreover, these effects are multiplicative which make their effective separation difficult or even impossible. Though, contributions of both could be roughly estimated: whilst the chemical enhancement is only one or two orders of magnitude, the electromagnetic enhancement is dominant, and the scattered intensity can be increased by a factor in the range of 10^4 to 10^7. Furthermore, in order to meet the requirements of applications in the field of analysis, the chemical sensor should exhibit a good reproducibility in terms of detection. The reproducibility is directly correlated to material preparation. Therefore, it is essential that the metal nanoparticle-based substrates display a good dispersion of the nanoparticles, as narrow as possible size distribution of the latter, and homogeneity in shape to ensure its efficiency. One of the major challenges in SERS technique is the development of reliable SERS substrates with inexpensive, easy and reproducible processing that allow fulfilling all these qualifications.

Plenty of experimental studies were using noble metals in many different ways in order to develop SERS substrates. Especially, silver and gold were used as colloids in solution due to their ease of preparation and the high resulting enhancement of intensity [17–20]. Nevertheless, the poor control over particle aggregation limits their stability and the reproducibility of SERS signals. In order to overcome these issues, noble metals were deposited on different supports using principally either chemical or physical deposition on different substrates. [21–23] As compared to colloidal nanoparticles, this 2D design shows significantly better stability, controllability and reproducibility. However, it lacks advanced characteristics such as the porous structure and the periodicity that have been described to increase substrate performances [24,25]. Therefore, other design strategies have been developed to prepare 3D porous substrates that combine the advantages of a high specific area (preconcentration property) and 3D long-range ordering of pores in the substrate structure that could provide more binding sites for the probe molecule. [25–27]

Nanocomposites consisting of silica matrices containing noble nanoparticles (NPs) may be interesting candidates as SERS substrates since: first the porous host matrix and the incorporated particle size are well controlled and second this sample configuration allows preconcentration of the molecule in the solids. In this context, two types of substrates were

synthesized: pristine silica matrices and nanocomposites based of either silver or gold. The study was divided in two parts: first the determination and comparison of the adsorption thermodynamics (adsorbed amounts and associated enthalpies) of a model molecule, rhodamine 6G (R6G), and second the Raman response of the different systems 'model molecule–substrate' for different adsorbed amounts of the model molecule. The overall scientific approach is summarized in the scheme presented in **Figure 2.1**.

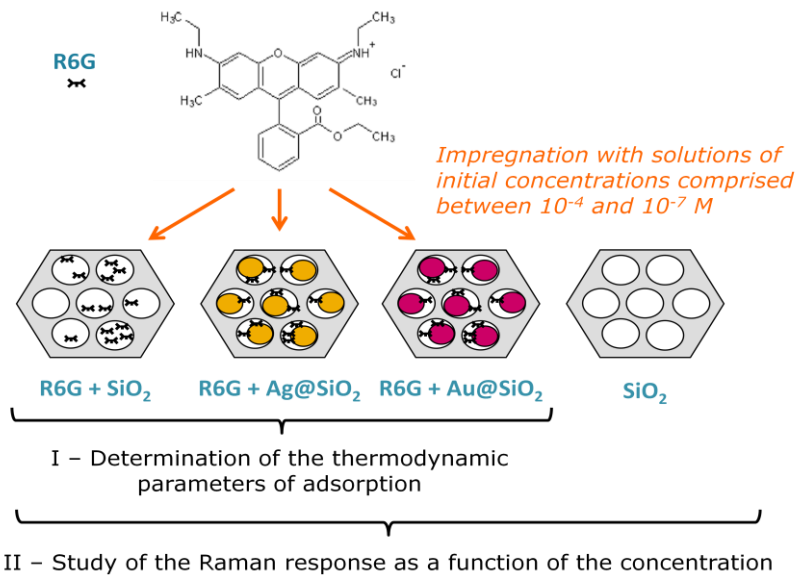

Figure 2.1: Schematic representation of the scientific approach.

II.2. Incorporation of noble metal nanoparticles in mesoporous silica matrices

In literature, different synthesis strategies have been used to incorporate noble metal, such as silver and gold, in porous matrices: i.e. either in one step or in two steps, **Figure 2.2**. In the first strategy, two approaches can be distinguished: in the first one, the so-called one-pot synthesis, the metal precursor is directly introduced to the reaction mixture [28,29], while in the second one, metal colloids are used instead [30,31]. In the second strategy, the two steps generally involve an impregnation process of the host matrix (previously synthesized) with the metal salt followed by a reduction in situ of the latter in the presence of appropriate reducing agent leads to formation (i.e. nucleation and growth) of the nanoparticles [32,33]. The most current reduction processes of gold and silver ions are: (i) the chemical reduction in liquid phase often carried out using sodium tetraborohydrate (sodium borohydride – $NaBH_4$) [34,35], (ii) the chemical reduction in gas phase generally performed under hydrogen [36,37] or an inert gas/hydrogen mixture flow [38,39] and (iii) thermal reduction in air at mild or high temperature values for several hours [32,40,41]. Although other techniques such as sonochemistry [42,43], radiolysis (γ irradiation source, electron accelerator) [44] and even UV irradiation are also

reported [45,46]. The latter methods require specific instrumentation, but with optimized experimental conditions the particles synthesized are located in the porosity and a homogeneous size distribution (with particle size lower than pore size) can be achieved.

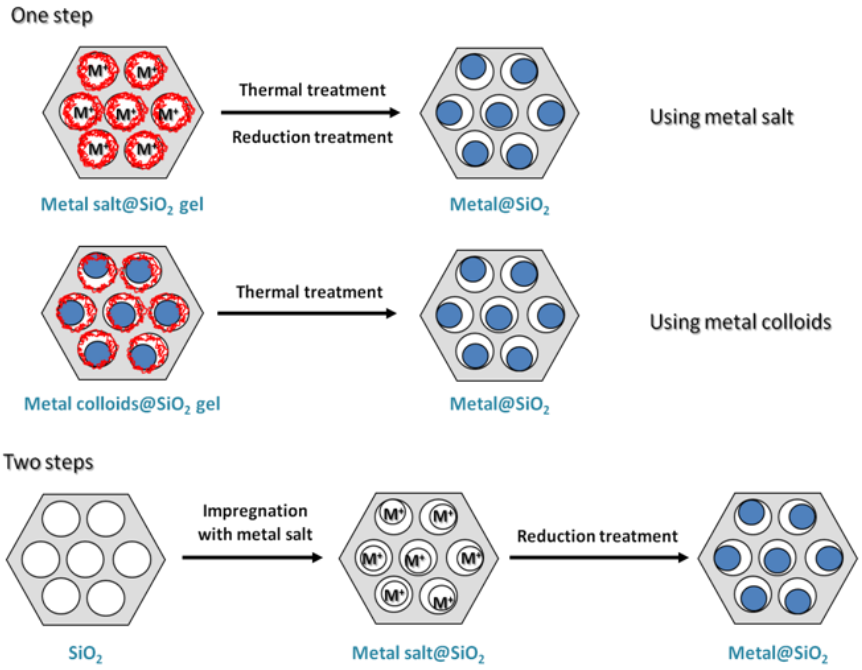

Figure 2.2: Scheme of the different strategies for the synthesis of nanocomposites.

During this work, mesoporous silica matrices, were beforehand prepared according to the syntheses presented in *Chapter 1*. The growth of noble nanoparticles in the porosity of the silica matrices was performed using the strategy in two steps: the impregnation of the silica matrices with solutions of the metal salts followed by a chemical reduction in gas phase. The general synthesis procedure of the nanocomposites studied is developed in the following paragraphs.

II.2.1. Impregnation step

The impregnation was effectuated under ambient conditions. The metal precursors used were silver nitrate ($AgNO_3$) and gold chloride hydrate ($HAuCl_4 \cdot xH_2O$), respectively. In a typical preparation, the powdered mesoporous silica support was dispersed into the metal salt solution in proportion of 100 mg of solid for 1.5 mL of solution. The concentration of both salt solutions (silver and gold) was fixed to 10^{-2} M. In addition, the preparation of gold particles via the two-step method generally requires the adjustment of the pH before and/or after the addition of the support [47,48]. Hence, the pH was set to 10 by dropwise addition of 30 wt% NaOH before and after the addition of silica to the gold chloride solution. For achieving equilibrium in the system, the suspension was thermostated at 25°C and agitated during 12 to 24 h. The impregnation process was performed in a dark room to avoid light-induced effects and with a rotary shaker to

enable suspension of the solid. After impregnation, the Metal salt@Silica sample was gathered by centrifugation and rinsed several times with distilled water in order to remove from the surface residual nitrate or chloride respectively. Lastly, the sample was collected the same way after washing and was dried at 80°C for 0.5 h.

II.2.2. Chemical reduction in gas phase

The growth of the noble metal in the porous silica matrices was achieved in gas phase since this method is easy, fast and well reproducible. The reduction of the metal ions adsorbed on silicas into metal nanoparticles was performed in a built-in-house apparatus. Prior to reduction process, the samples were degassed at room temperature then a purge with argon/hydrogen (95/5 molar ratio) mixture was performed to ensure purity of the atmosphere in the reduction system. Finally, the Metal salt@Silica samples were treated under the same Ar/H_2 atmosphere used for the purge, at 100°C or 150°C, during 1 h with a heating rate of $5°C.\,min^{-1}$. Afterwards, the nanocomposites Metal NPs@Silica were obtained. The *Silver NPs@Silica* nanocomposite, denoted as Ag@Silica, was obtained as a yellow powder while the *Gold NPs@Silica* one, denoted as Au@Silica, was obtained as a pink powder, as shown on the photographic images in **Figure 2.3**. These colors are known to be characteristics of isolated nanosized silver [39,44] and gold materials [31,44].

Figure 2.3: Photographic images of the samples Silica (a), Ag@Silica (b) and Au@Silica (c).

II.3. Study of the nanocomposites detection properties

II.3.1. Fundamentals of thermodynamics of adsorption in liquid phase and of Raman spectroscopy

As mentioned earlier, the nanocomposites detection properties were studied from a thermodynamic point of view and using a spectroscopic analysis based on the Raman effect. The thermodynamic part is the first step of the scientific approach. It is based on the study of the adsorption in liquid phase of a model molecule in the substrates and consists in one hand of the construction of adsorption isotherms and on the other hand of the determination of the

associated enthalpies. The spectroscopic analysis is the second step of the scientific approach. It consists in studying the Raman response of the substrates for different adsorbed amounts determined during the previous step of the study as well as the response of pure silica. The purpose of this section is to present fundamentals and methodology of the main analyses of the scientific approach. It is clear that it is impossible to present a complete review in available space, so the most relevant basic principles only will be presented.

II.3.1.a. Thermodynamics of adsorption in liquid phase [49]

It is not in our purpose to discuss completely the phenomenon of adsorption in this section. This will be described in more detail in the *Appendix B6*. Basically, the adsorption of a solute by solids from solution occurs at the liquid/solid interface, and it induces a change in the concentration. Adsorption mechanisms in liquid phase are competitive with respect to at least one solute and a solvent. Three principal factors governing the adsorption process can be highlighted: the interfacial tension between the solution and substrate, solute-substrate forces, the available solid surface. Several parameters affecting the adsorption process in liquid phase should be taken into account: namely the time, the temperature, the initial solute concentration, the pH, as well as the solvent. [50]

Adsorption isotherms

The most widely used approach to obtain direct determination of adsorption is to study the depletion of the species of interest from solution in equilibrium with the solid. Essentially, a certain amount of solute solution of initial concentration is added to a known weight of solid. Then, placed in a thermostat, the mixture is tumbled with a rotary shaker, for maintaining the solid in suspension, until adsorption equilibrium is reached (usually several hours). It should be mentioned that the method is applicable only with solid substrates possessing sufficient interface per unit volume, i.e. not too small specific surface area, to cause measurable change in concentration. [50] Finally, after separating the solid and the solution, the depletion of solute concentration in the supernatant is estimated using a spectroscopic method in UV or visible region. The Beer-Lambert law, expressed in **Equation 2.1**, enables the determination of the concentration which is directly related to the intensity of the measured absorption.

Equation 2.1 $$\boldsymbol{A = \varepsilon \times l \times C}$$

Where:	A	is the absorbance	
	ε	is the molar absorptivity	$[L.mol^{-1}.cm^{-1}]$
	l	is the path length (cuvette width)	$[cm]$
	C	is the analyte concentration	$[mol.L^{-1}]$

The molar absorptivity ε depends on the incident beam wavelength, the solvent and the temperature.

Knowing the equilibrium concentration (solute concentration in the supernatant once the time required reaching equilibrium is elapsed), the volume of the solute solution and the mass of the solid substrate, the amount of solute adsorbed at the solid-liquid interface can be determined by the following relationship, **Equation 2.2**, based on the depletion method:

Equation 2.2

$$N_{ads} = \frac{(C_i - C_{eq}) \times V}{m^s}$$

Where:			
	N_{ads}	is the amount adsorbed	$[mol.g^{-1}]$
	C_i	is the initial concentration	$[mol.L^{-1}]$
	C_{eq}	is the equilibrium concentration	$[mol.L^{-1}]$
	V	is the solution volume	$[L]$
	m^s	is the mass of adsorbent	$[g]$

Investigation of the substrate is conducted by considering a sequence of equilibrium states at constant temperature. These equilibrium states are achieved after several adsorption tests through impregnation of the solid substrates with solution of the solute of different initial concentrations. In order to get the most accurate results, a liquid/solid mass ratio must be defined for an optimum concentration deviation and should be kept constant for each acquiring measurements. The experimental excess surface adsorbed amounts can be considered as the equivalent adsorbed amounts, though there is no available information of the solvent near the interface. The thermodynamic representation of the adsorbed amount of the species of interest versus the concentration at equilibrium is known as *adsorption isotherm*.

Giles, Smith and Huitson classified adsorption isotherms in liquid phase into four categories that are themselves divided into subclasses [51] as presented in **Figure 2.4**. This classification presents four types of adsorption and seventeen classes in total. This number is quite high and it is not necessarily exhaustive. Indeed, the shape of the adsorption isotherm reflects a combination of several types of interactions, between the solutes, the solute and the solvent, the solute and the surface and the solvent and the surface, during the adsorption process in liquid phase. The adsorption takes place, not only by the attractive interaction between the solute and the solid, but also by stabilization of the system by exclusion of the solute relative to the solvent and therefore by the accumulation of the solute in the solid phase. The surface itself has a major influence on the isotherm shape. It can be crystalline or amorphous, it can have different adsorption sites and a certain pore size distribution. Thus, the description of the isotherms can be made reasonably considering only two of these types: type *L* and type *S*.

The isotherms of type *S* exhibit a first convex portion followed by an inflection point and then a plateau. This type of isotherm is common and reflects strong adsorbate–adsorbate interactions. The change in concavity suggests interactions between the adsorbed molecules.

The *L*–type isotherms, also called Langmuir–type, consist of a first concave portion. Such isotherm reflects uniform and narrow distribution of adsorption sites without the presence of adsorbate–adsorbate interactions. Experimental isotherms frequently correspond to a combination of these two ideal isotherms since the surfaces studied are rarely energetically homogeneous.

The isotherms of type *H* ('H' standing for high affinity) may be an extreme case of *L*–type isotherm or an *L*–type isotherm having an accuracy at low concentrations which is not sufficient. Similarly, the isotherms of type *C* are the linear part of the isotherm of type *L* in a concentration range corresponding to that of Henry. They reflect a mechanism of adsorption with or without saturation of the solid.

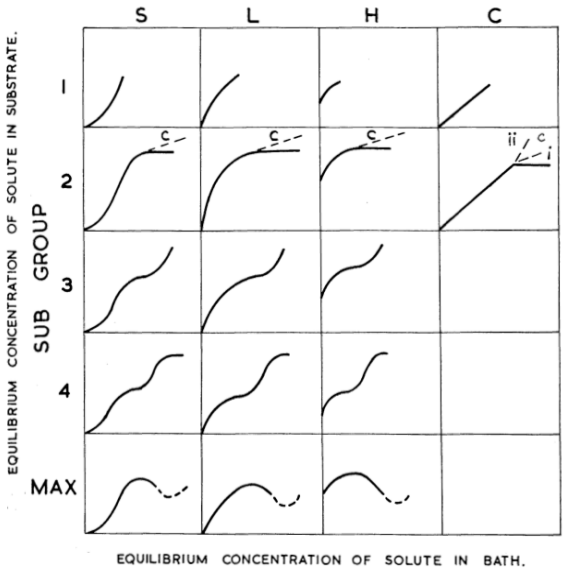

Figure 2.4: Giles, Smith and Huitson classification of adsorption isotherms in liquid phase. [51]

The literature states that there is a type of 'exotic' isotherm: the type *Z*. This isotherm has the peculiarity of having a breakout. At some point, the adsorbed amount increases but the equilibrium concentration decreases. This behavior is explained by a change in the solid surface. This type of adsorption isotherm is met, for example, in the case of adsorption of p-nitro-phenol in 2,2,4-trimethylpentane on dry cellulose [52]. The p-nitro-phenol is adsorbed depicting a *S*–type isotherm, until the structure of cellulose starts to deteriorate and its surface increases. This leads to a higher adsorption and thus a lower equilibrium concentration. This type of isotherm is due to a structural change of the solid. It represents a particular case of the adsorption process.

The adsorption isotherm accuracy may depend on various parameters such as the solubility of the adsorbent, the chemistry of the surface, the purity of solids and liquids, etc. The description of these isotherms allows developing various mathematical modeling. These models provide essentially a mathematical description of the isotherm and are mainly used in the field of environment [53]. The Langmuir model, which expresses the adsorbed amount versus equilibrium concentration, **Equation 2.3**, is the most widely used.

Equation 2.3

$$N_{ads} = N_{max} \times \frac{b \times C_{eq}}{1 + b \times C_{eq}}$$

Where:			
	N_{ads}	is the adsorbed amount	$[mol.g^{-1}]$
	N_{max}	is the adsorbed amount at saturation	$[mol.g^{-1}]$
	C_{eq}	is the equilibrium concentration	$[mol.L^{-1}]$
	b	is a constant reflecting the affinity	

The adsorption isotherm is essential to determine the adsorption properties of a solid. However, most of the solids being heterogeneous, the solid surface cannot be described as a set of identical sites neither from a chemical nor from a structural point of view. It is not trivial to model an adsorption isotherm since the adsorption in liquid phase is a phenomenon of displacement of a molecule by other molecules in the vicinity of a surface. The thermodynamic characterization of the system is then not only based on the study of the adsorption isotherm but also on the measurements of energetic variables such as the *enthalpy of the solute displacement*, also known as *enthalpy of adsorption*. This displacement concept is easily conceptualized by assimilating the exchange at the interface to a chemical reaction involving the displacement of r molecules of a solute A by a molecule of solute B:

Equation 2.4

$$\mathbf{r} \times \boldsymbol{A}_{(ads)} + \boldsymbol{B}_{(liq)} = \boldsymbol{A}_{(liq)} + \boldsymbol{r} \times \boldsymbol{B}_{(ads)}$$

Although widely used, the concept is fairly simple and can be exceeded in some cases (molecules of very different sizes, special conformations of the adsorbed molecules, etc.).

Adsorption enthalpies (or displacement enthalpies)

Enthalpies of adsorption are derived from the heat released during the displacement of the solute or solvent during the adsorption process. Measurements of these energies at constant temperature are performed using calorimeter instrument comprising two cells: a reference cell and a measuring cell. During the calorimetric analysis, it is essential to maintain symmetry between both cells in order to avoid measurement artifacts. The reference cell contains only the

solvent while the measuring cell contains the solvent and the solid in suspension. Then, solution of the solute is injected in the two cells simultaneously at equal rates.

Knowing the adsorption isotherm equation and the amount balance, the amount of solute adsorbed in the solid during each injection can be determined. The amount balance can be expressed as follows:

Equation 2.5 $$\boldsymbol{N_{ads} = N_i - N_{eq}}$$

Equation 2.6 $$\boldsymbol{N_{eq} = C_{eq} \times V_{eq}}$$

Equation 2.7 $$\boldsymbol{N_{ads} = N_i - C_{eq} \times V_{eq}}$$

Where:			
	N_{ads}	is the adsorbed amount	$[mol]$
	N_i	is the injected amount	$[mol]$
	N_{eq}	is the amount at equilibrium	$[mol]$
	C_{eq}	is the equilibrium concentration	$[mol.L^{-1}]$
	V_{eq}	is the equilibrium volume	$[L]$

The equilibrium concentration is related to the adsorbed amount through the adsorption isotherm, **Figure 2.5**. Indeed, the intersection of the two curves determines the amount adsorbed. It is calculated by using dichotomy inserted into a spreadsheet program. From the data obtained by adjusting the isotherm and knowing the weight of solid, the weight of solvent, the amount injected and the concentration of solution, it is possible to determine from the amount balance the amount adsorbed in the solid and the amount remaining in solution. Successive tests of equilibrium concentration are carried out in iterative way until coincide with the isotherm values calculated from the adjustment previously performed.

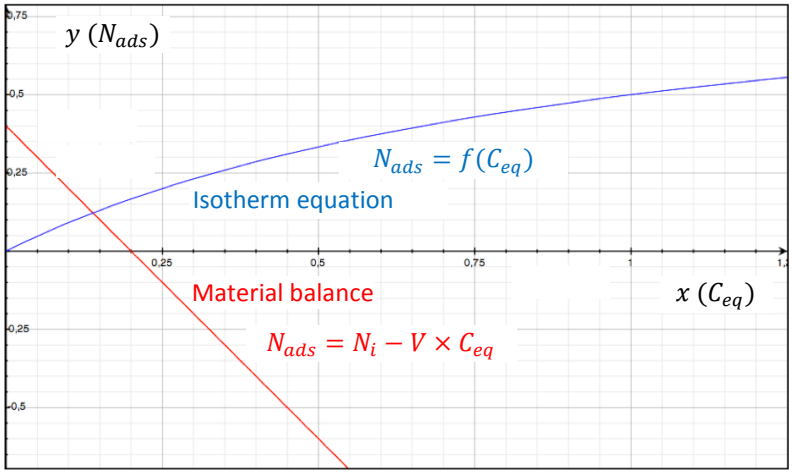

Figure 2.5: Method for the determination of the amount adsorbed in the solid.

The thermogram obtained from the calorimetric measurements represents an electromotive force as a function of time. By integration of the peaks through the calorimeter constant, the experimental amount of heat can be calculated, **Equation 2.8**.

Equation 2.8

$$Q_{exp} = \frac{1}{k} \times \int_{t_0}^{t_1} (V \times dt)$$

Where*:*

	Q_{exp}	is the experimental heat amount
	k	is the calorimeter constant
	t_0	is the final time bounding the peak
	t_1	is the starting time bounding the peak
	V	is the voltage

The peak shape also allows getting information on the reaction kinetics. The experimental amount of heat measured is the sum of the enthalpies of the solution dilution in the solvent and of the solvent displacement by the solute. The enthalpy of displacement is obtained by subtracting the enthalpy of the mixture to the experimental one.

II.3.1.b. Raman spectroscopy

In this section, a short review on the phenomena originating Raman scattering will be presented from a classical point of view. The advantages as well as the limitations of Raman spectroscopy will be mentioned. And finally, the so-called Surface enhanced Raman scattering (SERS) will be introduced.

Raman scattering and SERS effect

When a light illuminates a material, the major part of the light crosses it or is reflected, and the rest is absorbed, depending on the incident wavelength and on the nature of the material. A small proportion (about 0.1 %) of the light is scattered elastically and a much smaller fraction (approximately 0.0001 %) is inelastically scattered (with wavelength slightly different from the wavelength incident): this is referred as Rayleigh and Raman scattering, respectively. Raman scattering corresponds to an energy exchange between the material and the light. This exchange of energy can result either by a loss of energy (light scattered with higher frequency) or by a gain of energy (light scattered with lower frequency): this phenomena correspond to Raman anti-Stokes and Raman Stokes scatterings as shown on **Figure 2.6**. The order of magnitude of the exchanged energy corresponds to the energy separating two vibrational levels of the material.

The Raman spectrum represents the image of the vibrational energy levels (wavenumber and wavelength transition) of the molecule. Furthermore, the amount of photons generated for every

Raman line is linearly proportional to the concentration of the molecule. The energy of the incident photons is often inverted so that the energies corresponding to the Stokes process are positive. Indeed, the Stokes scattering is more intense than anti-Stokes scattering and it is thus much more used. The reason is directly related to the Boltzmann distribution between the lowest vibrational states.

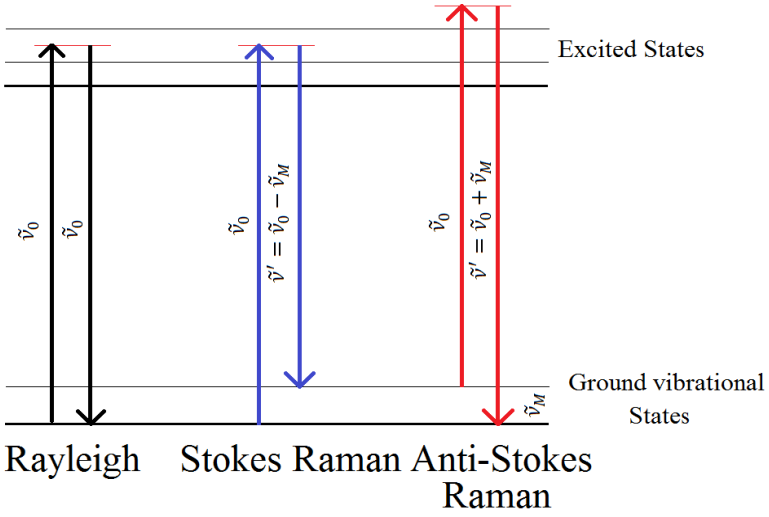

Figure 2.6: Energetic representation of elastic diffusion (Rayleigh) and inelastic diffusion (Stokes and anti-Stokes).

Raman spectroscopy presents various advantages. Indeed it is a non-destructive and non-invasive method that allows applying it to real systems. It is easy to handle and the setting-up time is null or almost null. It requires only a small amount of sample and whatever the physical state of the sample (solid, liquid or gas samples). Moreover, in a wide variety of samples can be analyzed, even with very small size ($< 1\ \mu m^3$). It is sensitive to small structures (identification of amorphous systems, the analysis of thin films for which diffraction methods can be sometimes difficult to achieve). It allows working in a hostile environment, in particular at high temperature, in the presence of radioactive phenomena or in a controlled atmosphere. Besides, this technique can be combined with other analytical methods and offers the possibility of in situ measurements.

However, two main limitations can be noticed is this analysis technique. First, the spatial resolution of the Raman spectroscopy is unsuitable for the study of the nanometric materials. This limit finds its origin in the undulatory nature of the light. In 1873, E. Abbe [54] then L. Rayleigh [55] in 1879, formulated the theory of resolution and established the criterion of diffraction, namely the criterion of Abbe or criterion of Rayleigh. This criterion allows estimating the minimal d_{min} necessary distance to distinguish two objects (**Equation 2.9**).

Equation 2.9

$$d_{min} = \frac{0.61 \times \lambda}{n \times \sin \alpha} = \frac{0.61 \times \lambda}{NA}$$

Where:

	λ	is the wavelength of the light
	N	is the refractive index of medium
	α	is the semi-angle of the incident light cone
	NA	is the numerical aperture

In practice, in the air, this means that the best resolution that can be obtained with a conventional Raman spectrometer coupled to a confocal microscope is in the range of 250 nm for a wavelength of 400 nm. The second limitation comes from the inefficiency of the diffusion process. As compared to the infrared absorption or fluorescence, the cross section of the Raman diffusion is about $10^8 - 10^{10}$ times lower [56]. Therefore, the study of very dilute solutions or isolated systems is not possible by conventional Raman spectroscopy. These two limits may be overcome by exploiting the optical properties of noble metals. In the following section will be presented a technique based on the enhancement of the Raman scattering by optical properties of noble metals: the surface enhanced Raman scattering (SERS). Since its first observation in 1974, many studies have been conducted to understand the processes responsible for the SERS effect. According to the scientific community, mechanisms at the origin of the enhancement of the signal are multiple and rely on the coincidence of two major effects: chemical and electromagnetic effects.

Raman signal amplification of order of magnitude between 10^4 to 10^7 is assumed to be initiated from electromagnetic mechanism enhancement while the chemical mechanism generates an enhancement of about 10^1 to 10^2. The quantitative relative contribution between these two mechanisms has lead to many debates in the SERS community [57]. The electromagnetic effect, whose contribution is closely related to the surface condition and the optical response of the metal substrate, influences not only the exciting field but also on the scattered field. Indeed, enhancement of the incident electric field on nanoparticles by the plasmon resonance of surface can be observed, and also the latter behave as local antenna for the field transmitted by the nearby entities. The SERS effect is maximal when the excitation laser is made with the frequency of the plasmon of surface of nanoparticles. The chemical effect that is not yet fully understood, all the mechanism is not clarified. However, it allows explaining the selectivity of the SERS effect of certain molecules. Indeed, scientists agree that it essentially depends on the affinities between the metal and the molecule leading to interactions of chemical nature.

II.3.2. Preliminary study: feasibility and highlighting of decisive experimental parameters

A preliminary study on pristine and nanocomposite substrates with controlled particle size and quantity was necessary in order to validate the different experimental parameters allowing the detection of low-dose molecules coupling thermodynamics of adsorption and Raman spectroscopy of the study.

The first step of this preliminary study was the preparation of reproducible substrates for the different analyses. The pristine material is SBA-16–type silica matrix synthesized following the synthesis procedure presented in *Chapter 1*. The SERS substrate, named Ag@SBA-16, was synthesized by means of chemical reduction in gas phase after impregnation with silver salt for 24 h, as detailed in the previous section.

The SERS substrate was first characterized using a combination of different techniques: nitrogen adsorption/desorption measurements at 77 K, transmission electron microscopy, optical absorption and inductively coupled plasma-mass spectrometry (ICP-MS) measurements.

The textural properties of the samples were investigated using nitrogen adsorption/desorption measurements (**Figure 2.7**). As for the parent silica host matrix, the isotherm of Ag@SBA-16 is characterized by an initial sharp uptake at relative pressures below 0.05 followed by a more gradual adsorption then a second sharp upswing between 0.5 and 0.7. A final plateau ends the adsorption branch. According to the IUPAC, such isotherm is characterized as mixed type *I* and *IV*, which are attributed to samples containing both microporosity and rigid mesoporosity. [58] A hysteresis loop of type *H2*, characteristic of adsorbent with ink-bottle shaped pores [59] (with narrow neck and wide body), is observed. Due to the smaller pore entries, the nitrogen molecules are not desorbed progressively, but are retained until a sudden desorption step originating from cavitation effect [60] occurs at relative pressures closed to 0.45 as for the pristine material. The equivalent surface areas were calculated using BET method (the term 'equivalent' is used since the BET surface area is estimated including the presence of microporosity). The microporous and total pore volumes were determined by *t*-plot analysis. The pore size was derived from the adsorption branch using BJH method. Shift to lower values of the isotherm suggests a decrease of the textural properties probably due to pore blocking effect caused by the presence of particles in the pores. Indeed, this tendency can be observed in the values of the textural properties which are summarized in **Table 2.1**, in particular in the specific surface area and the pore volumes.

Transmission electron microscopy permits the identification of the nanoparticle size and location in the silica host matrix. The mesopore size remains unchanged with the incorporation of silver nanoparticles. It is possible to estimate their size in **Figure 2.8 (a).** An analysis of many images indicates that the few nanoparticles observed are spherical and have a mean diameter of about 3 nm with an observed standard deviation that is less than 1 nm. They are distributed homogeneously within the silica matrix.

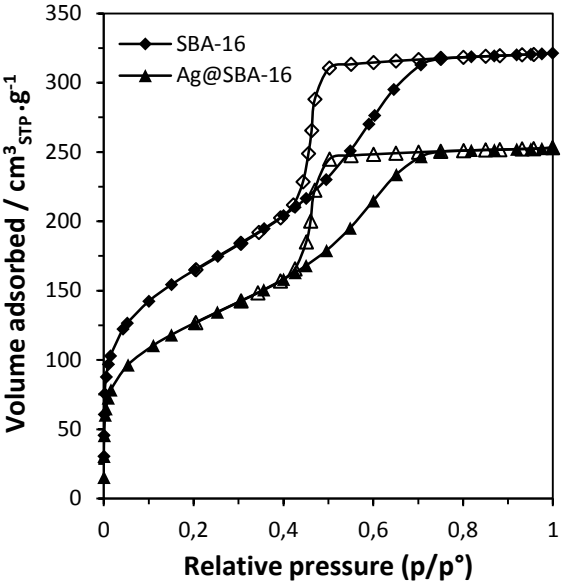

Figure 2.7: Nitrogen ad-/desorption isotherms at 77 K of SBA-16 and Ag@SBA-16 samples.

Table 2.1: Textural properties of SBA-16 and Ag@SBA-16 samples.

Sample	S_{BET} [a] $/m^2.g^{-1}$	$V_{\mu porous}$ [b] $/cm^3.g^{-1}$	$V_{total\ pore}$ [c] $/cm^3.g^{-1}$	D_{pore} [d] /nm
SBA-16	580	0.04	0.50	4.5
Ag@SBA-16	450	0.02	0.40	4.5
a BET surface area		**c** Total pore volume		
b Microporous volume		**d** Pore size at the maxima of pore size distribution		

The position of the plasmon resonance band of the nanocomposite sample, Ag@SBA-16, was determined using UV–vis spectroscopy. The plasmon band is centered on 400 nm, as shown in **Figure 2.8 (b).** This resonance is typical for isolated silver nanoparticles and is in agreement with the literature in which the plasmon resonance maximum of silver particles confined in porous silicas is found in the 400 − 440 nm region. [39,44,61]

According to inductive coupled plasma – mass spectrometry (ICP–MS) measurements, the silver loading in the silica host matrix was estimated to be close to 2.5 mg of silver per gram of silica, corresponding to a percentage of 0.25 wt%.

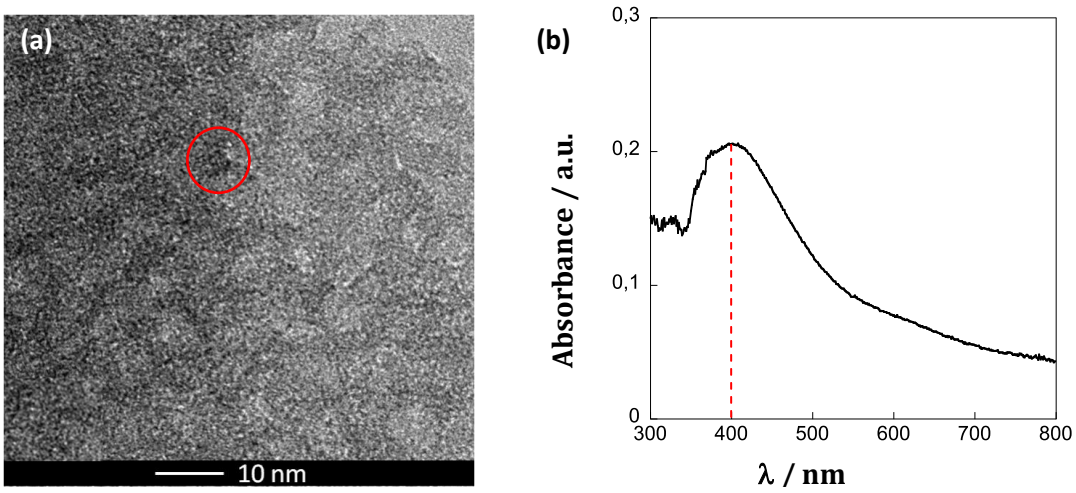

Figure 2.8: TEM image (a) and absorption spectrum (b) of the nanocomposite Ag@SBA-16.

This specific configuration, i.e. small and low concentration of silver nanoparticles homogeneously distributed within the silica matrix, was chosen in order to study precisely the influence of the presence of silver nanoparticles on the Raman response, avoiding interaction between particles and avoiding the creation of 'hot spots'. [7]

The adsorption of R6G in ethanol was primarily studied from a thermodynamic point of view on the two porous substrates, leading to two types of samples: R6G–SBA-16 and R6G–Ag@SBA-16. Then, the Raman response of samples was studied for different adsorbed amounts as well as the response of pure silica.

The adsorption isotherms of R6G onto SBA-16 and Ag@SBA-16 porous solids are presented in **Figure 2.9 (a)**. The construction of these isotherms using UV–vis spectroscopy in liquid phase is detailed *Appendix C*. They were derived from the spectra at the maximum of absorbance of R6G ($\lambda_{max} = 531$ nm). Initial concentrations of R6G in ethanol were varied from $1\,10^{-4}$ M to $1\,10^{-6}$ M. For both solids, a similar shape of isotherm can be observed and it corresponds to an *L*–type isotherm. [51] This type of adsorption isotherm is frequently found in the case of a homogeneous and narrow distribution of energetic adsorption sites. Furthermore, the initial affinity of R6G onto Ag@SBA-16 nanocomposite is reduced as compared to silica, as shown by the lower slope at low adsorbed amounts. This can be assigned to the difference of surface chemistry of the two samples.

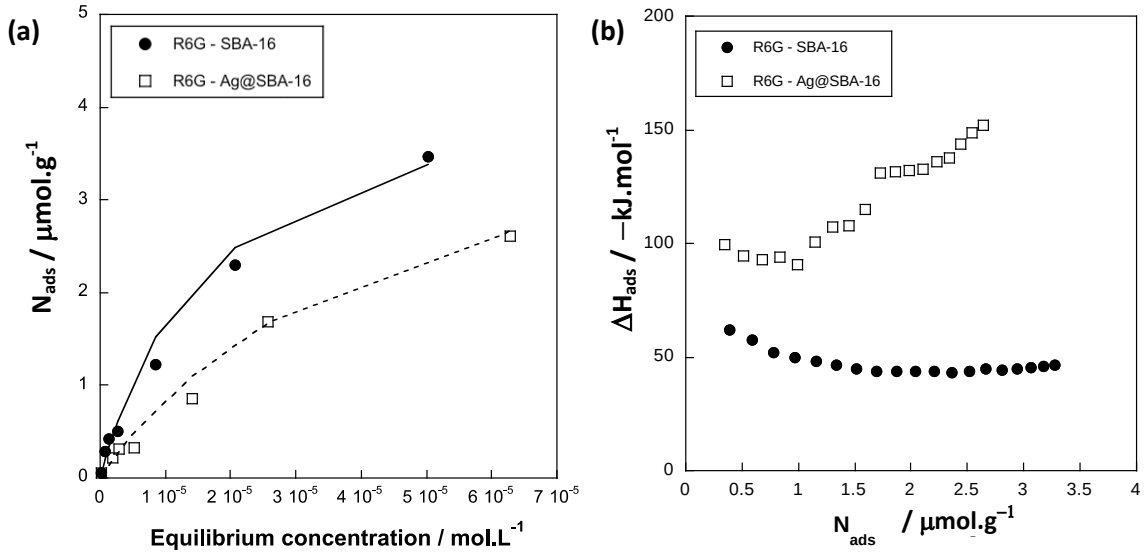

Figure 2.9*:* R6G adsorption isotherms onto SBA-16 and Ag@SBA-16 porous solids (a) and associated integral adsorption enthalpies (b).

The R6G adsorbed amounts at the highest equilibrium concentrations are around 3.5 and 2.5 µmol. g^{-1} for SBA-16 and Ag@SBA-16, respectively. This difference can be correlated to the decrease of the total adsorption capacity evidenced using nitrogen adsorption/desorption measurements for the Ag@SBA-16 sample. Furthermore, these maximum adsorbed amounts are in the range of those found in the case of adsorption of rhodamine B from aqueous solution on porous silica-based solids at an initial concentration of 1 10^{-4} M [62] but far (by a factor 10) from those described for the adsorption of rhodamine B from aqueous solution on functionalized hyper-cross-linked polymeric sorbent. [63]

The two isotherms presented in **Figure 2.9 (a)** can be related to the corresponding integral enthalpies of adsorption presented in **Figure 2.9 (b).** In the case of SBA-16, the variation of the enthalpy of adsorption (ΔH_{ads}) as a function of the adsorbed amount of R6G is quasi-constant. This behavior is characteristic of a single mechanism of adsorption with a homogeneous distribution of energetic sites. The associated value is close to -50 kJ. mol^{-1}, which corresponds to physisorption of R6G on the silica surface. This value can seem high for physisorption, but one has to remember that experiments are performed in ethanol as solvent in which the displacement of molecules is less endothermic than that in water. In the case of Ag@SBA-16, the value of the enthalpy of adsorption is quite constant and equal to -100 kJ. mol^{-1} from very low adsorbed amounts to 1.5 µmol. g^{-1}, then it increases up to -150 kJ. mol^{-1} for $N_{ads} = 2.6$ µmol. g^{-1}. The high initial value of enthalpy of adsorption as compared to the one found for silica can be explained in two different ways. It can be either attributed to strong interaction of π electrons of the R6G with Ag [64] or to interaction between silver surface and amine groups. [65] Furthermore, R6G molecules are known to form dimers in highly

concentrated solutions [66] and when they are incorporated in clays such as laponite [67] layered silicates [68] or spin-coated on silica surfaces. [69] They can form either H−type dimers (sandwich−type or head-to head structures) or J−type dimers (head-to-tail dimers). For the Ag@SBA-16 sample, knowing the amount of silver, the adsorbed amount of R6G per gram of silica, and the size of nanoparticles, one can estimate the number of R6G per square nanometer of silver along the isotherms: at very low adsorbed amounts (close to $0.05\ \mu mol.\ g^{-1}$), 0.1 molecule of R6G is calculated per nm^2 of Ag, whereas at high adsorbed amounts (close to $3\ \mu mol.\ g^{-1}$), 4 molecules of R6G are found. This last result means that R6G molecules probably form aggregates on the silver nanoparticle surface. This assumption is strengthened by the fact that values of integral enthalpies increase from adsorbed amounts close to $1.5\ \mu mol.\ g^{-1}$; this increase is a strong indication for an interaction between R6G molecules. Finally, this result is in agreement with the ones reported in the literature that evidence the formation of R6G dimers on Ag surface. [70]

Raman spectra of R6G, adsorbed on SBA-16 and Ag@SBA-16 porous solids, were recorded at different points of the adsorption isotherms using a 633 nm excitation wavelength, this wavelength being far from the plasmon band of silver nanoparticles ($\lambda = 400$ nm) and from the absorption band of R6G. The absorption spectrum of R6G in ethanol is presented in **Figure 2.10**.

Raman spectra for $N_{ads} > 1\ \mu mol.\ g^{-1}$ are presented in **Figure 2.11**: in all the spectra, characteristic bands of R6G are present. [71] The more intense bands are found at 610, 775, 1185, 1305, 1360, 1505, 1575, and 1650 cm^{-1}. They were indexed according to reference [71], as shown in **Table 2.2.** This means that even at a low equilibrium concentration, i.e. $1.13\ \mu mol.\ L^{-1}$ corresponding to an initial concentration of $2.5\ 10^{-5}\ mol.\ L^{-1}$, R6G is already detectable in the pure silica matrix without Ag nanoparticles, using only the preconcentration property of the porous solid.

This result clearly indicates the important necessity of studying the Raman response of the substrate itself (without Ag nanoparticles) to be sure that the observed signal is a SERS signal. This point is further evidenced by the quasi-linear evolution as a function of R6G adsorbed amounts on both solids of the Raman band intensity at $1360\ cm^{-1}$ that is assigned to C−C stretching of R6G's xanthene ring (**Figure 2.12**).

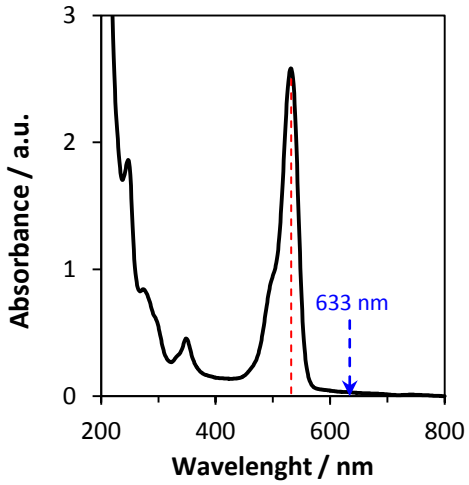

Figure 2.10: Absorption spectrum of R6G in ethanol in the UV-visible range.

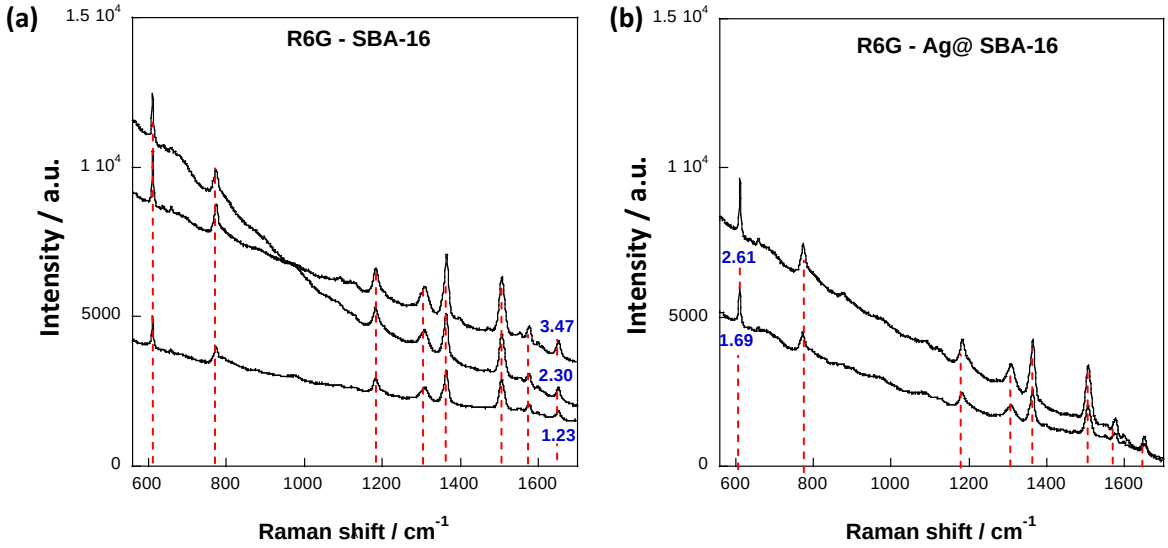

Figure 2.11: Raman spectra obtained at 633 nm for different adsorbed amounts of R6G ($N_{ads} > 1$ µmol. g^{-1}) onto SBA-16 (a) and Ag@SBA-16 (b) substrates. Adsorbed amounts in µmol. g^{-1} are given in blue.

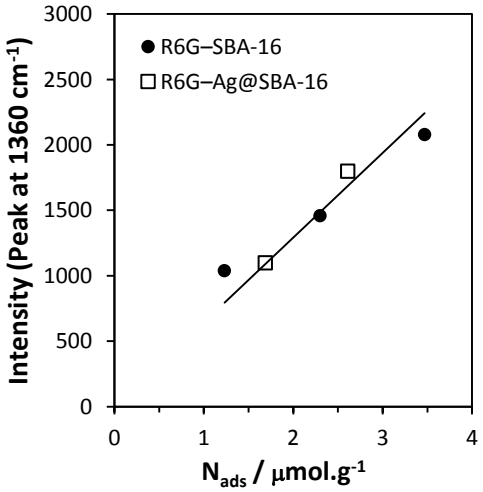

Figure 2.12*:* Evolution of the 1360 cm^{-1} C–C stretching mode (xanthene ring) as a function of the adsorbed amounts of R6G on porous solids.

Table 2.2: Position and assignment of observed Raman bands of R6G in methanol, polymethylcyanoacrylate and the SBA-16 based substrates (SBA-16 and Ag@SBA-16). [71]

Raman shifts of R6G in			Assignment
Methanol (cm^{-1})	**PMCA (cm^{-1})**	**SBA-16 substrates (cm^{-1})**	
613	614	610	C_x-C_x-C_x bend
628	625		Tor/C_x-C_x + N-H bend
777	777	775	C_x-H out-of-plane bend
852	850	875	H-C_e-H bend
890			C_x-C_x-H bend
936	932		C_x-C_x-C_x bend
1031	1033		C_e-H bend
1067	1073		C_m-H bend
	1131		C_x-H in-plane bend
1182	1181		C_x-C_x st
1188	1188	1185	C_e-C_e st + C_e-H bend
	1268		C_ϕ-C_ϕ st + C_x-C_x st + C_e-H bend
1312	1312	1305	C_x-H bend
1347	1348		C_x-C_x st + C_x-C_ϕ st
1366	1366	1360	C_x-C_x st
	1381		C_x-N st
	1419		C_x-C_x st + C_x-H bend
	1425		C_e-H bend
	1445	1454	C_e-H bend
	1474		C_e-H bend
1511	1512	1505	C_x-C_x st
	1578	1575	C_x-C_x st
1655	1654	1650	C_x-C_x st

a st and bend stand for stretching and bending modes
b Subscripts x, e, m, ϕ stand for the xanthene ring, ethylamine, methyl and phenyl group attached to the xanthene ring

Raman spectra obtained for $N_{ads} < 1\ \mu mol.\,g^{-1}$ are presented in **Figure 2.13 (a)** and **(b)** ($N_{ads} = 0.30\ \mu mol.\,g^{-1}$ and $0.05\ \mu mol.\,g^{-1}$ respectively). As the Raman band intensities are low compared to those presented in **Figure 2.11**, the Raman spectrum of the mesoporous silica matrix is also given for comparison (denoted as SBA-16 matrix). This spectrum exhibits three broad bands and two narrow bands (**Figure 2.13 (a)**). The 606 cm^{-1} band has been attributed to the breathing modes of the three-membered rings. The broad band, around 800 cm^{-1}, is

assigned to the overlapping transverse (TO) and longitudinal (LO) modes of the SBA-16 network motions. [72] The peak at 975 cm^{-1} is attributed to Si–O stretch of surface hydroxyl group.

The doublet appearing at 1369 and 1399 cm^{-1} on all the spectra of **Figure 2.13** is not a vibrational signature but is related to the electronic structure of silica. Generally, one has to use another excitation wavelength to check the vibrational or electronic origin of a given line. If this line's wavenumber calculated after replacing the laser at 0 cm^{-1} does not change, then it originates from vibration. If this line's wavenumber changes when changing the excitation wavelength, then it originates from the electronic structure. In our case, using an argon laser with $\lambda_L = 514$ nm, these two bands are found at 5003 and 5032 cm^{-1}, respectively, proving that they originate from electronic structure, with the corresponding energies 1.788 and 1.793 eV.

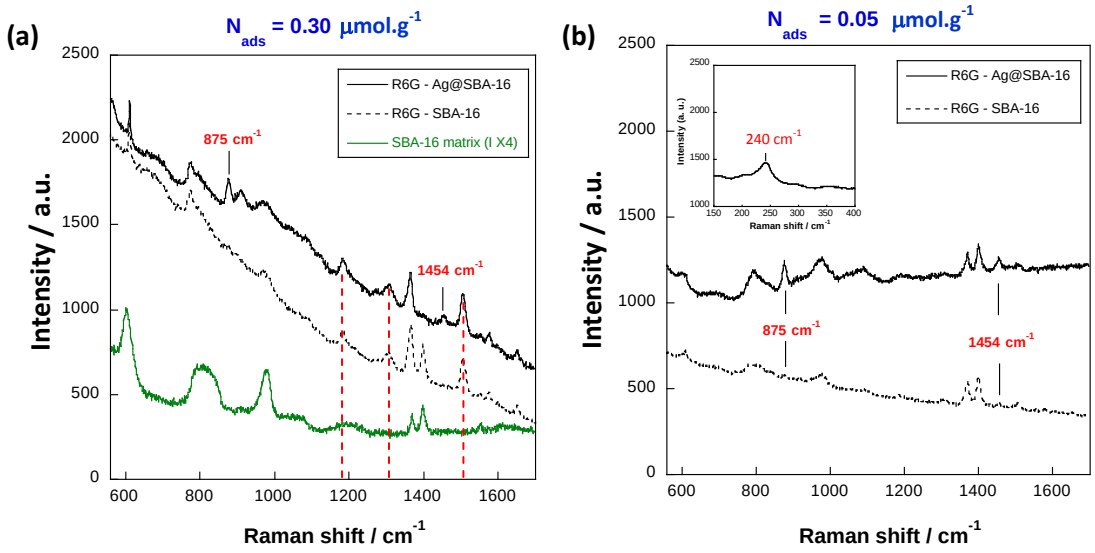

Figure 2.13*:* Comparison of Raman spectra obtained at 633 nm for R6G adsorbed on both solids with $N_{ads} = 0.3$ µmol. g^{-1} (a) and $N_{ads} = 0.05$ µmol. g^{-1} (b).

As shown in **Figure 2.13 (a)**, some Raman bands that are unambiguously characteristic of R6G molecules are present in both solids for adsorbed amounts close to 0.3 µmol. g^{-1}; they are located at 1185, 1305, and 1505 cm^{-1}. Furthermore, two additional bands are detected in the case of R6G adsorbed on Ag@SBA-16: one at 875 cm^{-1} assigned to H–C–H bending mode of ethylamine group attached to the xanthene ring and a second less intense band at 1454 cm^{-1} assigned to C–H bending mode of ethylamine group. For adsorbed amounts close to 0.05 µmol. g^{-1}, the two previously mentioned Raman bands of R6G are detected in the case of Ag@SBA-16 substrate, whereas they present a very low intensity in the case of silica. This value thus represents the detection limit of the Raman response of R6G without metallic nanoparticles in our experimental conditions. The ratio between the two Raman band intensities with and without Ag is roughly 10, which is close to the order of magnitude generally assumed for the

chemical enhancement mechanism. [12,15,16] In this way, the Raman bands of R6G that were first detected correspond to bending modes of amine groups. Furthermore, at lower wavenumbers, the Raman band corresponding to Ag–N stretching vibration is evidenced at 240 cm^{-1} (**Figure 2.13 (b)**) [73]; this observation gives a further indication that the adsorption of R6G on Ag nanoparticles takes place through the nitrogen of amine groups.

- In conclusion, no difference was observed in the Raman response of R6G adsorbed on SBA-16 and Ag@SBA-16 for $N_{ads} > 1\ \mu mol.\, g^{-1}$ (corresponding to $C_i \geq 5\ 10^{-6}\ mol.\, L^{-1}$). Therefore, the preconcentration properties of the porous silica matrix are sufficiently important to already detect R6G at an initial concentration close to $C_i = 5\ 10^{-6}\ mol.\, L^{-1}$ without silver nanoparticles.
- For very low adsorbed amounts ($N_{ads} = 0.05\ \mu mol.\, g^{-1}$), a ratio of roughly 10 was evidenced between the intensities with and without Ag of the Raman bands already present. This value is closed to the order of magnitude generally assumed for the chemical enhancement (CE) mechanism of SERS effect.
- Furthermore, Raman bands that are enhanced in the case of Ag@SBA-16 are assigned to bending modes of ethylamine groups. This result and the presence of a Raman band at 240 cm^{-1} corresponding to Ag–N stretching modes can be correlated to the thermodynamic parameters of the adsorption of R6G on Ag@SBA-16: the high values of integral adsorption enthalpies are certainly related to strong interactions between amine groups and Ag surface.

II.3.3. Towards the detection of molecules at low concentrations ($C_i < 1\ 10^{-6}$ M)

In the continuity of the study, another type of silica, SEO–type [74], whose synthesis procedure has been described in *Chapter 1*, will be investigated as substrate in a same way as in the preliminary study. This type of silica matrix has been selected for its ability of being easily tailored. Indeed, the pore size can be adjusted depending on the structure directing agent used during the synthesis. SEO will be studied in the same range of initial concentrations as for the SBA-16. Afterwards, in order to evaluate the influence of the metal nanoparticle chemical nature, the adsorption properties of R6G onto nanocomposites based of silver and gold nanoparticles will be studied similarly to their parent silica SEO. The R6G adsorption properties in ethanol of the different substrates (pristine silica and nanocomposites) will be studied for initial concentrations ranging from $1\ 10^{-4}$ M to $1\ 10^{-7}$ M.

II.3.3.a. Study of the adsorption of R6G on a new substrate

The new silica substrate, SEO, was characterized using various techniques previously in the *Chapter 1*. Especially, the textural properties of the porous matrix were investigated using nitrogen adsorption/desorption measurements, and are compared to those of SBA-16 in **Table 2.3**.

The adsorption isotherms of R6G onto SBA-16 and SEO substrates are presented in **Figure 2.14 (a)**. As for SBA-16 samples, the isotherm for SEO was derived from UV−vis spectra at R6G maximum of absorbance $\lambda_{max} = 531$ nm (cf. *Appendix C*). As for SBA-16, an *L*−type isotherm [51] is obtained for SEO. As mentioned earlier, this type of adsorption isotherm is frequently found for a homogeneous and narrow distribution of energetic adsorption sites. However, contrary to SBA-16, the SEO isotherm presents a saturation plateau at high equilibrium concentration. At the lowest equilibrium concentrations, i.e. below 10 µmol. L^{-1}, the isotherms present slightly different slopes and above this equilibrium concentration, the difference in adsorbed amounts of R6G in the SEO substrate is more significant. Indeed, much lower amounts are adsorbed as compared to the SBA-16 substrate. At the highest equilibrium concentrations, the R6G adsorbed amounts are around 3.5 µmol. g^{-1} and 1.7 µmol. g^{-1} for SBA-16 and SEO, respectively. These differences can be assigned to the lower specific surface area found for SEO matrix, **Table 2.3**. This feature of SEO can also explain the appearing saturation in the adsorbed amount which is traduced by the plateau at the end of the isotherm.

Table 2.3: Textural properties of SBA-16 and SEO samples.

Sample	S_{BET} [a] $/m^2.g^{-1}$	$V_{\mu porous}$ [b] $/cm^3.g^{-1}$	$V_{total\ pore}$ [c] $/cm^3.g^{-1}$	D_{pore} [d] /nm
SBA-16	580	0.04	0.50	4.5
SEO	430	0.05	0.50	8.5

a BET surface area
b Microporous volume
c Total pore volume
d Pore size at the maxima of pore size distribution

The SEO matrix isotherm presented can be related to the corresponding integral enthalpies of adsorption presented in **Figure 2.14 (a)**. The variation of the enthalpies of adsorption (ΔH_{ads}) as a function of the adsorbed amount of R6G in SEO–type silica is quasi-constant as it was observed for the SBA-16–type silica. This behavior is characteristic of a single mechanism of adsorption with a homogeneous distribution of energetic sites as mentioned earlier. The energies of interactions are close to -35 kJ. mol^{-1} and correspond to physisorption of R6G on the silica surface as explained previously. These values are lower than in the case of SBA-16 (-50 kJ. mol^{-1}) indicating a difference in the surface signature of the two types of silica.

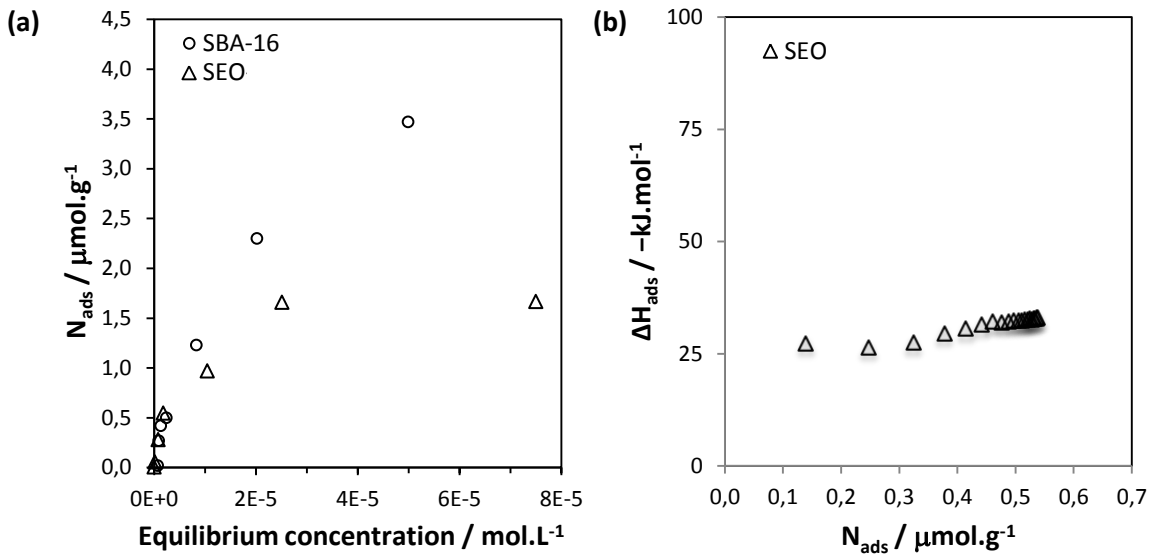

Figure 2.14: R6G adsorption isotherms onto SBA-16 and SEO porous solids (a) and associated integral adsorption enthalpies for SEO (b).

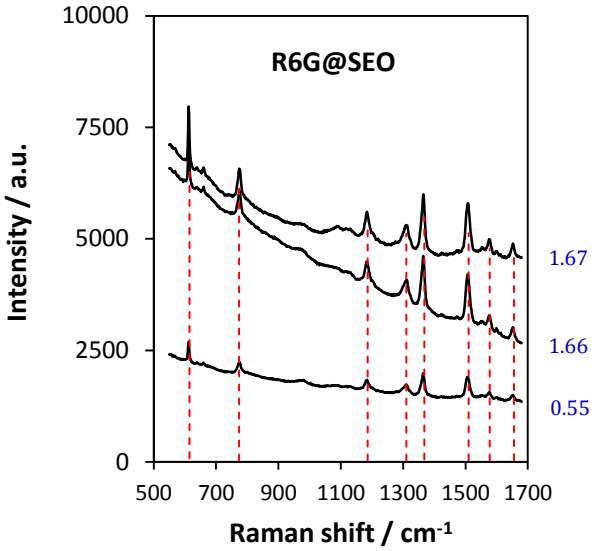

Figure 2.15: Raman spectra obtained at 633 nm for different adsorbed amounts of R6G ($N_{ads} \geq 0.5$ µmol. g^{-1}) onto SEO. Adsorbed amounts in µmol. g^{-1} are given in blue.

Similarly to the SBA-16 substrate, Raman spectra of R6G adsorbed on SEO substrates were recorded at different points of the adsorption isotherms, i.e. for R6G initial concentrations ranging from $1\,10^{-5}$ M to $1\,10^{-4}$ M, using a 633 nm excitation wavelength (**Figure 2.15**). The more intense bands, indexed according to reference [71] as previously (**Table 2.2**), are found at 612, 775, 1184, 1310, 1364, 1506, 1577 and 1651 cm^{-1} for $N_{ads} \geq 0.5$ µmol. g^{-1} (i.e. $C_i \geq 1\,10^{-5}$ mol. L^{-1}). The R6G bands displayed are slightly different than for the SBA-16 porous matrix: the deviation is roughly about 1 to 2 cm^{-1} for most of them and about 4 to 5 cm^{-1} for two of them. These little variations in wavenumbers can be assigned either to a

calibration effect or to weak interactions between the SEO surface and the R6G molecule not found in SBA-16–type silica.

From these results, three conclusions can be drawn:

- The first is that though lower R6G adsorbed amounts are obtained in the case of silica SEO, the adsorption mechanisms of R6G onto both substrates are basically identical.
- The second is that the type of silica does not affect the Raman response of the adsorbed R6G.
- The last but not least is that the R6G can be detected in the SEO substrate for initial concentrations starting from $N_{ads} = 0.55\ \mu mol.\ g^{-1}$ (i.e. $C_i = 1\ 10^{-5}$ M) without the presence of noble metal nanoparticles in the matrix.

II.3.3.b. Influence of the chemical nature of the metal on the properties of adsorbed R6G

In this subsection, the adsorption properties of R6G onto nanocomposites based of silver and gold nanoparticles will be studied similarly to their parent silica in order to evaluate the influence of the metal chemical nature on adsorption properties and Raman response. The initial R6G concentrations vary from $1\ 10^{-4}$ M to $1\ 10^{-7}$ M but the Raman response study of R6G in the different nancomposites will be divided in two steps: first for $C_i \geq 1\ 10^{-5}$ M then for $C_i \leq 1\ 10^{-5}$ M in the next subsection.

The silica SEO was used as host matrix to synthesize the two types of substrates, namely Ag@SEO and Au@SEO, by means of chemical reduction in gas phase after impregnation with silver or gold salt solution for 12 h, as detailed in the previous section.

The textural and structural properties of the two nanocomposites were investigated using various techniques of characterization.

The samples were first characterized using nitrogen adsorption/desorption measurements at 77 K. The isotherms of Ag@SEO and Au@SEO (not shown herein) have the same shape as the parent silica one: they are characterized as mixed type *I* and *IV* and present a hysteresis loop of type *H1*. Their textural properties are summarized in **Table 2.4**. The nanocomposite Ag@SEO presents the same porous volumes as SEO, while its specific surface area is lower (~ -9 %). For Au@SEO, a decrease in the specific surface area and the porous volumes is observed as compared to SEO. Thus, the presence of the noble nanoparticles reduces the silica matrix textural properties probably due to pore blocking effect caused by the presence of particles in the pores (this is also observable on the shift of the isotherms to lower values during the measurements).

Transmission electron microscopy permits the identification of spherical nanoparticles of silver and gold that are homogeneously distributed within the silica host matrix (**Figure 2.16** and **Figure 2.17**). The size of silver and gold particles is about 6 nm with a standard deviation around 1 nm. The mesopore size (8 – 9 nm) remains unchanged with the incorporation of the noble metal nanoparticles which is in good agreement with the nitrogen adsorption/desorption measurements.

According to inductive coupled plasma – mass spectrometry (ICP–MS) measurements, the silver and gold loadings in the silica host matrix were estimated to be close to 1.3 mg and 0.7 mg per gram of silica, corresponding to a mass percentage of 0.13 wt% and 0.07 wt%.

Table 2.4: Textural properties of the nanocomposites Ag@SEO and Au@SEO.

Sample	S_{BET} [a] $/m^2.g^{-1}$	$V_{\mu porous}$ [b] $/cm^3.g^{-1}$	$V_{total\ pore}$ [c] $/cm^3.g^{-1}$	D_{pore} [d] /nm
Ag@SEO	390	0.05	0.50	8.5
Au@SEO	320	0.02	0.50	8.5

a BET surface area **c** Total pore volume
b Microporous volume **d** Pore size at the maxima of pore size distribution

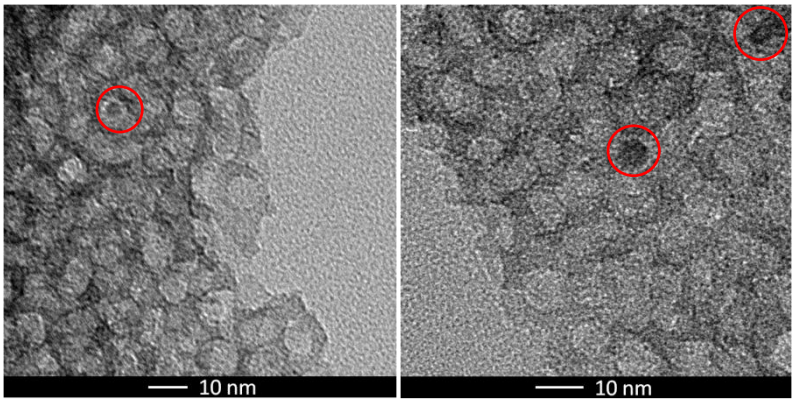

Figure 2.16: TEM images of the nanocomposite Ag@SEO. Red circles show Ag nanoparticles.

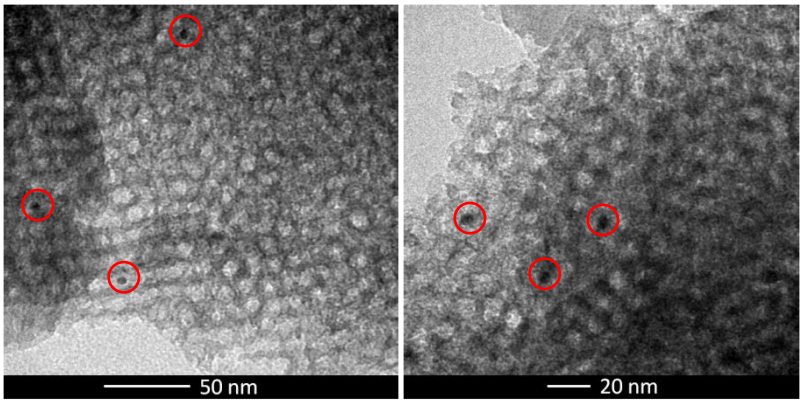

Figure 2.17: TEM images of the nanocomposite Au@SEO. Red circles show Au nanoparticles.

UV–visible spectroscopy enables to locate the plasmon resonance band of the nanocomposite samples. For the sample Ag@SEO, the plasmon band is centered on 400 nm and the one of Au@SEO was found to be centered on 520 nm, as shown in **Figure 2.18**. These resonances are typical for isolated or confined (in porous silica) silver [61] and gold [75] nanoparticles.

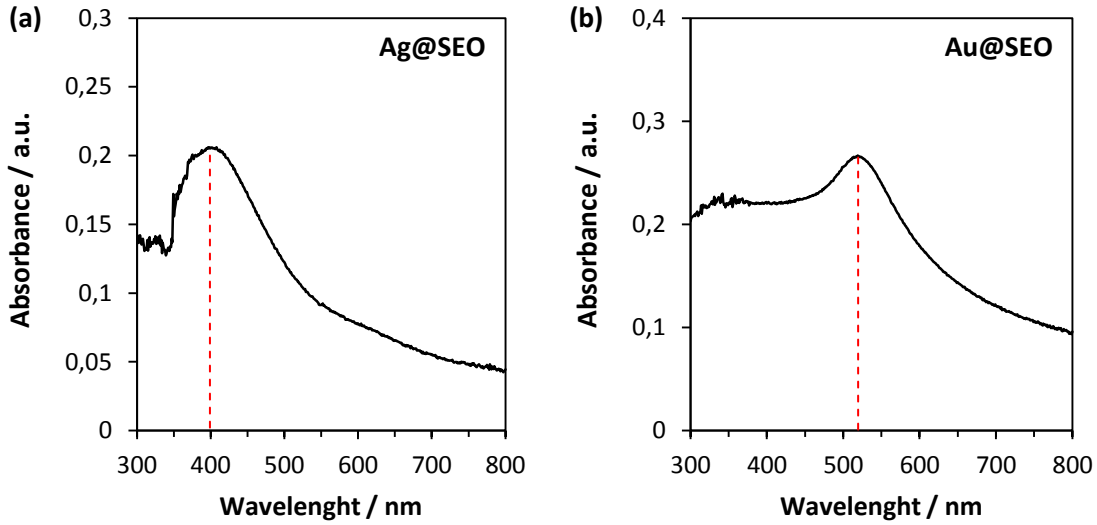

Figure 2.18: Absorption spectra of the nanocomposites Ag@SEO (a) and Au@SEO (b).

In conclusion, the specific configuration set for the nanocomposite in the preliminary study, i.e. 'small and low concentration of nanoparticles with a homogeneous distribution', was achieved within the SEO–type matrix. This will allow studying the influence of the presence of silver and gold nanoparticles in a silica substrate on the Raman response (preventing inter-particle interactions and 'hot spots').

The R6G adsorption on the nanocomposite substrates was studied primarily from a thermodynamic point of view in ethanol, as for the pristine material. Then, using a 633 nm excitation wavelength, the Raman response of the two systems, R6G–Ag@SEO and R6G–Au@SEO, was studied for different R6G adsorbed amounts correlated to initial concentrations ranging from $1\ 10^{-5}$ M to $1\ 10^{-4}$ M.

The adsorption isotherms of R6G onto Ag@SEO and Au@SEO porous solids are presented above in **Figure 2.19 (a)**. As previously, the isotherms were derived from UV–vis spectra at R6G maximum of absorbance $\lambda_{max} = 531$ nm (cf. *Appendix C*). For both solids, *L*–type isotherms [51] with ending saturation plateaus can be observed similarly to pristine SEO. At equilibrium concentrations lower than 10 µmol. L^{-1}, the adsorbed amounts of R6G in the substrates are close but the initial adsorption affinity of R6G on Au@SEO substrate is reduced as compared to the one found for Ag@SEO. Furthermore, above the equilibrium concentration of 10 µmol. L^{-1}, the

amounts of R6G adsorbed in Au@SEO are lower than those in Ag@SEO. The R6G adsorbed amounts at the highest equilibrium concentrations are estimated about 1.6 µmol. g^{-1} and 1.0 µmol. g^{-1} for Ag@SEO and Au@SEO respectively. This tendency is in good agreement with nitrogen adsorption/desorption measurements that show lower total adsorption capacity for the nanocomposite based of gold nanoparticles (**Table 2.4**).

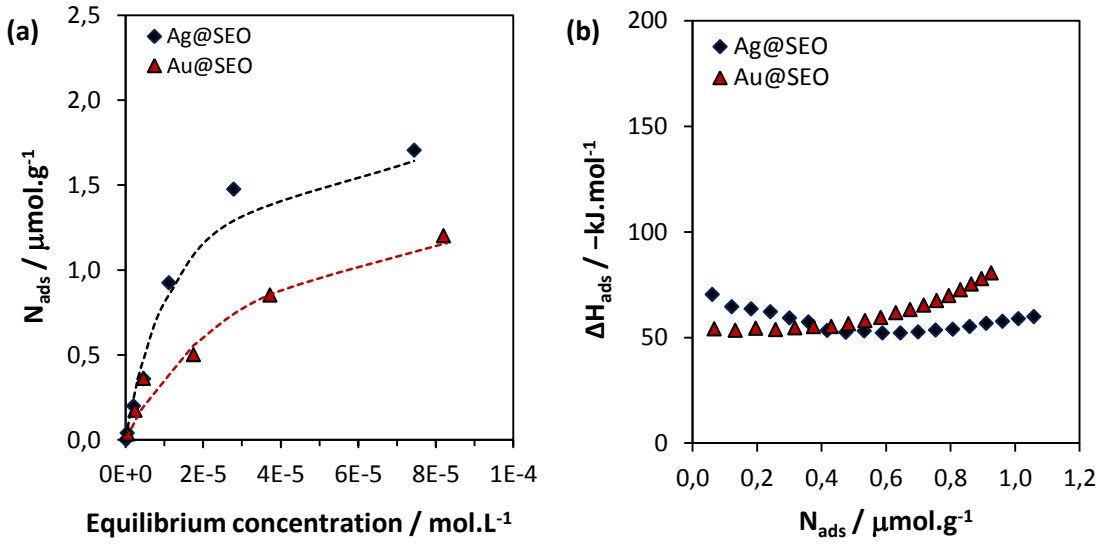

Figure 2.19: R6G adsorption isotherms onto Ag@SEO and Au@SEO porous solids (a) and associated integral adsorption enthalpies (b).

The integral enthalpies of adsorption (ΔH_{ads}) related to the two R6G adsorption isotherms corresponding to each type of nanocomposites are presented in **Figure 2.19 (b)**.The samples present different behaviors during adsorption process. Similarly to the silica parent, the variation of the enthalpies of adsorption for Ag@SEO is nearly constant (decreases slightly at the beginning up to reach a constant value): it is about -70 kJ. mol^{-1}. This behavior is characteristic of a single mechanism of adsorption with a homogeneous distribution of energetic sites. In the case of Au@SEO, the enthalpies of adsorption are quite constant and equal to -55 kJ. mol^{-1} from very low adsorbed amounts to 0.5 µmol. g^{-1}, then it increases up to-80 kJ. mol^{-1} for $N_{ads} = 0.95$ µmol. g^{-1} indicating the presence of interactions between R6G molecules. Thus, for low adsorbed amounts the interaction is less energetic in the case of Au@SEO substrate compared to Ag@SEO one.

Raman spectra of R6G adsorbed onto Ag@SEO and Au@SEO substrates were recorded at different points of the adsorption isotherms, i.e. for $N_{ads} \geq 0.3$ µmol. g^{-1} (corresponding to R6G initial concentrations ranging from 1 10^{-5} M to 1 10^{-4} M using a 633 nm excitation wavelength, similarly to SEO (**Figure 2.20**). The Raman spectra were shift on the y-axis in order to facilitate the comparisons, thus no intensity values are shown on the diagram axes.

For both substrates, the more intense bands are found at the same wavenumbers as for the SEO parent: 612, 775, 1184, 1310, 1364, 1506, 1577 and 1651 cm^{-1}. Besides, a quasi-linear evolution of the Raman band intensity at 1364 cm^{-1}, assigned to C–C stretching of R6G's xanthene ring, as a function of R6G adsorbed amounts on both nanocomposite substrates is observed, as shown on **Figure 2.21**. First, these comparisons confirm that the intensities of the bands are directly related to the adsorbed amount of R6G as it was previously demonstrated with SBA-16 substrates. Besides, it shows that for $N_{ads} \geq 0.3$ µmol. g^{-1} the chemical nature of the metal does not fundamentally affect the Raman response of R6G in the substrates.

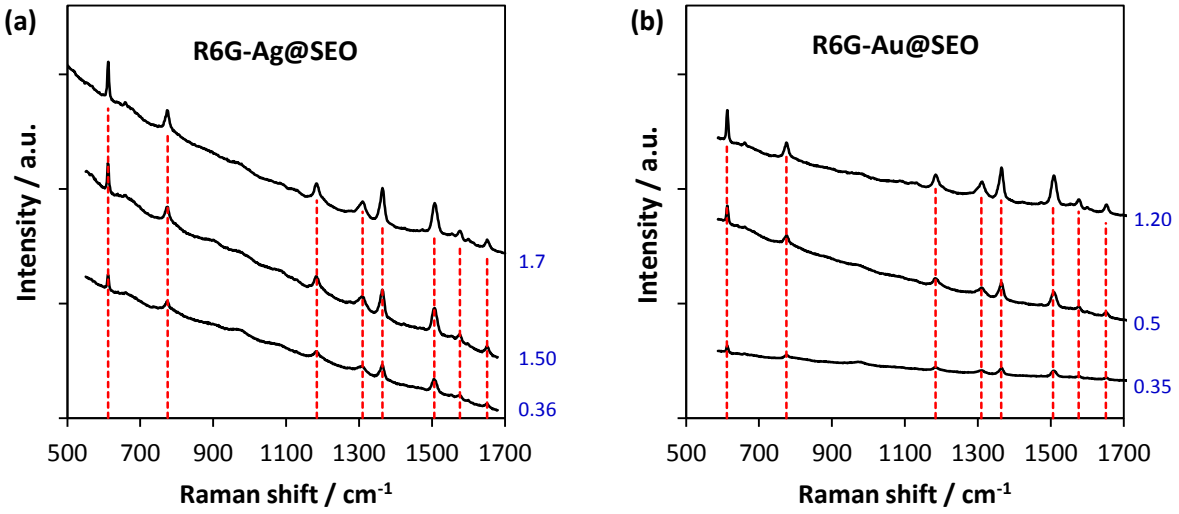

Figure 2.20: Raman spectra obtained at 633 nm for different adsorbed amounts of R6G ($N_{ads} \geq 0.3$ µmol. g^{-1}) onto Ag@SEO (a) and Au@SEO (b) porous solids. Adsorbed amounts in µmol. g^{-1} are given in blue.

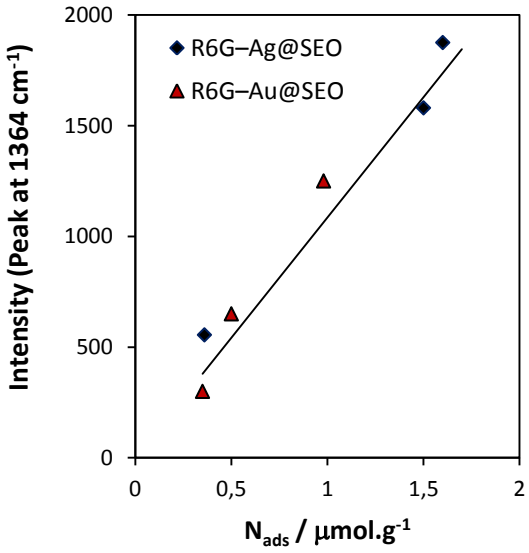

Figure 2.21: Evolution of the 1364 cm^{-1} C–C stretching mode (xanthene ring) as a function of the adsorbed amounts of R6G on porous solids.

- In conclusion, no differences were observed in the Raman response of R6G adsorbed onto silver and gold-based nanocomposites for $N_{ads} \geq 0.3\ \mu mol.\ g^{-1}$ (corresponding to $C_i \geq 1\ 10^{-5}$ M).

II.3.3.c. Raman response of R6G adsorbed at low concentrations on different substrates

To go deeper in the study, the Raman response of R6G adsorbed on different substrates was investigated for initial concentrations equal to $1\ 10^{-6}$ M and $1\ 10^{-7}$ M. For this purpose, a fourth type of substrate was also prepared. It consists in a SEO matrix in which the silver impregnation process was performed twice. More precisely, after the first impregnation then reduction, the sample was soaked again in silver nitrate solution for 12 h, washed and thermally treated under Ar/H_2 gas mixture at 150°C for 1 h.

The textural properties and TEM images of this nanocomposite, denoted as Ag@SEO-DI (DI standing for double impregnation), are presented in **Table 2.5** and **Figure 2.22**, respectively.

The nitrogen adsorption/desorption isotherm at 77 K of Ag@SEO-DI (not shown herein) has the same shape as the parent silica one (mixed type *I* and *IV* with *H1*–type hysteresis loop). This nanocomposite Ag@SEO-DI presents a comparable value of specific surface area to that of Ag@SEO.

Table 2.5: Textural properties of the nanocomposite Ag@SEO-DI.

Sample	S_{BET} [a] $/m^2.g^{-1}$	$V_{\mu porous}$ [b] $/cm^3.g^{-1}$	$V_{total\ pore}$ [c] $/cm^3.g^{-1}$	D_{pore} [d] /nm
Ag@SEO-DI	385	0.05	0.50	8

a BET surface area
b Microporous volume
c Total pore volume
d Pore size at the maxima of pore size distribution

Transmission electron microscopy permits the identification of spherical silver nanoparticles within the silica host matrix (**Figure 2.22**)**.** The particle size is about 7 nm with a standard deviation around 1 nm. The presence of particles with a mean size around 15 nm is also observed in this sample. The mesopore size remains basically unchanged except upon the incorporation of these bigger nanoparticles in which case it seems to be increased. This was not detectable from nitrogen adsorption/desorption measurements; indeed no significant change in pore size was observable.

Adsorbed amounts of R6G onto the different substrates, i.e. SEO, Ag@SEO, Ag@SEO-DI and Au@SEO, at initial concentrations equal to $1\ 10^{-6}$ M and $1\ 10^{-7}$ M, are given in **Table 2.6**. As

previously, adsorbed amounts were derived from UV–vis spectra at R6G maximum of absorbance $\lambda_{max} = 531$ nm (cf. *Appendix C*). As the adsorbed amounts are low, the reported values correspond to the average of at least three experiments.

As a general trend, the adsorbed amounts of R6G are lower in the nanocomposites as it was observed at higher initial concentrations; probably due to the decreased textural properties as compared to the pristine silica.

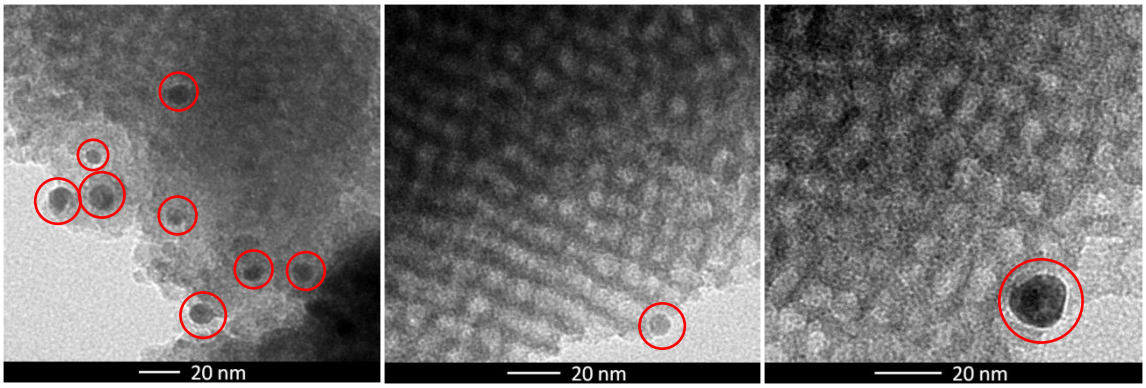

Figure 2.22: TEM images of the nanocomposite Ag@SEO-DI.

Table 2.6: Adsorbed amounts of R6G onto the different substrates with initial concentrations equal to 1 10 $^{-6}$ M and 1 10 $^{-7}$ M.

	Adsorbed amounts of R6G / µmol. g^{-1}			
Concentration	**SEO**	**Ag@SEO**	**Ag@SEO-DI**	**Au@SEO**
$C_i = 1\ 10^{-6}\ M$	$(6 \pm 0.2)\ 10^{-2}$	$(3.5 \pm 0.2)\ 10^{-2}$	$(3.5 \pm 0.2)\ 10^{-2}$	$(4 \pm 0.2)\ 10^{-2}$
$C_i = 1\ 10^{-7}\ M$	$(7 \pm 1)\ 10^{-3}$	$(3 \pm 1)\ 10^{-3}$	$(2 \pm 1)10^{-3}$	$(7 \pm 1)\ 10^{-3}$

Study of the Raman response of adsorbed R6G starting from $C_i = 1\ 10^{-6}$ M

As shown in **Figure 2.23**, the Raman response of adsorbed R6G can be divided in two groups depending on substrates:

- For R6G–SEO and R6G–Au@SEO: the Raman spectrum exhibit some of the bands that were previously found for high adsorbed amounts (**Figure 2.15** and **Figure 2.20**), one at 1365 cm^{-1} and one at 1507 cm^{-1}. One can notice that the bands are slightly shifted as compared to higher initial concentrations.
- For R6G–Ag@SEO and R6G–Ag@SEO-DI, the Raman bands found are located at 875 cm^{-1} and 1455 cm^{-1}, corresponding to the C–H bending of ethylamine groups attached to the xanthene ring. Furthermore, the band corresponding to Ag–N stretching vibration (240 cm^{-1}) is also evidenced.

The presence of these two groups can be explained considering the interaction between R6G molecules and the substrate. In the case of silver containing substrates, as evidenced with Raman results, R6G molecules interact with silver via ethylamine groups and high adsorption enthalpies were determined ($\Delta H_{ads} = -70$ kJ. mol^{-1}). In the other case, no specific interactions were evidenced using Raman spectroscopy and calorimetric measurements.

Raman band intensities of R6G adsorbed onto each substrate are given above in **Table 2.7**. As shown in this table, regarding to intensities in SEO lower than for nanocomposites, the highest band intensities are those found with silver-based substrates for the bands located at 875 and 1455 cm^{-1}. One has to remember that these highest intensities are associated with the lowest adsorbed amounts of R6G (0.035 µmol. g^{-1}). Thus, starting from an initial concentration of 1 10 $^{-6}$ M, the Raman intensity is no more linearly correlated to the adsorbed amounts in the substrates.

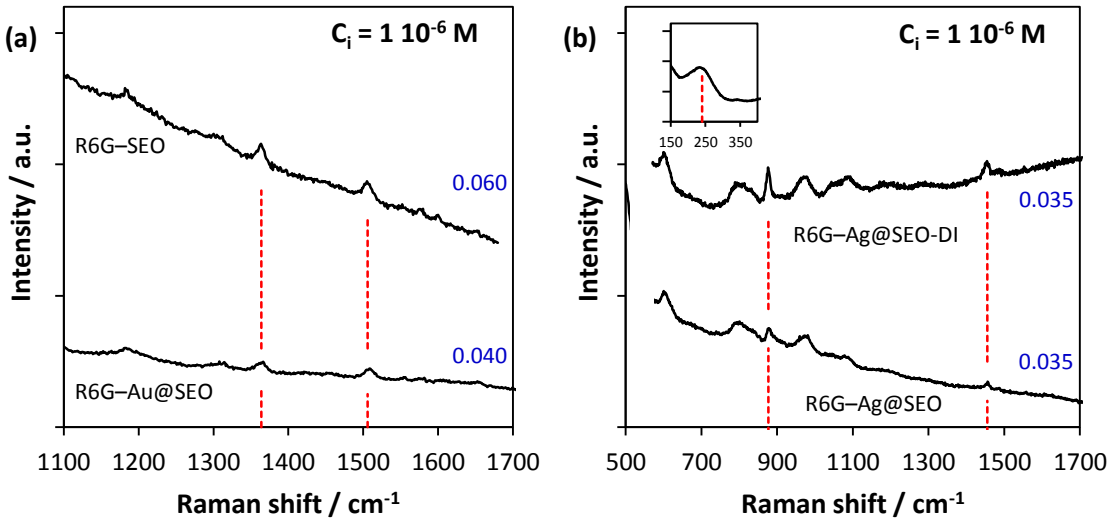

Figure 2.23: Raman spectra obtained at 633 nm for R6G adsorbed on SEO and Au@SEO (a) and Ag@SEO and Ag@SEO-DI (b) substrates with $C_i = 1\ 10^{-6}$ M. Adsorbed amounts in µmol. g^{-1} are given in blue.

Table 2.7: Intensity of Raman bands located at 875, 1365, 1455 and 1507 cm^{-1} for SEO, Ag@SEO, Ag@SEO-DI and Au@SEO.

$C_i = 1\ 10^{-6}\ M$	Intensity / a.u.			
	SEO	**Ag@SEO**	**Ag@SEO-DI**	**Au@SEO**
Raman band at 875 cm^{-1}	0	40	120	0
Raman band at 1365 cm^{-1}	70	0	0	30
Raman band at 1455 cm^{-1}	0	20	55	0
Raman band at 1507 cm^{-1}	70	0	0	40
N_{ads} / µmol. g^{-1}	0.060	0.035	0.035	0.040

Study of the Raman response of adsorbed R6G starting from $C_i = 1\ 10^{-7}$ M

The Raman response of adsorbed R6G starting from an initial concentration equal to $1\ 10^{-7}$ M is different than the one determined for $C_i = 1\ 10^{-6}$ M. Indeed, in this case, the spectra obtained for the four substrates are similar: two bands are evidenced at 875 and 1455 cm^{-1} (**Figure 2.24**). The Raman intensities of these two bands were determined for each substrate and are reported in **Table 2.8**.

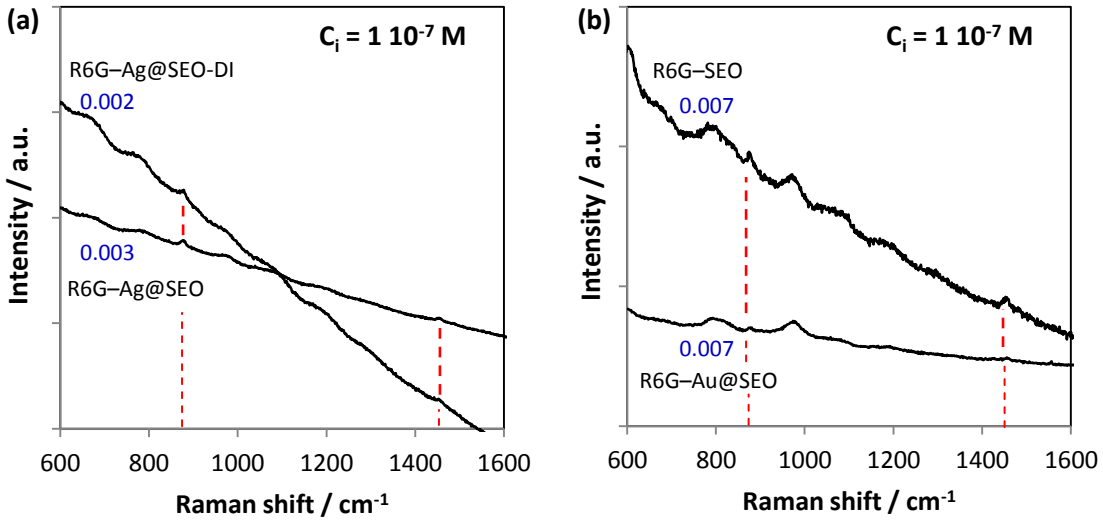

Figure 2.24: Raman spectra obtained at 633 nm for R6G adsorbed on SEO and Au@SEO (a) and Ag@SEO and Ag@SEO-DI (b) substrates with $C_i = 1\ 10^{-7}$ M. Adsorbed amounts in µmol. g^{-1} are given in blue.

Table 2.8: Intensity of Raman bands located at 875 cm^{-1} and 1455 cm^{-1} for each substrate.

$C_i = 1\ 10^{-7}\ M$	Intensity / a.u.			
	SEO	**Ag@SEO**	**Ag@SEO-DI**	**Au@SEO**
Raman band at 875 cm^{-1}	40	140	230	10
Raman band at 1455 cm^{-1}	40	75	85	10
N_{ads} / $\mu mol.\ g^{-1}$	0.007	0.003	0.002	0.007

The analysis of results presented in **Table 2.8** permits to have the following comments:

- Starting from this initial concentration, the Raman intensity is no more linearly correlated to the adsorbed amounts. Indeed, the highest intensity is found for the lowest value of N_{ads} (corresponding to Ag@SEO-DI substrate).
- An enhancement of Raman band intensities is found for silver-based nanocomposites. This enhancement is particularly more pronounced for the band at 875 cm^{-1} and for the Ag@SEO-DI substrate. Even if it is not possible to calculate the enhancement factor properly

as the adsorbed amounts are different, the intensity is multiplied by a factor of 6 for this Raman band, as compared to the pristine material. This is characteristic of the chemical enhancement.

- For Au-based nanocomposite, intensities are lower than the pure SEO ones.

These results clearly emphasize the role played by the interaction between R6G molecules and the substrate: when this interaction is not specific, Raman band intensities are low whereas when this interaction is more specific, the intensities are enhanced. Furthermore, the observed differences in the case of Ag-based substrates could be explained considering the difference in size of Ag nanoparticles. Indeed, in the case of double impregnation process, two populations of incorporated Ag nanoparticles were found, one with a mean diameter of 8 nm and a second with 15 nm. One can suppose that the interaction between R6G molecules and silver is strengthened is the case of larger particles.

- In conclusion, the presence of gold nanoparticles does not particularly help for a better detection of R6G; at contrary, the signal is found to be lowered as compared to SEO matrix at $C_i = 1\ 10^{-6}$ M ($N_{ads} = 0.007\ \mu mol.\ g^{-1}$) and $C_i = 1\ 10^{-7}$ M ($N_{ads} = 0.04\ \mu mol.\ g^{-1}$).
- For silver-based nanocomposites, at both initial concentrations $C_i = 1\ 10^{-6}$ M and $1\ 10^{-7}$ M, the Raman signal of the R6G could be enhanced. Besides the bigger the particle size the higher the enhancement of the Raman response of R6G.

II.3.4. Influence of other experimental parameters on the Raman response

In this part, the excitation wavelength and the molecule of interest will be modified in order to study the influence of these parameters on the detection capacity.

II.3.4.a. Influence of the excitation wavelength

In this subsection, the aim is to study the influence of the excitation wavelength on the Raman response of R6G adsorbed on the substrates SEO and Ag@SEO. The analysis was performed with an excitation wavelength of 405 nm. This wavelength is close to the plasmon resonance band of silver nanoparticles ($\lambda = 400$ nm).

The Raman spectra of R6G adsorbed onto SEO and Ag@SEO were recorded at an initial concentration equal to $C_i = 1\ 10^{-6}$ M. Two bands appear at 878 and 1455 cm^{-1} for both substrates as found for at 633 nm. However as shown on **Figure 2.25**, the Raman response is more visible in the pristine material than in the nanocomposite. This clearly evidences that the

plasmon band of silver nanoparticles disturbs the signal since at the same initial concentration an enhanced Raman signal could be observed at 633 nm for the silver-based nanocomposite.

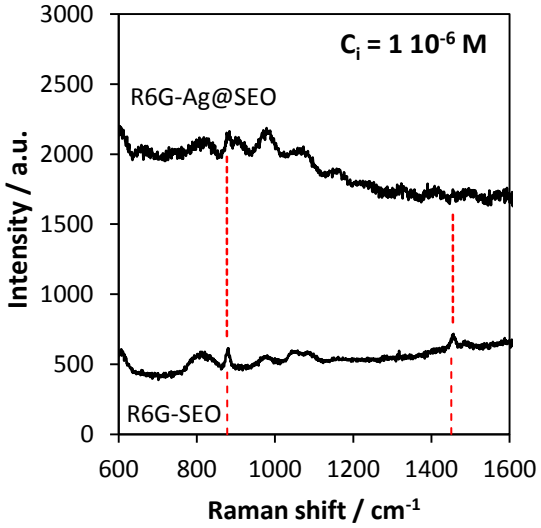

Figure 2.25: Raman spectra obtained at 405 nm for R6G adsorbed onto SEO and Ag@SEO substrates with $C_i = 1\ 10^{-6}$ M

II.3.4.b. Influence of the model molecule

In this subsection, the aim is to study the adsorption and the Raman response of another model molecule on the substrate SEO: the methylene blue (MB). The adsorption properties of the substrate towards MB will be first presented then the Raman response will be studied.

The adsorption isotherm of MB onto SEO is presented in **Figure 2.26 (a)**. Initial concentration range in water was $1\ 10^{-6}\ \text{M} < C_i < 1\ 10^{-3}\ \text{M}$. Similarly to previously, the isotherm was derived from UV–vis spectra at MB maximum of absorbance $\lambda_{max} = 665$ nm (cf. *Appendix C*). One can observe that there is a high affinity between SEO and MB which is evidenced by a sharp increase of adsorbed amount at the beginning of the isotherm (type *H*), i.e. $C_i < 1\ 10^{-5}$ M. Indeed, all MB was adsorbed after impregnation at these concentrations (the supernatants were transparent).

Raman spectra of MB adsorbed onto SEO were recorded at different initial concentrations with an excitation wavelength of 514 nm. This wavelength was chosen especially because it was not located on the absorption band of MB as shown in **Figure 2.26 (b)**.

For initial concentrations $C_i < 1\ 10^{-4}$ M, it was not possible to detect MB although quite high adsorbed amounts were achieved, i.e. $1 < N_{ads} < 6\ \mu\text{mol.g}^{-1}$. The MB started to be detectable in the substrate at an initial concentration $C_i = 1\ 10^{-4}$ M corresponding to $N_{ads} = 6\ \mu\text{mol.g}^{-1}$.

Indeed, one band which is unambiguously characteristic of MB was visible at 1627 cm^{-1}, **Figure 2.27**. This band is assigned to the N-H bending mode of MB [76].

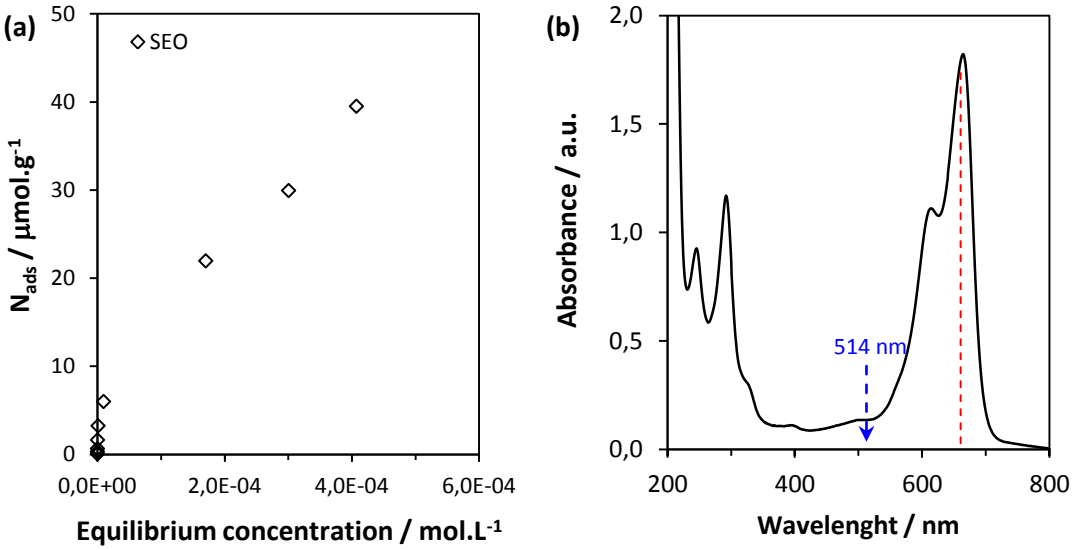

Figure 2.26: MB adsorption isotherm onto SEO porous solid (a) and its absorption spectrum in water in the UV-visible range (b).

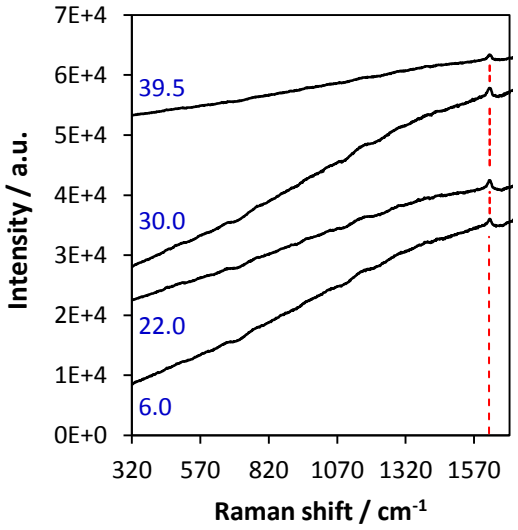

Figure 2.27: Raman spectra obtained at 514 nm for MB adsorbed on SEO substrate at $1\ 10^{-4}\ M < C_i < 1\ 10^{-3}\ M$. Adsorbed amounts in µmol. g^{-1} are given in blue.

In summary, these two studies drew to the following conclusions:

- The excitation wavelength influences the Raman response of R6G: if it is close to the plasmon band of the metal nanoparticles incorporated in the silica matrix, the Raman signal is disturbed.

- Although MB adsorbed amounts were quite high, it was not possible to detect it easily: the Raman response of MB is less strong (in terms of band intensity) as compared to R6G. This clearly emphasizes the importance of the cross section of the molecule of interest. One has to remember that the cross section expresses the Raman scattering efficiency of a molecule in a manner analogous to describing light absorption through the absorption cross section.

Therefore, it can be concluded that the detection of a molecule at low concentration depends not only on the substrate used for the detection but also on the experimental conditions and the intrinsic properties of the molecule of interest.

Summary and prospects

In conclusion, the Raman response of R6G adsorbed on the different solids synthesized was studied at $\lambda = 633$ nm at different points of adsorption isotherms that correspond to different adsorbed amounts per gram of solids (N_{ads}).

It was evidenced that, for initial concentrations $C_i \geq 5\ 10^{-6}$ M (corresponding to $N_{ads} > 1\ \mu mol.g^{-1}$), no difference was observed in the Raman response of R6G adsorbed on SBA-16 and Ag@SBA-16. This result clearly highlights that the preconcentration properties of porous pristine SBA-16 are sufficiently important to already detect R6G without considering the presence of Ag nanoparticles. This is not the case for very low adsorbed amounts ($N_{ads} = 0.05\ \mu mol.g^{-1}$). Indeed, a ratio of roughly 10 was evidenced between the intensities with and without silver of the Raman bands already present and this is assumed for the chemical enhancement (CE) mechanism of SERS effect.

The detection of R6G adsorbed in the new silica substrate SEO was studied. Similarly to SBA-16, the preconcentration properties of SEO enabled detecting R6G without the presence of noble metal nanoparticles (silver and gold) incorporated for initial concentrations $C_i \geq 1\ 10^{-5}$ M ($N_{ads} \geq 0.5\ \mu mol.g^{-1}$). Concerning the silver and gold-based nanocomposites, starting from this initial concentration ($N_{ads} \geq 0.3\ \mu mol.g^{-1}$), no differences could be observed between the nanocomposites materials.

At lower concentrations, i.e. $C_i = 1\ 10^{-6}$ M and $1\ 10^{-7}$ M, the Raman response of SEO, Ag@SEO, Au@SEO and a new substrate Ag@SEO-DI (double impregnation) was studied. The conclusions drawn are:

- The presence of gold nanoparticles in SEO matrix was found to lower the Raman signal as compared to SEO;

- The presence of silver nanoparticles in SEO matrix enhanced the Raman signal and bigger silver particles in the SEO matrix (i.e. Ag@SEO-DI sample) showed higher enhancement of the Raman response of R6G. Indeed, the intensity was found to be multiplied by a factor of approximately 6 as compared to the pristine material, which is characteristic of the chemical enhancement.

Investigation of the influence of two parameters was also performed during this work: the excitation wavelength and the molecule of interest. First, it has been evidence that at an initial concentration of $C_i = 1\ 10^{-6}$ M, as compared to the case with an excitation wavelength which is far from the plasmon band of incorporated silver nanoparticles, the study the Raman response of R6G at an excitation wavelength which is close to the latter did not permit having a better detection of the molecule, at contrary it was disturbed. Besides, the Raman signal was observed to be shifted in these conditions. Second, the importance of the molecule cross section to be detected has been revealed. Indeed, the study of MB adsorbed on pristine silica emphasized that even if the substrate possessed a high affinity with the molecule (very high adsorbed amounts since low initial concentrations, *H*–type isotherm) the detection of the latter was not so obvious. Indeed, the lower cross section characteristic of MB as compared to R6G might be the origin for such weak Raman signal.

The detection of molecule at low concentrations is an application which is very sensitive to the analysis procedure. Indeed, the setting of the different parameters is not an easy task since the signal depends not only on the substrate used to detect the molecule of interest but also on several parameters such as the excitation wavelength, the molecule cross section, and so on.

Being able to handle all important parameters influencing the signal will help exceeding the detection limit encountered nowadays. For this purpose, studying different molecule–substrate systems by varying the parameters would be interesting.

In future work, the size of both silver and gold nanoparticles will be increased in order to study the influence of this parameter on the Raman response at low concentrations. It would be interesting in future analyses to use other model molecules such as pure or thiol- and amino-modified pyridines, or aminothiophenols, in order to focus on the influence of 'molecule–nanoparticle' interactions on the Raman response and adsorption properties.

References

[1] K. Kneipp, H, Kneipp, I. Itzkan, et al., *Curr. Sci.*, 77 (1999) 915.

[2] K. Kneipp, H. Kneipp, I. Itzkan, et al., *Chem. Rev.*, 99 (1999) 2957.

[3] K. Kneipp, H. Kneipp, I. Itzkan, et al., *J. Phys.-Condens. Matter*, 14 (2002) R597.

[4] D. Cialla, S. Pollok, C. Steinbrücker, et al., *Nanophotonics*, 3 (2013) 1.

[5] C.L. Haynes, A.D. McFarland, R.P. Van Duyne, *Anal. Chem.*, 77 (2005) 338A.

[6] Z.Q. Tian, B.Ren, D.Y. Wu, *J. Phys. Chem. B*, 106 (2002) 9463.

[7] A. Campion, P. Kambhampati, *Chem. Soc. Rev.*, 27 (1998) 241.

[8] S.J. Lee, Z. Guan, H. Xu, et al., *J. Phys. Chem. C*, 111 (2007) 17985.

[9] J.R. Lombardi, R.L. Birke, *J. Phys. Chem. C*, 112 (2008) 5605.

[10] D.Y. Wu, J.F. Li, B. Ren, et al., *Chem. Soc. Rev.*, 37 (2008) 1025.

[11] Y. Wang, B. Yan, L. Chen, *Chem. Rev.*, 113 (2013) 1391.

[12] W.E. Doering, S.M. Nie, *J. Phys. Chem. B*, 106 (2002) 311.

[13] P. Kambhampati, C.M. Child, M.C. Foster, et al., *J. Chem. Phys.*, 108 (1998) 5013.

[14] S.M. Morton, L. Jensen, *J.Am. Chem. Soc.*, 131 (2009) 4090.

[15] W.H. Park, Z.H. Kim, *Nano Lett.*, 10 (2010) 4040.

[16] N. Valley, N. Greeneltch, R.P. Van Duyne, *J. Phys. Chem. Lett.*, 4 (2013) 2599.

[17] K. Kneipp, Y. Wang, H. Kneipp, et al., *Phys. Rev. Lett.*, 78 (1997) 1667.

[18] K. Faulds, R.E. Littleford, D. Graham, et al., *Anal. Chem.*, 76 (2004) 592.

[19] C.G. Blatchford, J.R. Campbell, J.A. Creighton, *Surf. Sci.*, 120 (1982) 435.

[20] A.M. Schwartzberg, C.D. Grant, A. Wolcott, et al., *J. Phys. Chem. B*, 108 (2004) 19191.

[21] R.G. Freeman, K.C. Grabar, K.J. Allison, et al., *Science*, 267 (1995) 1629.

[22] D.J. Maxwell, S.R. Emory, S.M. Nie, *Chem. Mater.*, 13 (2001) 1082.

[23] C.L. Haynes, R.P. Van Duyne, *J. Phys. Chem. B*, 107 (2003) 7426.

[24] D.M. Kuncicky, S.D. Christesen, O.D. Velev, *Appl. Spectrosc.*, 59 (2005) 401.

[25] L.H. Lu, A. Eychmüller, A. Kobayashi, et al., *Langmuir*, 22 (2006) 2605.

[26] S. Chang, Z.A. Combs, M.K. Gupta, et al., *ACS Appl. Mater. Interfaces*, 2 (2010) 3333.

[27] R. Kodiyath, T.A. Papadopoulos, J. Wang, et al., *J. Phys. Chem. C*, 116 (2012) 13917.

[28] L.M. Bronstein, 'Nanoparticles made in mesoporous solids' in *Colloid Chemistry 1*, Springer-Verlag: Berlin, Vol. 226 (2003) pp. 55–89.

[29] B. Lee, H.G. Zhu, Z.T. Zhang, et al., *Micropor. Mesopor. Mater.*, 70 (2004) 71.

[30] C. Aprile, A. Abad, G.A. Hermenegildo, et al., *J. Mater. Chem.*, 15 (2005) 4408.

[31] Z. Konya, V.F. Puntes, I. Kiricsi, et al., *Chem. Mater.*, 15 (2003) 1242.

[32] M.H. Huang, A. Choudrey, P.D. Yang, *Chem. Comm.*, (2000) 1063.

[33] Y. Guari, C. Thieuleux, A. Mehdi, et al., *Chem. Comm.*, (2001) 1374.

[34] J.H. Park, J.K. Park, H.Y. Shin, *Mater. Lett.*, 61 (2007) 156.

[35] A. Ghosh, C.R. Patra, P. Mukherjee, et al., *Micropor. Mesopor. Mater.*, 58 (2003) 201.

[36] C.M. Yang, P.H. Liu, Y.F. Ho, et al., *Chem. Mater.*, 15 (2003) 275.

[37] Y.J. Han, J.M. Kim, G.D. Stucky, *Chem. Mater.*, 12 (2000) 2068.

[38] S. Besson, Thesis: 'Films organisés de silice mésoporeuse : synthèse, caractérisation structurale et utilisation pour la croissance de nanoparticules', Ecole polytechnique Palaiseau, 2002.

[39] Y. Plyuto, J.M. Berquier, C. Jacquiod, et al., *Chem. Commun.*, (1999) 1653.

[40] (a) W.P. Cai, L.D. Zhang*, J. Phys.-Condens. Matter*, 9 (1997) 7257. (b) W.P. Cai, L.D. Zhang, H.C. Zhong, et al.*, J. Mater. Res.*, 13 (1998) 2888.

[41] L.Z. Wang, J.L. Shi, W.H. Zhang, et al., *Chem. Mater.*, 11 (1999) 3015.

[42] W. Chen, J.Y. Zhang, W.P. Cai, *Scr. Mater.*, 48 (2003) 1061.

[43] W. Chen, W.P. Cai, C.H. Liang, et al., *Mater. Res. Bull.*, 36 (2001) 335.

[44] V. Hornebecq, M. Antonietti, T. Cardinal, et al., *Chem. Mater.*, 15 (2003) 1993.

[45] S. Eustis, G. Krylova, N. Smirnova, et al., *J. Photochem. Photobiol. A-Chem.*, 181 (2006) 385.

[46] G. Krylova, A. Eremenko, N. Smirnova, et al., *Int. J. Photoenergy*, 7 (2005) 193.

[47] H. Yazid, R. Adnan, S.A. Hamid, et al., *Turk. J. Chem.*, 34 (2010) 639.

[48] F. Moreau, G.C. Bond, A.O. Taylor, *J. Catal.*, 231 (2005) 105.

[49] D. Bergé-Lefranc, Thesis : 'Élimination de toxines urémiques par adsorption sur des matériaux zéolitiques', Aix-Marseille Université, 2006.

[50] (a) J. Lyklema, *Fundamentals of Interface and Colloid Science*, Academic Press: San Diego, Vol. 2 (1995) Chap. 2, pp. 1–91. (b) G.D. Parfitt, C.H. Rochester, *Adsorption from solution at the solid/liquid interface*, Academic Press: London, (1983).

[51] C.H. Giles, D. Smith, A. Huitson, *J. Colloid. Interface Sci.*, 47 (1974) 755.

[52] P.T. Dawson, G.T. Rich, D.A. Haydon, *J. Phys. Chem.*, 68 (1964) 3550.

[53] C. Hinz, *Geoderma*, 99 (2001) 225.

[54] E. Abbe, *Arch. F. Microsc. Anat.*, 9 (1873) 413.

[55] L. Rayleigh, 'Investigations in optics, with special reference to the spectroscope' in *The London, Edinburgh and Dublin Philosophical Magazine and Journal of Science*, Taylor and Francis: New York, Vol. 8 (1879) 261–274.

[56] R. Aroca, *Surface-Enhanced Vibrational Spectroscopy*, John Wiley & Sons: Chichester, (2007).

[57] J.R. Lombardi, R.L. Birke, T.H. Lu, et al., *J. Chem. Phys.*, 84 (1986) 4174.

[58] K.S.W. Sing, *Colloids Surf. A Physicochem. Eng. Asp.*, 187 (2001) 3.

[59] P.I. Ravikovitch, A.V. Neimark, *Langmuir*,18 (2002) 9830.

[60] F. Rouquerol, J. Rouquerol, K.S.W. Sing, *Adsorption by Powders and Porous Solids: Principles, Methodology and Applications*, First Ed. Academic Press: London, (1999).

[61] E. Bloch, P.L. Llewellyn, D. Vincent, et al., *J. Phys. Chem.* C, 114 (2010) 22652.

[62] P.V. Messina, P.C. Schulz, *J. Colloid. Interface Sci.*, 299 (2006) 305.

[63] J.H. Huang, K.L. Huang, S.Q. Liu, et al., *Colloids Surf.*, 330 (2008) 55.

[64] J.L. Solomon, R.J. Madix, J. Stöhr, *Surf. Sci.*, 255 (1991) 12.

[65] T.M. Herne, A.M. Ahern, R.L. Garrell, *J. Am. Chem. Soc.*, 113 (1991) 846.

[66] F.L. Arbeloa, I.L. Gonzalez, P.R. Ojeda, et al., *J. Chem. Soc., Faraday Trans. 2*, 78 (1982) 989.

[67] (a) V.M. Martínez, F.L. Arbeloa, J.B. Prieto, et al., *J. Phys. Chem. B*, 108 (2004) 20030. (b) V.M. Martínez, F.L. Arbeloa, J.B. Prieto, *J. Phys. Chem. B*, 109 (2005) 7443.

[68] J. Bujdák, N. Lyi, *J. Phys. Chem. B*, 109 (2005) 4608.

[69] T. Kikteva, D. Star, Z.H. Zhao, et al., *J. Phys. Chem. B*, 103 (1999) 1124.

[70] (a) M.A. Noginov, M. Vondrova, S.M. Williams, et al., *J. Opt. A: Pure Appl. Opt.*, 7 (2005) S219. (b) J. Zhao, L. Jensen, J. Sung, et al., *J. Am. Chem. Soc.*, 129 (2007) 7647.

[71] G.S.S. Saini, S. Kaur, S.K. Tripathi, et al., *Spectrochim. Acta, Part A*, 61 (2005) 653.

[72] (a) C.A. Murray, T.J. Greytak, *J. Chem. Phys.*, 71 (1979) 3355. (b) Y. Borodko, J.W. III Ager, G.E. Marti, et al., *J. Phys. Chem. B*, 109 (2005) 17386.

[73] J.R. Lombardi, R.L.J. Birke, *Chem. Phys.*, 136 (2012) 144704.

[74] E. Bloch, P.L. Llewellyn, T. Phan, et al., *Chem. Mater.,* 21 (2009) 48.

[75] T.A. El-Brolossy, T. Abdallah, M.B. Mohamed, *Eur. Phys. J. Special Topics*, 153 (2008) 361.

[76] (a) A. Merlen, V. Chevallier, J.C. Valmalette, et al., *Surf. Sci.*, 605 (2011) 1214. (b) A. Merlen, F. Lagugné-Labarthet, E. Harté, *J. Phys. Chem. C*, 114 (2010) 12878.

Chapter 3

Nanocomposites for the storage of hydrogen

Table of contents

Chapter 3: Nanocomposites for the storage of hydrogen

III.1. Context and scientific approach

In addition to the considerable pollution arising from industrialization, the energetic dependency on fossil fuels (coal, oil and gas) poses two major concerns: the coming shortage of these finite energy resources and the greenhouse effect (global warming) due to the emission of environmentally harmful gases such as carbon dioxide. In order to face these problems, a growing interest is devoted to new energy resources compatible with the so-called 'green energy' or 'clean energy'.

In the field of energy storage and conversion, besides the development of the well-known renewable energies (solar energy, wind energy, hydropower, geothermal energy and biomass), one of the main challenges is focused on hydrogen. Indeed, being abundant and non-polluting, the latter appears as an attractive and promising environmentally friendly energy 'vector' for potential sustainable alternative energy. As mentioned, it is worth noting that this is not an energy resource but an energy carrier: its generation and storage are two necessary steps towards the production of energy. Nowadays, hydrogen can be easily produced by different means such as water electrolysis, hydrogen rich hydrocarbons reforming and biomass gasification. [1] Furthermore, different approaches are available for storing hydrogen: the high compression or cryogenic liquefaction in tanks. Though both techniques possess advantageous characteristics for stationary hydrogen applications, none of them satisfies all of requirements for viable mobile technologies. Not to mention the cost processing, some scientific and technological issues still need to be overcome for achievement in transportation and utility applications. More precisely, there are constraints concerning an appreciable energetic yield in terms of production and efficient and stable storage into a desirable store system at room temperature and atmospheric pressure: i.e. high gravimetric and volumetric storage capacities, reasonable temperature and pressure conditions, fast refueling capability, no fuel leakage, compact and light reservoir, etc. Besides, safety concerns may also be taken into account since hydrogen is highly flammable and explosive. Efficient delivery capacities (good releasing rate and reasonable temperature and pressure conditions) are also of prime interest. Therefore, many efforts have been made in order to propose other viable alternatives for hydrogen storage with respect to efficiency, stability and safety. Two solid-state storage approaches based on reversible hydrogen uptake-and-release mechanisms have been developed: the storage of hydrogen through **a<u>b</u>sorption** into solid metallic sorbents and the storage of hydrogen through **a<u>d</u>sorption** on porous materials with high surface area. [1–5]

In the first solid-state storage approach, hydrogen trapping occurs via adsorption (physisorption and chemisorption successively) then subsequent diffusion into the lattice structure of the solid sorbent upon increasing pressure at a constant temperature in a metal or alloy (whilst the overall process is exothermic). At the early stage, next to the adsorption step, the hydrogen enters the lattice then occupies the interstitial sites of the sorbent inducing the formation of a 'solid solution of hydrogen' named α-phase with concomitant volume expansion of the structure. On increasing the interstitially dissolved hydrogen content in the α-phase a new phase called β-phase starts to be formed above a saturation content (maximum hydrogen solubility in the α-phase), leading to the coexistence of both phases. On further hydrogen loading in the lattice at constant equilibrium pressure (specific to each material), the β-phase increases at the expense of the α-phase up to obtaining only the β-phase called 'hydride'. At this final stage, in order to increase the amount of hydrogen, pressure has to be increased again above the equilibrium pressure. The release of hydrogen is obtained by sufficient heating supply although it is not systematically fully reversible: after releasing process, the sorbent returns to its initial state but stays as a hydride (obviously with smaller hydrogen content). With pressure and temperature change, uptake-and-release cycles can be performed. Different types of metal hydrides or complex metal hydrides have been developed [6–11]. Although these materials have low gravimetric energy capacity (due to their high weight), they exhibit good volumetric energy capacity. To date, the storage technology arising from hydride is the only to be currently commercially available: for instance, AB_5–type metal hydrides (e.g. $LaNi_5$, $MmNi_5$ – Mm refers to mischmetal which is a mixture of rare earth elements) [12–13], AB_2–type metal hydrides (e.g. MgH_2) [14], AB–type metal hydrides (e.g. TiFe) [13] and alanate (e.g. $NaAlH_4$, $LiAlH_4$) and borohydride (e.g. $NaBH_4$, $LiBH_4$) complex metal hydrides.

In the second solid-state storage approach, hydrogen trapping occurs via adsorption on the accessible porous surface of the sorbents, upon increasing pressure and at a constant temperature. Hence, the surface area of porous materials plays a very important role in the adsorption capacity. Moreover, contrary to the previous absorption approach, there is no diffusion limitation; then no activation is required in the adsorption process. This may lead to a phenomenon occurring with faster kinetics. Besides, the process is fully reversible. A wide range of porous solids including e.g. carbon-based materials [15] (i.e. activated carbon ACs, carbon nanotubes CNTs, graphitic nanofibers GNFs, etc.), silica-based materials [16] (i.e. silica, zeolites, titanosilicates, etc.), metal organic-frameworks (MOFs) [17], porous covalent organic frameworks [18] have been widely studied for adsorption of hydrogen over the past decades. However, although these materials are light as compared to the sorbents used in metal hydride storage approach and possess high surface area due to their porosity that confers to them the possibility of trapping high amount of hydrogen, the hydrogen storage through adsorption

approach has been shown to be more effective at low temperatures owing to the weak interaction forces (van der Waals) dominating the process. This does not coincide with the US Department of Energy (DOE) storage targets for mobile applications that recommend ambient temperature (233 to 358 K). Besides, the hydrogen gravimetric capacity goal for 2015 is of 5.5 wt% taking into account the mass and volume of the overall system (material, tank, valves, regulators, etc.) which assume a higher capacity for the sorbent materials of about 6.45 wt% (considering 10 % extra-weight for the tank and other parts). Hydrogen uptake of not more than 2 wt% is generally obtained for zeolites at 77 K and less than 0.1 wt% at room temperature. MOF-177 ($4750\ m^2.g^{-1}$) reached an amount of 7.5 wt% of hydrogen adsorbed [18]. Hydrogen has been loaded up to 9 wt% in the MOF NU-100 ($5800\ m^2.g^{-1}$) at 77 K [19]. COF-102 ($3620\ m^2.g^{-1}$) has been shown to store 7.2 wt% [18]. Activated carbon has been found to store 6.8 wt% at 77 K [20]. The temperature dependence of the hydrogen uptake, the limit in adsorbed amounts and the possibility to have a controlled release of hydrogen are nowadays the major key issues for hydrogen storage via adsorption.

Porous materials seem to be good candidates for hydrogen storage applications but as mentioned before high surface area and light weight are not sufficient properties. To enable high loading at room temperature, the energies of interactions (heats of adsorption) of hydrogen with the sorbent surface during adsorption should increase to 15– 25 $kJ.mol^{-1}$ [21]. Functionalization of the porous matrices via introduction of metal species could significantly enhance the surface reactivity and may allow overcoming this issue. Indeed, as develop earlier, metal have specific behavior with hydrogen. It is believed that splitting of hydrogen occurs at the surface of the metal catalyst, and then hydrogen atoms migrate towards the sorbent surface, this phenomenon is known as *spillover effect*. [22] Therefore, combining both properties of high heats of adsorption and high surface areas into a nanocomposite could be suggested as one of the prospective methods for better storage in porous materials and especially reach high hydrogen storage at room temperature. Noble and transition metal such as for instance palladium, rhodium and nickel are known for their affinity for hydrogen. It has appeared interesting to use such kind of metal for functionalizing the porous sorbents towards improved hydrogen storage. Thus, metal modified-porous materials have been studied to explore their hydrogen storage performances over the last years. [23] The results of these studies show the positive effect of incorporating metals on the hydrogen adsorption capacity as compared to the pristine sorbents. However, the hydrogen storage capacity is still far from the goal for mobile applications and additional efforts to understand the mechanism of adsorption in these modified structures and to optimize their properties are necessary.

In this context, this work was focused on the preparation of micro-/mesoporous materials, including silica and carbon, functionalized with metal nanoparticles as nanocomposites for the storage of hydrogen. Nickel material, presenting required heat of adsorption towards hydrogen [21], will be the metal of interest in this study. In literature, different synthesis approaches have been used to synthesize nickel/porous (silica or carbon) matrix nanocomposites: i.e. either in one step via the so-called one-pot synthesis in which nickel precursor is directly introduced to the reaction mixture [24–26], or in two steps whose first step is an impregnation process of the host matrix (previously synthesized) with nickel salt [26–30]. In both cases, reduction in situ of the nickel in the presence of appropriate reducing agent leads to formation of the nanoparticles which are either embedded in the matrix walls or present at the porous surface according to the synthesis approach employed. Two experimental approaches have been developed in order to reduce in situ the nickel salts: chemical reduction in gas phase with H_2, N_2 or light hydrocarbons [24–26,31] and/or liquid phase using sodium borohydride $NaBH_4$ or hydrazine hydrate ($N_2H_4 \cdot H_2O$) [26–30]. In this study, prior to synthesize the nanocomposite, an important phase of setting-up a procedure to obtained unconfined nickel particles via two reduction routes, in liquid (N_2H_4) and gas phase (H_2), was made. Then these reduction procedures were used to induce the growth of nickel nanoparticles in the porosity of the host materials. And finally, the hydrogen properties of nickel-based bulk materials and confined particles in nanocomposites, i.e. Ni@Silica and Ni@Carbon, were studied at low temperature (77 K).

III.2. Incorporation of nickel nanoparticles in mesoporous matrices

III.2.1. Preliminary study: Setting up of reduction methods of unconfined nickel precursors

Metal nanoparticles of nickel are relatively difficult to synthesize because they easily get oxidized. A preliminary study was made in order to set up procedures to synthesize unconfined nickel particles, according to the literature: by means of chemical reduction of the nickel source either in gas phase (H_2) or in liquid phase (N_2H_4).

III.2.1.a. Nickel precursors

Commercial nickel acetate tetrahydrate, $Ni(CH_3CO_2)_2 \cdot 4H_2O$, which is a crystalline powder that possesses a bright green color, is commonly used as a nickel source. Its XRD pattern is presented in **Figure 3.1 (a)** and can be indexed using the JCPDS card N°26–1282. This nickel source was used during this work because two nickel precursors could be brought out from its thermogravimetric profile, **Figure 3.1 (b)**. Indeed, two main weight loss stages could be observed

during the thermal analysis. The first one, between 60 and 170°C, can be attributed to dehydration of uncrystallized and crystallized water in the initial nickel source [32–34] and to evolution of acetic acid in the gas phase: basic nickel acetate in the solid phase, $(1-x)Ni(CH_3CO_2)_2 \cdot xNi(OH)_2$, is thus generated [34]. The second one, between 260 and 350°C, corresponds to the decomposition of the intermediate anhydrous nickel acetate into nickel oxide [34–36]. The two nickel precursors studied were obtained after thermal treatments of nickel acetate during 4 h in static air atmosphere. The treatment temperatures were selected on the plateaus appearing after the different weight losses. Therefore, the first precursor was obtained after a treatment at 200°C, while the second one after a treatment at 400°C. The calcination products are denoted as NiAc (standing for nickel acetate) followed by the calcination temperature T in parenthesis, i.e. NiAc(T). Thus, the nickel precursors obtained after calcinations of nickel acetate are NiAc(200°C) and NiAc(400°C), respectively.

The two nickel precursors were characterized using X-ray diffraction analysis, **Figure 3.1 (b insets)**. The sample of commercial nickel acetate treated at 200°C, NiAc(200°C), had a brighter green color than the crystalline commercial one; no diffraction lines could be observed on its XRD profile. This allows concluding that amorphous anhydrous intermediate nickel acetate was obtained. The XRD pattern of the commercial nickel acetate treated at 400°C, NiAc(400°C), showed two well defined diffraction peaks; these lines can be indexed using the JCPDS card N°44–1159 corresponding to rhombohedral nickel oxide and are assigned to the (101) and (012) reflections. The sample had a black color which is characteristic of nickel oxide nanoparticles.

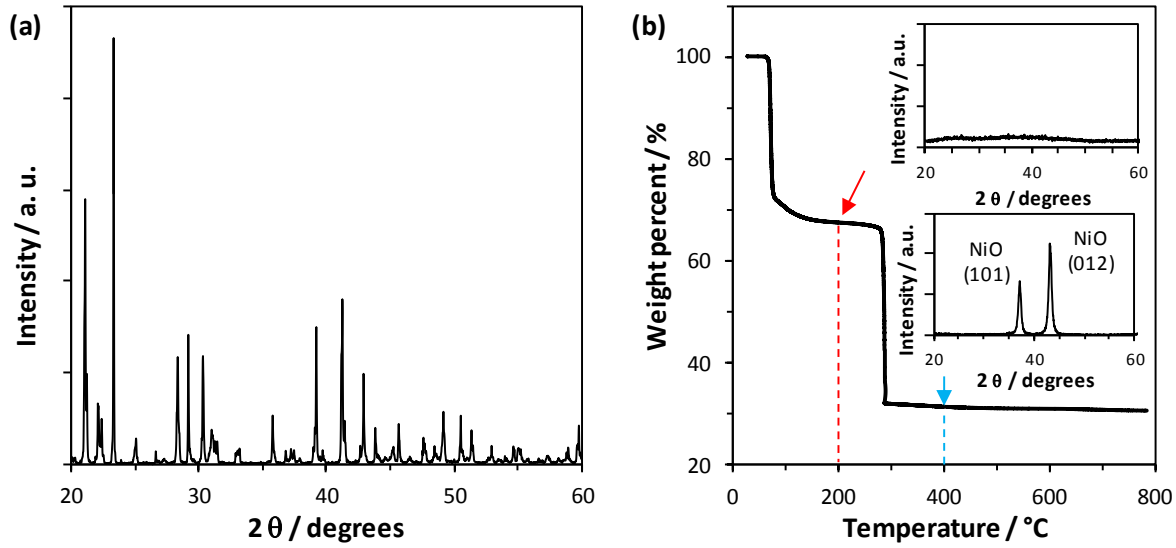

Figure 3.1: Wide-angle XRD pattern (a) and TGA profile (b) of commercial nickel acetate tetrahydrate. Wide-angle XRD patterns of NiAc(200°C) and NiAc(400°C) (b insets).

After the preparation of the nickel precursors, NiAc(200°C) and NiAc(400°C), two types of treatments were performed in order to synthesize unconfined nickel particles: reduction in gas phase using hydrogen as reducing agent and reduction in liquid phase using hydrazine as reducing agent. Powder of commercial nickel oxide nanoparticles was reduced similarly in order to have a comparison. Powder of commercial nickel nanoparticles was used as a reference material within this study.

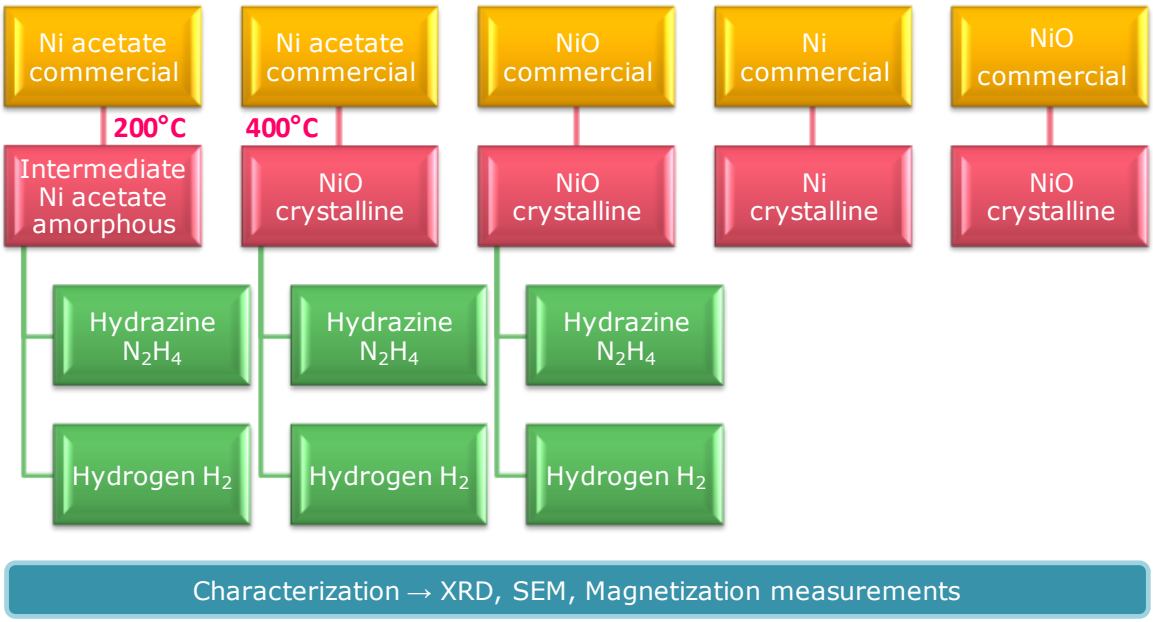

Figure 3.2: Diagram of the scientific approach of the preliminary study.

Afterwards, the different samples were characterized using various techniques such as XRD, SEM and magnetization measurements. The scientific approach of the preliminary study is exemplified in **Figure 3.2**.

III.2.1.b. Chemical reduction in liquid phase

The chemical reduction in liquid phase of the nickel precursors, inspired from literature [30,37], was performed in a basic hydrazine excess. The solid samples were heated to 80°C for 0.5 h. Then, 64 % hydrazine and a 20 M sodium hydroxide solution were added in excess, the pH of the solution was evaluated to be 14. The starting material ratio was set to 200 mg : 5 mL : 5 mL [NiAc(T) : N_2H_4 : NaOH]. The mixture was left to react for 3 h at 80°C in a thermostatic oil bath. The green color of NiAc(200°C), changed to black upon insertion of the liquids and the mixture with an initial violet-blue color changed to white milky after some minutes. The violet-blue color can be ascribed to the formation of stable nickel-hydrazine species in solution. Indeed, it is known that unsupported Ni^{2+} ions form a blue complex $[Ni(N_2H_4)_3]^{2+}$ in basic hydrazine media [29(b)]. This complex is formed via the substitution of water ligands by hydrazine ligands.

Also for our sample, we believe that a stable supported $[Ni(N_2H_4)_n]^{2+}$ complex was intermediately formed in solution before being decomposed. Upon insertion of the liquids, the mixture color was black grayish for NiAc(400°C) and green khaki then turned to black greyish for commercial nickel oxide. The obtained solids were filtered, washed then dried at 80°C. The different samples obtained are denoted as NiAc(T)– N_2H_4 and NiO– N_2H_4, respectively. The samples NiAc(200°C)– N_2H_4 and NiO– N_2H_4 were black and NiAc(400°C)– N_2H_4 sample was black grayish. All samples were magnetic: the particles were attracted to a magnet.

III.2.1.c. Chemical reduction in gas phase

The chemical reduction in gas phase, inspired from literature [38], of the nickel precursors was carried out in a built-in-house apparatus. Prior to reduction process, the samples were degassed at room temperature then purged with an argon/hydrogen (95/5 molar ratio) gas mixture to ensure purity of the atmosphere in the reduction system. Finally, the samples were treated at 350°C under the Ar/H_2 mixture used for the purge during 16 h with a heating rate of $2°C.min^{-1}$. The different samples obtained are denoted as NiO– H_2 and NiAc(T)– H_2, respectively. NiAc(200°C)– H_2 sample was black grayish, NiAc(400°C)– H_2 and NiO– H_2 samples were black. All samples were magnetic: the particles were attracted to a magnet.

III.2.1.d. Characterization of unconfined particles synthesized

Prior to present the different synthesized samples, the characterization of the reference commercial powders of nickel and nickel oxide will be introduced. The two powders were characterized using nitrogen adsorption/desorption measurements at 77 K, TEM and XRD.

After nitrogen adsorption/desorption measurements, the specific surface areas (S_{BET}) estimated using BET method are 75 m^2g^{-1} and 5 m^2g^{-1} for NiO and Ni powders, respectively. The average particle sizes were calculated using the classical formula $S_{BET} = \frac{6}{\rho \times D}$ where ρ is the density and D is the size of isotropic particle (**Table 3.1**). [39] Results obtained are in agreement with the characteristics specified by Aldrich, i.e. $D < 50$ nm and $D < 150$ nm for NiO and Ni powders, respectively.

Table 3.1: Specific surface area and particle size of NiO and Ni powders derived from nitrogen adsorption/desorption measurements.

Sample	S_{BET} [a] /m^2g^{-1}	ρ /g cm^{-3}	D [b] /nm
NiO	75	6.67	12
Ni	5	8.90	135

a S_{BET}: BET surface area
b D: Particle size determined using the specific surface area

TEM images obtained for NiO and Ni powders are presented in **Figure 3.3**. In the case of NiO, the powder presents an important polydispersity with particles size varying from 5 to 25 nm (**Figure 3.3 (a)**). Furthermore, the nanoparticles geometry varies significantly, some particles are quite spherical whereas some others present angular shape. On **Figure 3.3 (b)**, it can be seen that the nanoparticles are well crystallized. Concerning the Ni powder, an important polydispersity in nanoparticle size is also observed: the crystallite size varies from 20 to 150 nm, as shown in **Figure 3.3 (c–d)**.

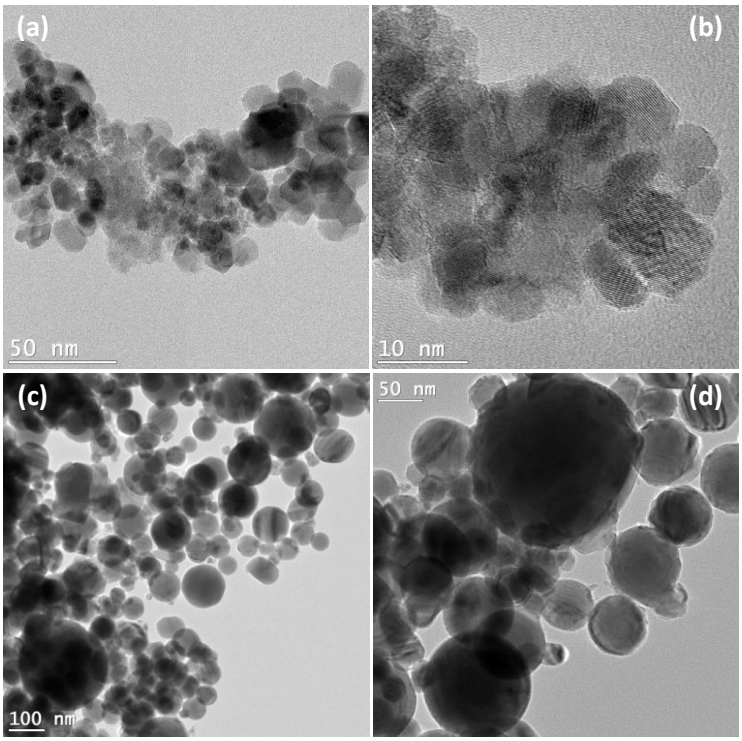

Figure 3.3: TEM images of NiO (a–b) and Ni (c–d) commercial nanopowders.

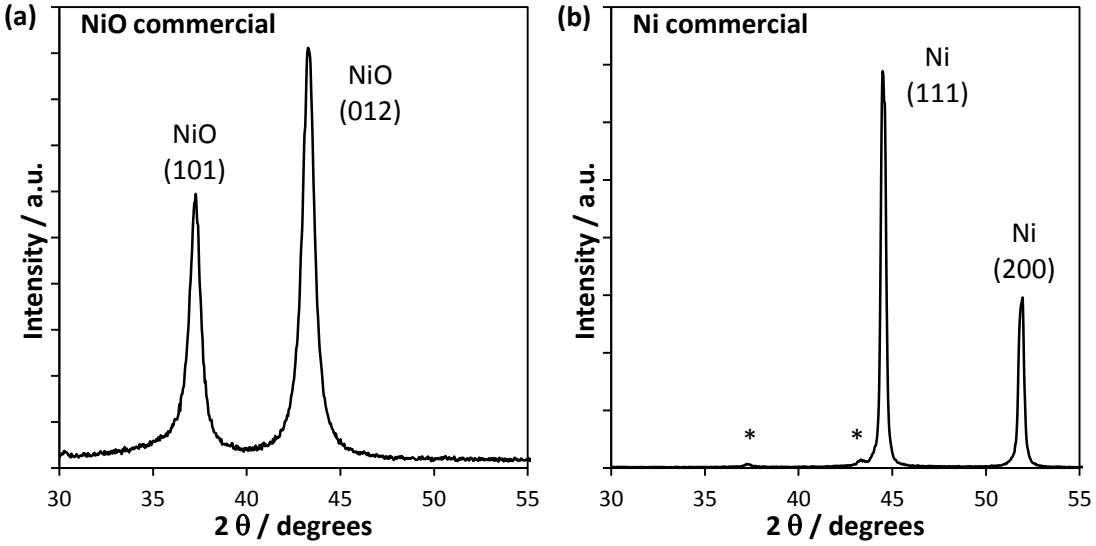

Figure 3.4: X-ray diffraction patterns obtained for NiO (a) and Ni (b) commercial nanopowders.

These powders were then characterized using X-ray diffraction. As it can be seen on **Figure 3.4**, well-defined diffraction peaks are obtained. From the XRD patterns of both NiO and Ni nanoparticles, a larger broadening (or Full Width at Half Maximum – FWHM) of the diffraction peaks obtained for NiO powder is obtained as compared to the one for Ni powder. This is in good agreement with the difference of nanoparticle size mentioned above [39]; this difference is also observed on the TEM images of NiO and Ni presented in **Figure 3.3**. The diffraction peaks of NiO powder are indexed using the JCPDS cards N°44-1159 corresponding to rhombohedral nickel oxide. In the case of Ni nanopowder, the most intense peaks were indexed using the JCPDS card N°65-2865 corresponding to cubic nickel. In the pattern of Ni powder, two supplementary peaks (with very low intensity, shown with stars) are present, they can be indexed with the (111) and (200) reflections of NiO. This means that the surface of Ni nanopowder is partially oxidized.

In order to evaluate the efficiency of the chemical reductions in liquid and gas phase of the two types of nickel precursors pre-treated at 200°C and 400°C, the different powders obtained were characterized using XRD, SEM and magnetization measurements.

X-ray diffraction analysis

Particles obtained via reduction in liquid phase

After the reduction treatment, the particles issued from NiAc(200°C) were purely composed of Ni in cubic phase (100 wt%; diffraction lines indexed with JCPDS card N°62-2865), as shown on **Figure 3.5**.

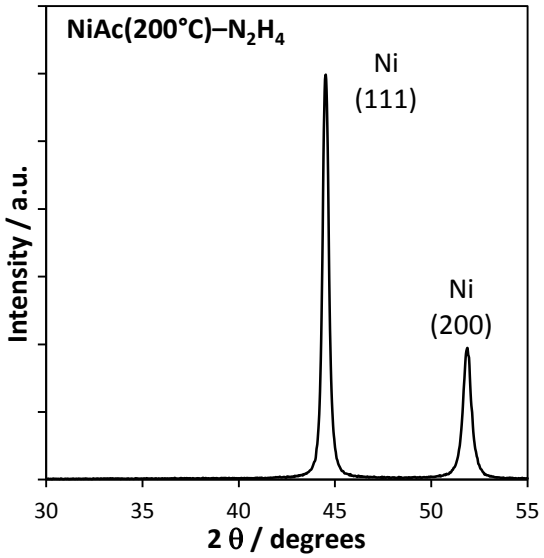

Figure 3.5: X-ray diffraction pattern obtained for NiAc(200°C)– N_2H_4.

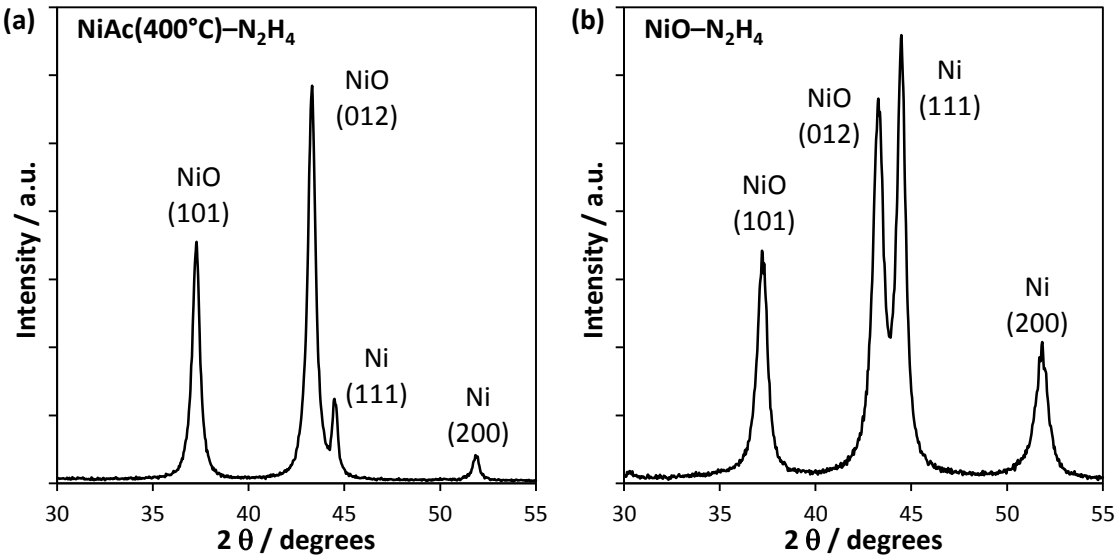

Figure 3.6: X-ray diffraction patterns obtained for NiAc(400°C)– N_2H_4 (a) and NiO– N_2H_4 (b).

Contrarily, for the particles issued from NiAc(400°C) and NiO, a mixture of Ni in cubic phase and NiO in rhombohedral phase[1] (JCPDS card N°44-1159) was obtained, **Figure 3.6**. A calibration curve, presented in **Figure 3.7**, was used in order to estimate percentages in weight of Ni cubic and NiO rhombohedral in the unconfined particles synthesized. The samples used to plot this calibration curve were the commercial powders of Ni cubic and NiO rhombohedral nanoparticles.

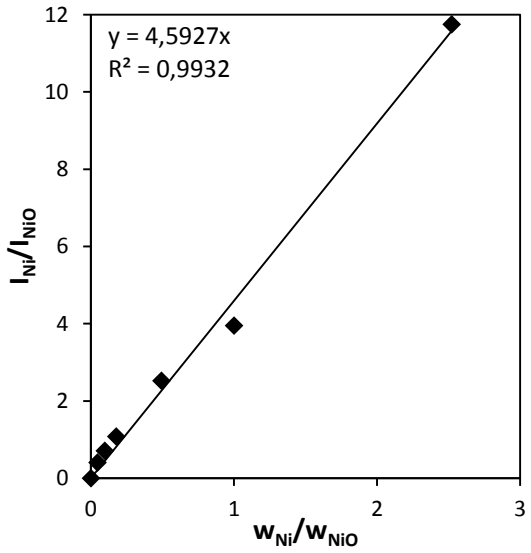

Figure 3.7: Calibration curve of the ratio of Ni and NiO intensities in function of their corresponding weight ratio in samples examined with XRD.

[1] In the rest of the study, Ni in cubic phase and NiO in rhombohedral phase will be denoted as Ni cubic and NiO rhombohedral, respectively.

The derived weight percents are listed in **Table 3.2**. The composition of NiAc(400°C)– N_2H_4 particles was about 4.5 wt% of Ni cubic and 95.5 wt% of NiO rhombohedral, **Figure 3.6 (a)**. For the commercial nickel oxide treated, the composition of the particles was of Ni cubic (20 wt%) and NiO rhombohedral (80 wt%), **Figure 3.6 (b)**. The compositions of the samples were in good agreement with the phase amounts calculated with the Semi-Quantitative (S-Q) analysis tool of the XRD software.

Table 3.2: Composition of the different samples issued from reduction in liquid phase derived from the calibration curve and measured from the Semi-Quantitative analysis tool of XRD software.

Sample	Calibration curve		S-Q analysis tool of XRD	
	Ni cubic /wt%	NiO rhombo /wt%	Ni cubic /wt%	NiO rhombo /wt%
NiAc(200°C)– N_2H_4	100	0	100	0
NiAc(400°C)– N_2H_4	4.5	95.5	4.8	95.2
NiO– N_2H_4	20	80	19.8	80.2

Reduction treatment using a volume ratio between 64 % N_2H_4 and 20 M NaOH solutions which was two times lower than previously (i.e. 2.5 mL : 2.5 mL) was performed on NiAc(200°C), NiAc(400°C). Despite the decrease in volume ratio, this reduction procedure seemed to be as efficient as the previous one. Indeed, the particles obtained from NiAc(200°C) were found to be composed solely of Ni cubic and those obtained from NiAc(400°C) were of quasi-identical composition as before, i.e. 4.2 wt% of Ni cubic and 95.8 wt% of NiO rhombohedral, respectively.

Particles obtained via reduction in gas phase

After the reduction treatment, the particles issued from commercial nickel oxide were composed of 20.4 wt% of Ni cubic and 79.6 wt% of NiO rhombohedral (**Figure 3.8 (a)**). For NiAc(400°C), the composition of the particles was also a mixture of Ni cubic (2.1 wt%) and NiO rhombohedral (97.9 wt%) (**Figure 3.8 (b)**).

Additionally to Ni cubic and NiO rhombohedral phases, Ni in hexagonal structure[2] (JCPDS card N°45-1027) was present in the particles issued from NiAc(200°C) (**Figure 3.9**). Due to the presence of Ni hexagonal in the composition of the samples issued from NiAc(200°C) precursor, phase amounts were not calculated using the calibration curve.

[2] In the rest of the study, Ni in hexagonal phase will be denoted as Ni hexagonal.

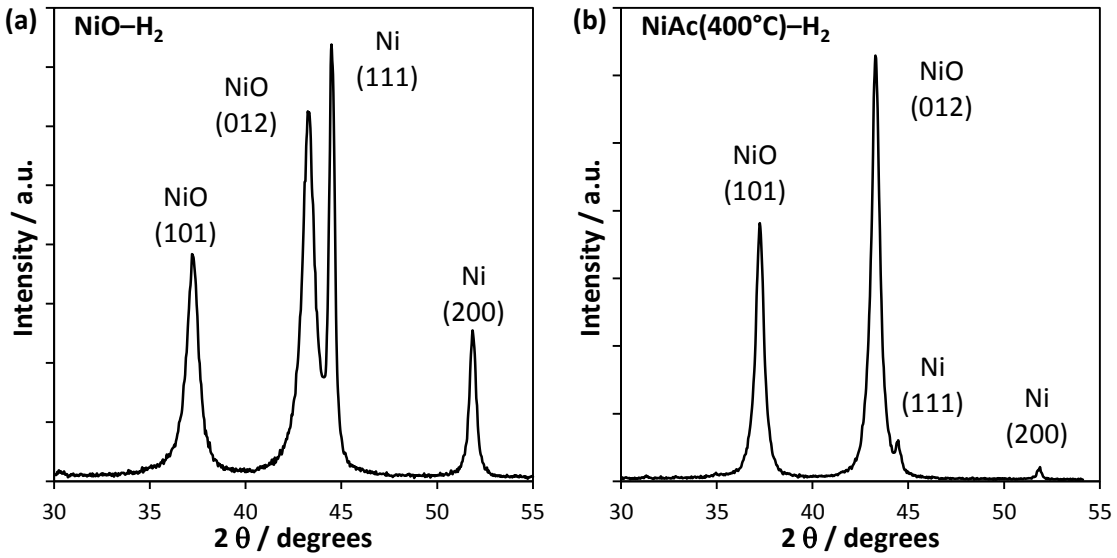

Figure 3.8: X-ray diffraction patterns obtained for NiO– H_2 (a) and NiAc(400°C)– H_2 (b).

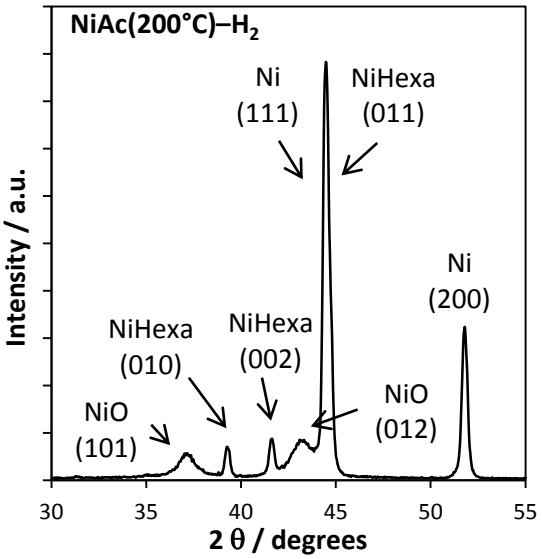

Figure 3.9: X-ray diffraction patterns obtained for NiAc(200°C)– H_2.

The compositions of the samples derived from the calibration curve are listed in **Table 3.3**. The compositions of the samples were in good agreement with the phase amounts calculated with the S-Q analysis tool of the XRD software. Besides, the amounts of Ni and NiO in the sample NiAc(200°C)– H_2 could be estimated at 52 wt% of Ni cubic, 24.9 wt% of Ni hexagonal and 23.1 wt% of NiO rhombohedral. One can notice that Ni hexagonal was not included in the composition neither of the other samples reduced in gas phase nor in the products issued from the reduction in liquid phase. This new phase seems to appear at the expense of NiO rhombohedral, thus increasing the yield of nickel in the particle composition of NiAc(200°C)– H_2.

Table 3.3: Composition of the different samples issued from reduction in gas phase derived from the calibration curve and measured from the Semi-Quantitative analysis tool of XRD software.

Sample	Calibration curve		S-Q analysis tool of XRD	
	Ni cubic /wt%	NiO rhombo /wt%	Ni cubic /wt%	NiO rhombo /wt%
NiAc(200°C)– H_2 [a]	---	---	52	23.1
NiAc(400°C)– H_2	2.1	97.9	2.1	97.9
NiO– H_2	20.4	79.6	21.8	78.2
a Not calculated with the calibration curve (due to the presence of Ni in hexagonal phase)				

Reduction treatment with a duration plateau at 350°C approximately three times lower than previously (i.e. 5 h) was performed on NiAc(200°C) and NiAc(400°C). The particles issued from NiAc(400°C)– H_2 – 5 h, were composed of Ni cubic and NiO rhombohedral as those obtained with the previous procedure and the weight percents were slightly higher: i.e. 6.6 wt% of Ni cubic and 93.4 wt% of NiO rhombohedral. For the particles issued from NiAc(200°C)– H_2 – 5 h, a mixture of Ni cubic, Ni hexagonal and NiO rhombohedral was obtained as previously, except that a part of intermediate amorphous nickel acetate was left suggesting that the reduction was not complete. This reduction procedure seemed to be equivalent the previous one if the precursor is NiAc(400°C), while it is not really the case if the precursor is NiAc(200°C).

Scanning Electron Microscopy

Selected unconfined samples issued from liquid and gas reductions were examined with SEM in order to evaluate their shape and size.

Particles obtained via reduction in liquid phase

We can observe that the particles are agglomerated and have a quasi-spherical shape. The particle size of NiAc(200°C)– N_2H_4 is homogeneous and is estimated around 450 nm and a little quantity of particles with size around 350 nm are also observed (**Figure 3.10 (a–b)**). A wider size polydispersity is observed for the sample NiAc(400°C)– N_2H_4 (**Figure 3.10 (c–d)**). Populations of particles with mean size around 350 nm and 135 nm are present. Much smaller (~50 nm) and much bigger (> 550 nm) particles can also be observed.

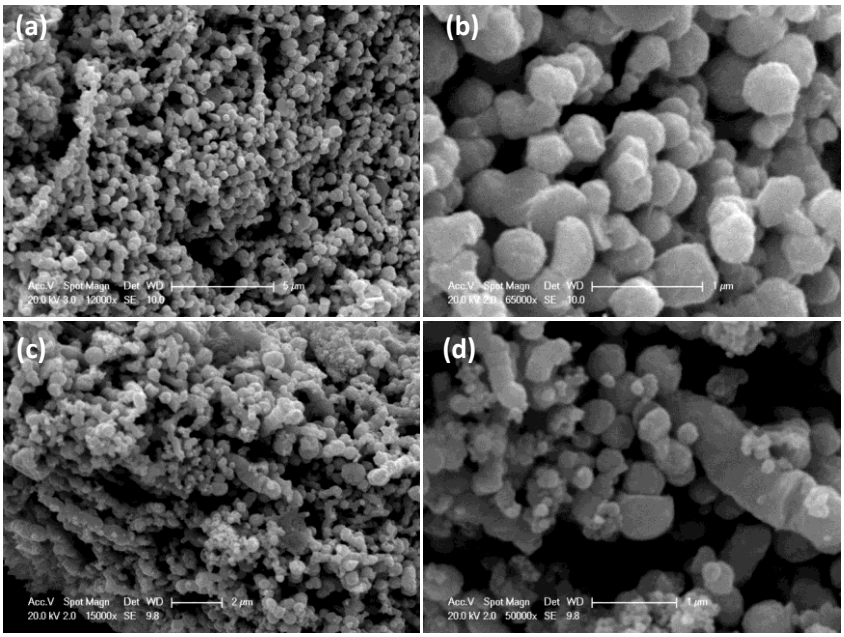

Figure 3.10: SEM images of NiAc(200°C)– N_2H_4 (a–b) and NiAc(400°C)– N_2H_4 (c–d).

Particles obtained via reduction in gas phase

As for the samples issued from reduction in liquid phase, SEM images of the samples NiAc(200°C)– H_2 and NiAc(400°C)– H_2show quasi-spherical agglomerated particles. The sample NiAc(200°C)– H_2 presents a quite homogeneous dispersion in size which is estimated at about 700 nm, and few particles with lower size (500 nm) are also present, **Figure 3.11 (a–b)**. While the particles of NiAc(400°C)– H_2 are much smaller with a mean size around 185 nm, and some particles of diameter around 100 nm are present, **Figure 3.11 (c–d)**.

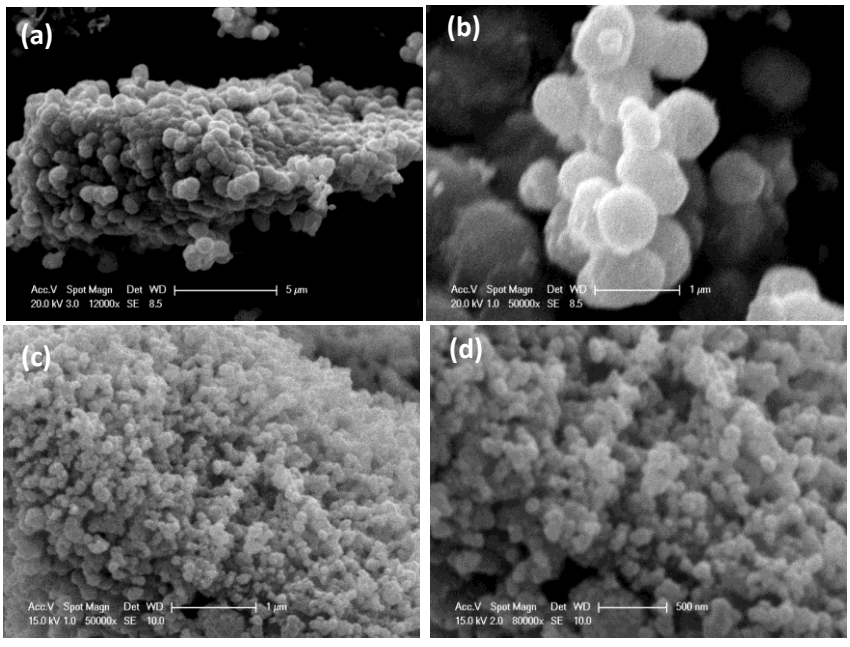

Figure 3.11: SEM images of NiAc(200°C)– H_2 (a–b) and NiAc(400°C)– H_2 (c–d).

Magnetic property measurements

Magnetic property measurements of selected samples were performed in order to evaluate the magnetic behavior of the particles synthesized. The experiments consist in the measurements of samples magnetization as a function of applied magnetic field (from 50 kOe to – 50 kOe) at room temperature (298 K). They were performed by Corine Reibel at Institut Charles Gerhardt, Montpellier, using a SQUID magnetometer (Quantum Design, MPMS-XL-7T model).

Particles obtained via reduction in liquid phase

Results obtained for NiAc(200°C)– N_2H_4 and NiAc(400°C)– N_2H_4 are presented in **Figure 3.12** and those obtained on commercial nickel particles are also given for comparison as a reference material. A photographic image of the samples attracted when approaching a magnet is presented in **Figure 3.12 (inset)**. For all samples, the evolution of the normalized magnetization (per gram of solid) as a function of applied magnetic field is plotted. As it can be observed, all curves have similar shape. This behavior is characteristic of ferromagnetic compound as shown in **Figure 3.13**.

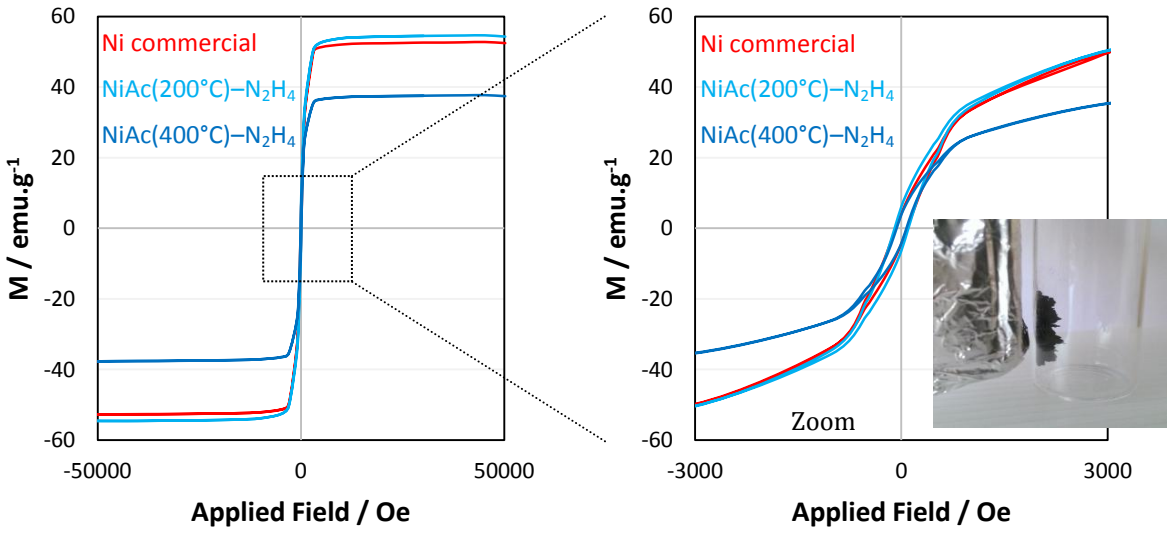

Figure 3.12: Normalized magnetization curves at 298 K of particles obtained via reduction in liquid phase of the two types of nickel precursors (left), zoom between – 3 and 3 kOe (right) and photographic image of samples showing good ferromagnetic properties (inset).

For an initially unmagnetized sample, i.e. $M \equiv 0$ at $H = 0$, as H increases from zero, M increases as shown by the dashed curves above in **Figure 3.13**. This magnetization process is due to the motion and growth of the magnetic domains. When the saturation point (***a***) is reached, the magnetization curve no longer retraces the original dashed curve when H is reduced (***a*** *to* ***b***). When the applied field H reaches again zero, the sample still retains some magnetization (***b***) due

to the existence of domains still aligned in the original direction of the applied field. The value at $H = 0$ is defined as the remanent magnetization or retentivity (M_r). In order to reduce the magnetization M to zero, a reverse field known as the coercive force or coercivity (H_c) is required. Soft and hard magnetic materials are distinguished by their small and large area of the hysteresis loop, respectively (**Figure 3.14**).

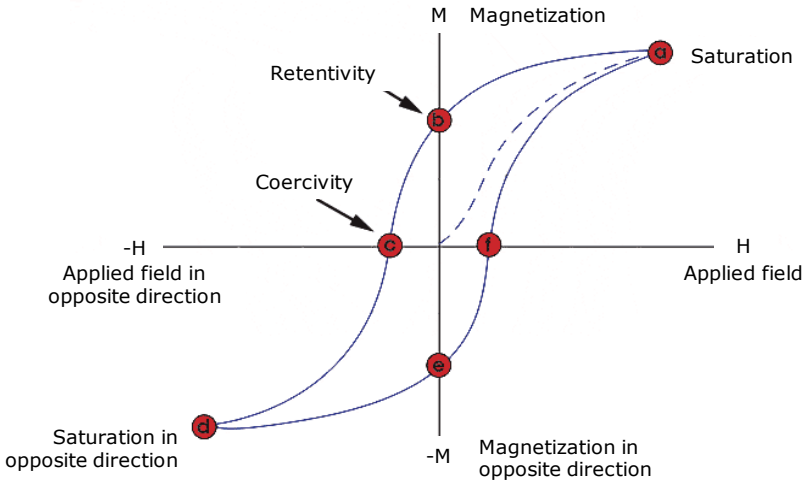

Figure 3.13: Typical magnetization curve of a ferromagnetic compound. Adapted from [40].

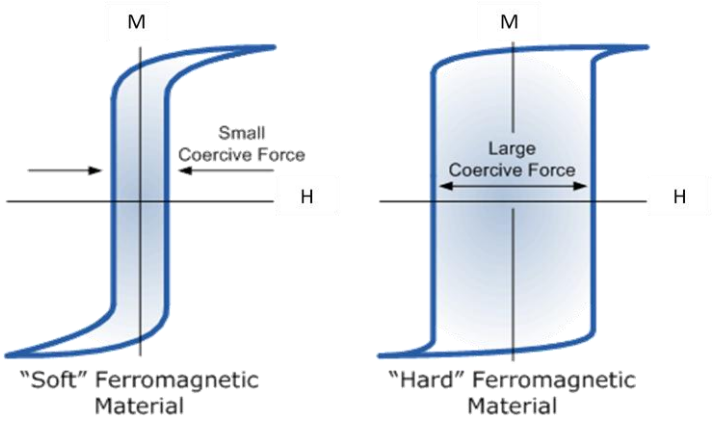

Figure 3.14: Representation of magnetization curves of hard and soft ferromagnets. [41]

Table 3.4: Magnetic properties measured at 298 K of the samples reduced in liquid phase.

Sample	M_s [a] /emu.g^{-1}	M_r [b] /emu.g^{-1}	H_c [c] /Oe
Ni commercial	52.5	4.3	80
NiAc(200°C)– N_2H_4	54.3	6.1	100
NiAc(400°C)– N_2H_4	37.4	4.0	70

a Saturation magnetization **b** Remanent magnetization **c** Coercivity

The saturation magnetization of the commercial nickel particles used as reference material is about 52.5 emu. g^{-1}. This value is close to the saturation magnetization of bulk nickel equal to 55 emu. g^{-1} at room temperature [42–44]. The saturation magnetization of the sample NiAc(200°C)– N_2H_4 is close to that of reference material (**Figure 3.12**); this result is in concordance with the XRD results that showed a pure nickel compound. Whilst M_s of NiAc(400°C)– N_2H_4 is lower than the one of the reference material; this lower value can be assigned to the large amount of NiO present in the sample which is antiferromagnetic as bulk material. Furthermore, the value of H_c is in the same range for all samples and it is characteristic of a soft ferromagnetic behavior. Identically, remanent magnetization is of same order for the three materials. The magnetic properties of the samples are summarized in **Table 3.4**.

Particles obtained via reduction in gas phase

Results obtained for samples reduced in gas phase are presented in **Figure 3.15**. Similarly to the samples reduced in liquid phase, the normalized magnetization curves of these samples present a shape which is characteristic of ferromagnetic materials. For NiAc(200°C)– H_2 sample, the value of M_s is again decreased due to the presence of NiO (close to 23 wt%). For NiAc(400°C)– H_2 sample that contains 98 wt% of NiO, the ferromagnetic properties are almost inexistent.

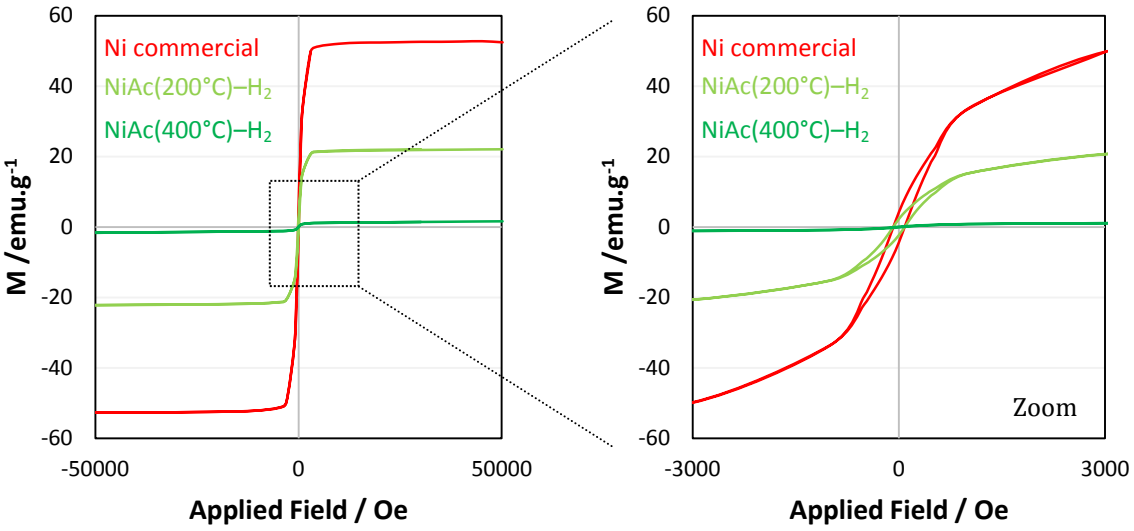

Figure 3.15: Normalized magnetization curves at 298 K of particles obtained via reduction in gas phase of the two types of nickel precursors (left) and zoom between – 3 and 3 kOe (right).

Besides, as previously, the value of H_c is in the same range for all samples and is characteristic of soft ferromagnets. However, remanent magnetization was decreased with increasing amount of NiO phase. This tendency was not observed in the case of the samples reduced in liquid phase

thought significant difference in NiO amount was observed between the samples; the same tendency can be noticed with the M_S here. These differences may arise from a difference of configuration of Ni-NiO in the particles synthesized using a reduction in gas phase as compared to those obtained using a reduction in liquid phase. The magnetic properties of the samples are summarized in **Table 3.5**.

Table 3.5: Magnetic properties measured at 298 K of the samples reduced in gas phase.

Sample	M_s [a] /emu. g^{-1}	M_r [b] /emu. g^{-1}	H_c [c] /Oe
Ni commercial	52.5	4.3	80
NiAc(200°C)– H_2	22	2.3	80
NiAc(400°C)– H_2	1.6	0.1	60

a Saturation magnetization **b** Remanent magnetization **c** Coercivity

- In conclusion, the reduction process is more efficient independently from the chemical procedure nature (in liquid or gas phase) starting from NiAc(200°C) nickel precursor. Indeed, in this case, metallic nickel (100 wt%) was obtained from a reduction in liquid phase and a material with 77 wt% was obtained from a reduction in gas phase. While starting from the NiAc(400°C) precursor, a mixture of nickel (5 to 10 wt%) and nickel oxide (95 to 98 wt%) was obtained.
- After the two types of reduction processes, the particles issued from the nickel precursor NiAc(200°C) present better homogeneity in size as compared to those issued from NiAc(400°C).
- Magnetization measurements performed on the different samples show that they exhibit soft ferromagnetic behavior. Besides, the presence of NiO in the samples lowers the saturation magnetization. In the case of mixed NiO/Ni particles, it is of great importance to determine the structural configuration of the latter: i.e. either a Ni–NiO core–shell structure or the reverse. Therefore, a characterization using microcalorimetry can be performed in order to define this feature of the unconfined particles synthesized.

III.2.2. Reduction of confined nickel precursors in porous matrices

During this work, SEO–type mesoporous silica and carbon matrices were beforehand prepared according to the syntheses presented in *Chapter 1*. The growth of nickel nanoparticles in the porosity of the matrices was performed in two steps: the impregnation of the latter with solution of nickel acetate salt followed by a chemical reduction in gas or liquid phase.

III.2.2.a. Impregnation step

The impregnation was performed under ambient conditions. In a typical preparation, the powdered mesoporous silica or carbon support was dispersed into the nickel salt solution in proportion of 100 mg of solid for 2 mL and 0.5 mL of solution, respectively. The impregnation process was performed with a nickel acetate solution of concentration set to 0.5 M. For achieving equilibrium in the system, the suspension was thermostated at 25°C and agitated during 48 h for the silica matrix and 24 h for the carbon one. After impregnation, the Ni salt@Silica or Ni salt@Carbon sample was gathered by centrifugation and rinsed several times with distilled water in order to remove residual species from the surface. Lastly, the sample was collected the same way after washing and was dried at 80°C.

III.2.2.b. Silica matrices: chemical reduction in gas phase and characterization

The chemical reduction chosen for the nanocomposites obtained from silica matrix was the one in gas phase since the high pH of the medium during the reduction in liquid phase causes decomposition of the silica leading to a dramatic loss of the porous structure. After thermal treatment at 200°C or 400°C of Ni salt@Silica, the reduction in gas phase of the latter was performed using hydrogen following the procedure developed in the preliminary study. The samples were degassed at room temperature then purged with argon/hydrogen (95/5 molar ratio) mixture to ensure the atmosphere purity in the reduction system. Finally, the samples were treated under the same Ar/H_2 mixture at 350°C (with a heating rate of 2°C. min^{-1}) during 16 h in order to favor a complete reduction. The two *Nickel NPs@Silica* nanocomposites prepared are denoted as Ni(200°C)@SiO_2 and Ni(400°C)@SiO_2. The color of the samples changes from green to gray after reduction treatment as shown in **Figure 3.16**. The different samples obtained were characterized using nitrogen adsorption/desorption at 77 K, TEM, XRD and magnetization measurements.

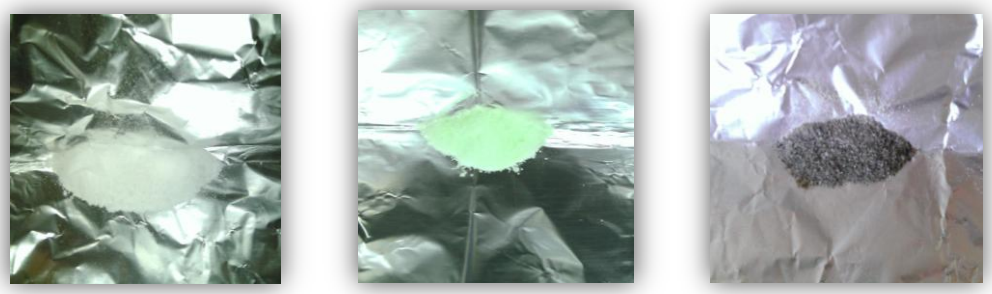

Figure 3.16: Photographic images of the samples SiO_2 (a), Ni salt@SiO_2 (b), Ni(200°C)@SiO_2 and Ni(400°C)@SiO_2 (c).

The textural properties of the samples were investigated using nitrogen adsorption/desorption measurements at 77 K. The isotherms (not shown) have the same shape as the parent silica one: they are characterized as mixed type *I* and *IV* and present hysteresis loop of type *H1*. They are shifted to lower adsorbed volumes indicating a decrease of porosity (**Table 3.6**).

Table 3.6: Textural properties of the samples SiO_2, Ni(200°C)@SiO_2 and Ni(400°C)@SiO_2.

Sample	S_{BET} [a] /$m^2.g^{-1}$	$V_{\mu porous}$ [b] /$cm^3.g^{-1}$	$V_{total\ pore}$ [c] /$cm^3.g^{-1}$	D_{pore} [d] /nm
SiO_2	380	0.050	0.5	8.5
Ni(200°C)@SiO_2	210	0.015	0.4	8
Ni(400°C)@SiO_2	330	0.010	0.5	8

a BET surface area
b Microporous volume
c Total pore volume
d Pore size at the maxima of pore size distribution

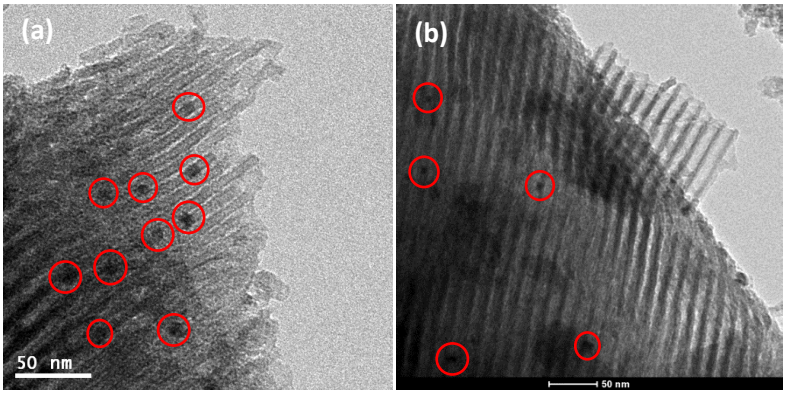

Figure 3.17: TEM images of the nanocomposites Ni(200°C)@SiO_2 (a) and Ni(400°C)@SiO_2 (b).

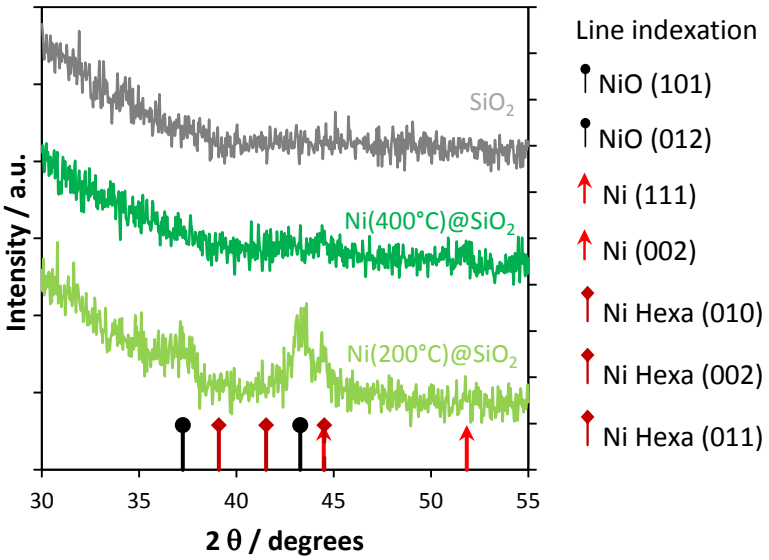

Figure 3.18: X-ray diffraction patterns of SiO_2, Ni(200°C)@SiO_2 and Ni(400°C)@SiO_2. The line indexation in the order of appearance for each line is presented on the right side.

Transmission electron microscopy permits the identification of nanoparticle size with mean diameter around 7 nm located in the silica host matrix for both samples Ni(200°C)@SiO_2 (**Figure 3.17 (a)**) and Ni(400°C)@SiO_2 (**Figure 3.17 (b)**). The presence of nanoparticles in the pore systems explains the decrease of the textural properties in both samples (pore blocking effect).

XRD analysis was performed in order to indentify the composition of the nanoparticles grown in the nanocomposites. The XRD patterns of the pristine silica and the two nanocomposites are presented in **Figure 3.18**. The silica matrix is amorphous thus the characterization of the samples is complicated: nickel or nickel oxide diffraction lines may not be necessarily well depicted in XRD patterns due to the low amount of particles as compared to the unconfined particles synthesized. Thus one should note that this characterization is more relative than quantitative. As it can be seen, only the most intense peaks of NiO (012) and Ni (111) are unambiguously visible in the XRD pattern of Ni(200°C)@SiO_2. As compared to the unconfined material NiAc(200°C)– H_2, we cannot confirm or refute the presence of Ni hexagonal in the composition. Concerning the sample Ni(400°C)@SiO_2, it was not possible to determine any diffraction lines of Ni or NiO.

- In conclusion, using a reduction treatment in gas phase, the incorporation of nickel-based nanoparticles within the silica matrix was achieved. Nanoparticles with a mean size around 7 nm were obtained for both nanocomposites Ni(200°C)@SiO_2 and Ni(400°C)@SiO_2.
- The XRD analysis was relative. Nanoparticles in Ni(200°C)@SiO_2 were composed of a mixture containing at least Ni cubic and NiO rhombohedral phases. However, the identification of the phases present in the case of Ni(400°C)@SiO_2 was less obvious; it was not possible to detect the phases present.

III.2.2.c. Carbon matrices: chemical reduction in liquid phase and characterization

The chemical reduction chosen for the nanocomposites obtained from carbon matrix was the one in liquid phase because the temperature applied during the reduction in gas phase could cause a modification of the carbon porosity. Commercial Carbon Norit was used as a reference matrix for the reduction treatment since it possesses high specific area and micropores. Besides, it will allow validating the reduction process on an easily affordable material beforehand, since the synthesis of the Carbon matrix studied herein takes time and yield in few amounts of material. The reduction in liquid phase of impregnated Carbon synthesized matrix, previously treated thermally in air at the temperatures of 200°C or 400°C, was performed with a mixture of

64 % hydrazine and 20 M sodium hydroxide following the procedure developed during the preliminary study. The carbon Norit being decomposed from a temperature of 400°C in air, as shown in **Figure 3.19 (a),** the thermal treatment chosen to grow nickel oxide nanoparticles in this matrix was set to 350°C. Indeed, a very little variation in weight (~2 wt%) was observed during the thermogravimetric analysis after a procedure of 350°C for 4 h in air atmosphere, **Figure 3.19 (a inset)**. Similarly, the Carbon synthesized decomposes as the carbon Norit in air from 400°C, **Figure 3.19 (b)**. However, in order to prevent totally the decomposition of the matrix, the atmosphere used in order to grow NiO nanoparticles was nitrogen instead of air since it does not decomposes in inert atmosphere, **Figure 3.19 (b)**. In a typical procedure, the thermally pre-treated samples were then treated at 80°C for 0.5 h, afterwards hydrazine and sodium hydroxide solutions were added in excess with the starting material ratio 200 mg : 5 mL : 5 mL [NiAc(T)@Carbon : N_2H_4 : NaOH]. The mixture was left to react for 6 h (two times more than the reference materials) to favor a complete reduction. The mixture color was black due to the suspension of carbon materials (which has a black color). The obtained black solids were filtered then dried in air at 80°C.

Four nanocomposites were prepared: Ni(200°C)@Carbon Norit and Ni(350°C)@Carbon Norit using reference carbon matrix, and Ni(200°C)@Carbon and Ni(400°C)@Carbon using the Carbon synthesized matrix. The different samples obtained were characterized using nitrogen adsorption/desorption at 77 K, TEM, XRD and magnetization measurements.

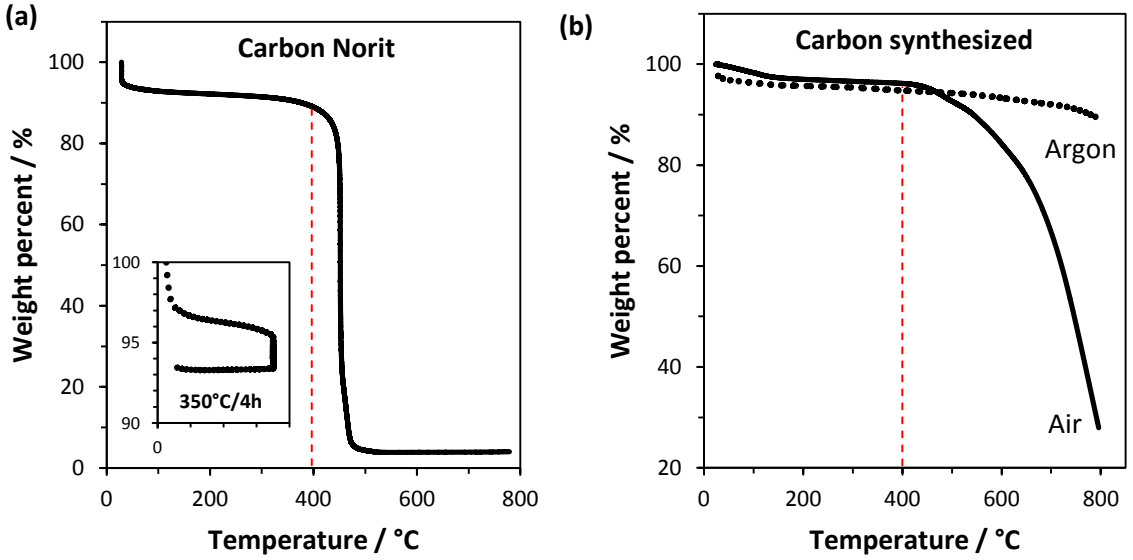

Figure 3.19: TGA profiles of carbon Norit in air atmosphere with a linear treatment (a) and with a procedure of 350°C/4h (a inset), and TGA profiles of carbon synthesized in air and inert atmosphere (argon) (b).

The textural properties of the samples made of the two types of carbon matrices, commercial Carbon Norit and synthesized Carbon, were investigated using nitrogen adsorption/desorption measurements at 77 K (**Figure 3.20**).

Concerning the samples Carbon Norit and Ni(200°C)@Carbon Norit, the isotherms are characterized by an initial sharp uptake at relative pressures below 0.05 followed by a long plateau up to the end of the adsorption branch. According to the IUPAC, such isotherms are characterized as type *I*, characteristic of microporous samples. The isotherm of sample Ni(350°C)@Carbon Norit exhibits a more gradual uptake and a desorption branch that is slightly shifted compared to the adsorption one. This feature indicates that the textural properties of the matrix are certainly modified by the heating treatment at 350°C followed by the hydrazine treatment. Indeed measurements performed for carbon Norit treated likewise showed a change in the isotherm shape.

Concerning the nanocomposites made of synthesized carbon, the isotherms have the same shape as the parent Carbon synthesized one: they are characterized as mixed type *I* and *IV* (they possess both micropores and few primary mesopores) and present hysteresis loop of type *H4*.

For all samples, as observed for the nanocomposites made from silica, a shift of isotherms is observed indicating decrease of the porosity with the incorporation of Ni-based particles. Textural properties of all samples are presented in **Table 3.7**.

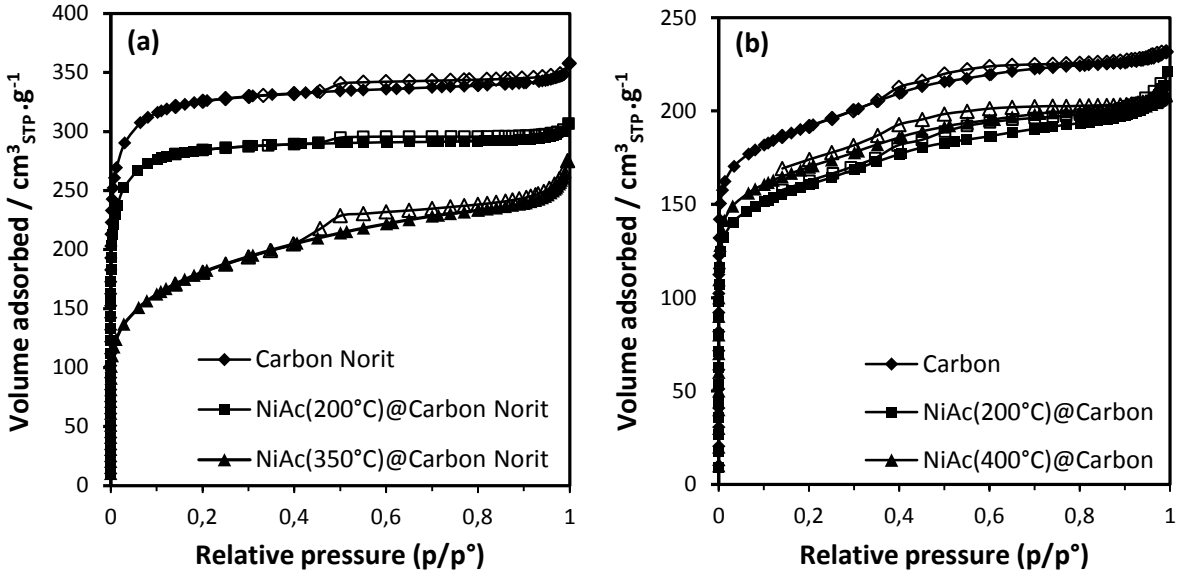

Figure 3.20: Nitrogen ad-/desorption isotherms at 77 K of Carbon Norit, Ni(200°C)@Carbon Norit, Ni(350°C)@Carbon Norit (a) and Carbon, Ni(200°C)@Carbon, Ni(400°C)@Carbon (b).

Table 3.7: Textural properties of Carbon Norit, Ni(200°C)@Carbon Norit, Ni(350°C)@Carbon Norit and Carbon, Ni(200°C)@Carbon, Ni(400°C)@Carbon samples.

Sample	S_{BET} [a] $/m^2.g^{-1}$	$V_{uporous}$ [b] $/cm^3.g^{-1}$	$V_{total\ pore}$ [c] $/cm^3.g^{-1}$	D_{pore} [d] /nm
Carbon Norit	1250	0.41	0.51	< 2
Ni(200°C)@C Norit	1100	0.36	0.45	< 2
Ni(350°C)@C Norit	640	0.1	0.33	< 2
Carbon	700	0.2	0.35	< 2 + 2.5–3
Ni(200°C)@Carbon	595	0.16	0.29	< 2 + 2.5–3
Ni(400°C)@Carbon	660	0.18	0.34	< 2 + 2.5–3

a BET surface area
b Microporous volume
c Total pore volume
d Pore size at the maxima of pore size distribution (for D_{pore} > 2 nm)

The specific surface area of Carbon Norit is approximately twice higher than the one of the Carbon synthesized in this study. For both type of carbon, a decrease of the textural properties is observed after incorporation of the nickel-based nanoparticles probably due to pore blocking effect as suggested the shift of the isotherms to lower values. Besides, Ni(200°C)@Carbon has lower textural properties than Ni(400°C)@Carbon as found in the case of silica matrix. Furthermore, after a thermal treatment at 350°C followed with a treatment with a mixture of N_2H_4–NaOH (similarly to the nanocomposites) for commercial Carbon Norit, changes in the isotherm shape and textural properties can be observed. A significant decrease in the textural properties suggests that the structure and/or texture of Carbon Norit changes after this treatment.

Transmission electron microscopy permits the identification of the nanoparticle size and location in the carbon matrix. For the samples issued from Carbon Norit, no images are presented herein since it was not possible to observe clearly the pore system neither the presence of particles. TEM images in bright field and in dark field modes of the nanocomposites issued from the Carbon synthesized show the presence of nanoparticles located in the pores of the carbon matrix. For both samples Ni(200°C)@Carbon and Ni(400°C)@Carbon, nanoparticles of mean size around 3 nm are observed, **Figure 3.21** and **Figure 3.22**. The presence of nanoparticles in the pore systems can explain the pore blocking effect leading to a decrease of the textural properties in both samples.

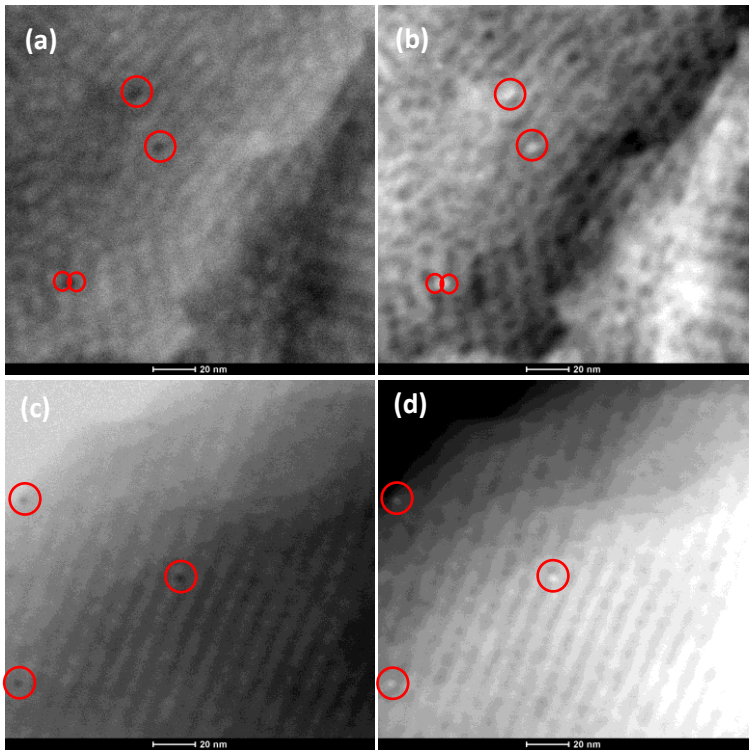

Figure 3.21: TEM images in bright field (a–c) and in dark field (b–d) modes of the nanocomposite Ni(200°C)@Carbon.

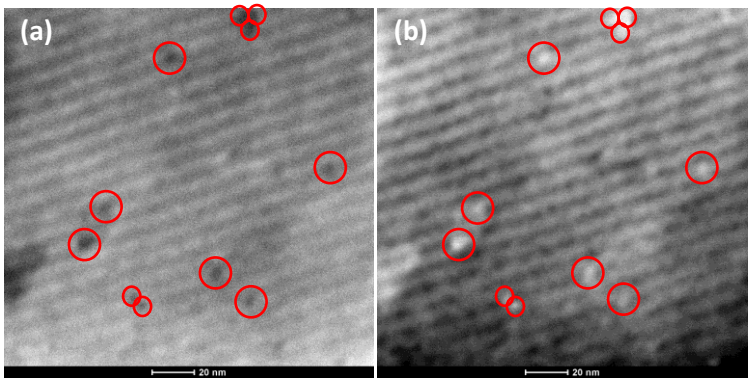

Figure 3.22: TEM images in bright field (a) and in dark field (b) modes of the nanocomposite Ni(400°C)@Carbon.

XRD analysis was performed in order to indentify the phases present in the nanocomposites (**Figure 3.23**). The nanocomposite Ni(200°C)@Carbon Norit displays diffraction lines of Ni cubic. No distinct diffraction peaks other than those from Ni cubic is found in the sample in the X-ray diffraction limit. The sample Ni(350°C)@Carbon Norit exhibits diffraction lines of Ni cubic as well as NiO. In order to estimate relatively the percentages in weight of the two phases in this sample, the carbon Norit XRD pattern was subtracted from the nanocomposite one. It results that the weight percents of Ni cubic and NiO are estimated around 32.9 wt% and 67.1 wt% respectively. These results are in good agreement with the reference material, NiAc(400°C)– N_2H_4, in which a mixture of the two phases was obtained. One can note that the

percentage of Ni cubic is much higher in the nanocomposite as compared to the reference material. This difference can be explained by the fact that the ratio between the amount of nickel precursor and the reducing agent is much lower than in the case of the reference material (for a same amount of nickel precursor there is more reducing agent) and that the objects that have to be reduced are in the nanometer range. For Ni(200°C)@Carbon and Ni(400°C)@Carbon, the identification of phases present in the nanocomposites is much more difficult as the response of the pure carbon matrix is more intense in a wide 2θ range.

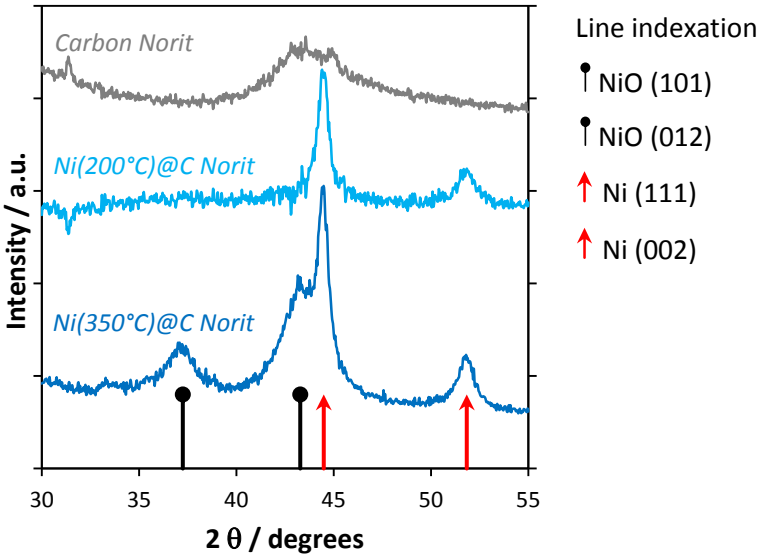

Figure 3.23: X-ray diffraction patterns obtained for the samples Ni(200°C)@Carbon Norit and Ni(400°C)@Carbon Norit.

Magnetization measurements of the nanocomposite samples synthesized starting from the Carbon Norit matrix were performed in an external field of 50 kOe at room temperature (298 K) in order to evaluate their magnetic behavior (**Figure 3.24**). In the case of nanocomposites, the value of magnetization was not normalized per gram of solid but per gram of incorporated Ni. In order to perform this normalization, the adsorbed amount of nickel acetate in the carbon matrix was measured using UV-visible spectroscopy and the following assumptions were made: all adsorbed nickel acetate is present in the porous structure and all is converted to Ni-based particles. Amounts of nickel acetate adsorbed in the nanocomposite substrates were estimated to $\sim 8.2\ 10^{-4}$ mol per gram of solid. As shown in **Figure 3.24**, the Carbon Norit matrix exhibits diamagnetic behavior and the samples Ni(200°C)@Carbon Norit and Ni(400°C)@Carbon Norit displayed a ferromagnetic behavior similarly to the commercial nickel particles. The magnetic properties of the samples are summarized in **Table 3.8**.

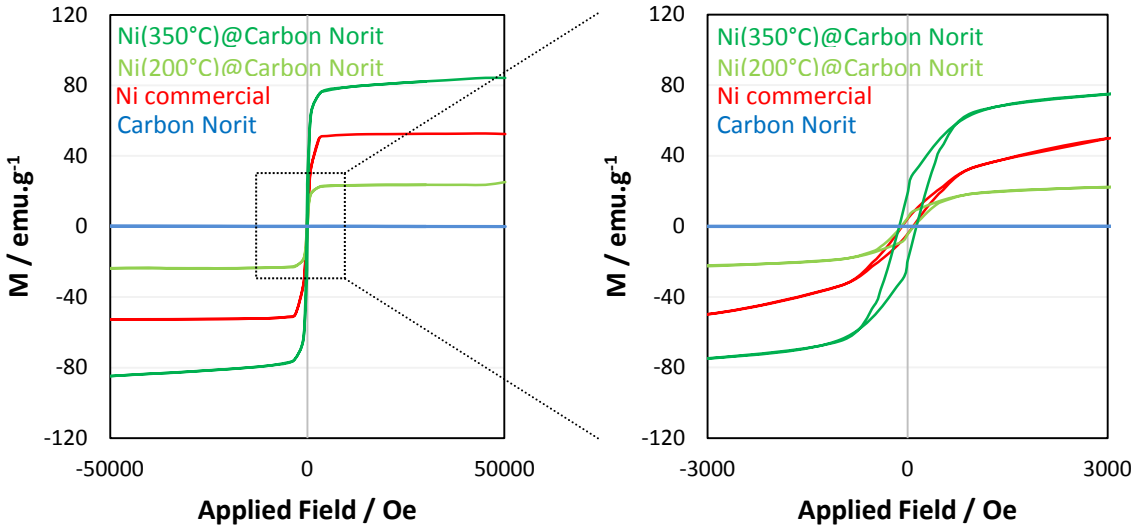

Figure 3.24: Normalized magnetization curves of Ni(200°C)@Carbon Norit and Ni(350°C)@Carbon Norit, measured at 298 K (left) and zoom between – 3 and 3 kOe (right).

Table 3.8: Magnetic properties measured at 298 K of the different samples studied.

Sample	T measurement	M_s [a] / emu. g^{-1}	M_r [b] / emu. g^{-1}	H_c [c] /Oe
Ni commercial		52.5	4.3	80
Ni(200°C)@Carbon Norit	298 K	25.2	4.8	90
Ni(350°C)@Carbon Norit		84.2	19.5	130

a Saturation magnetization **b** Remanent magnetization **c** Coercivity

At room temperature, as shown in **Table 3.8**, the value of the remanent magnetization M_r of sample Ni(200°C)@Carbon Norit is lower than the one of commercial nickel whereas the one of Ni(400°C)@Carbon Norit is higher. The value of the coercive field H_c is slightly higher for the later sample as compared to the two other ones. These results are difficult to interpret. Indeed, one has to consider the size of incorporated particles, the chemical composition (pure Ni or mixture of Ni/NiO) and the configuration of these 'mixed' particles. As the Carbon Norit matrix exhibits mainly micropores, one can consider that a large percentage of Ni-based nanoparticles present a diameter lower than 2 nm.

It is reported that the magnetic properties of nanosized nickel particles are enhanced for clusters containing less than 400 atoms i.e. for particles exhibiting a diameter lower than 3 nm (**Figure 3.25**). [45] Furthermore, it is also reported that small Ni nanoparticles (as powder or incorporated in matrices) and core–shell nanoparticles of type Ni–NiO, exhibit a superparamagnetic behavior [28,46,47]. It is also found in the literature that nanosized NiO particles present ferromagnetic properties [48,49].

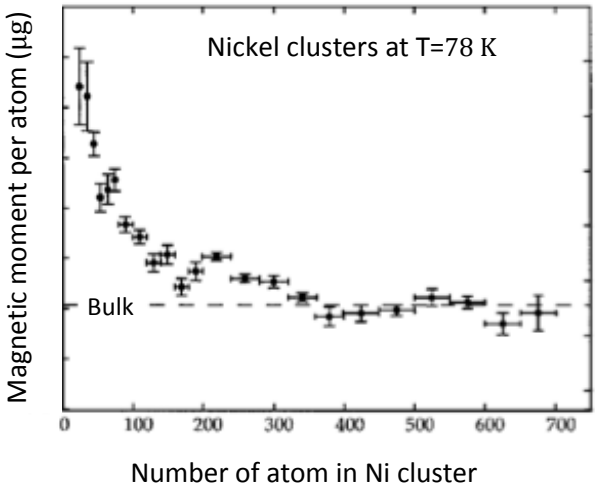

Figure 3.25: Representation of the magnetic moment per atom as a function of the number of atom in nickel clusters.

Therefore, it is not possible to conclude considering solely these results. To have access to more information about the magnetic properties of these Ni-based nanoparticles incorporated in carbon matrix, Zero Field Cooling/Field Cooling (ZFC/FC) measurements are envisaged. Indeed, this type of measurement will permit to observe (or not) the transition between the superparamagnetic state and the blocked one and to have information about the nanoparticle size, their size distribution and their magnetic interactions.

- In conclusion, the incorporation of nickel-based nanoparticles within the synthesized carbon matrix was achieved using chemical reduction liquid phase. Nanoparticles with a mean size about 3 nm were obtained in nanocomposites Ni(200°C)@Carbon and Ni(400°C)@Carbon. It was not possible to observe Carbon Norit structure and thus neither the particles incorporated.
- XRD analysis permitted to determine the nanocomposite phase compositions. Similarly to their unconfined reference material, only a phase of Ni cubic was detected in the limit of detection for Ni(200°C)@Carbon Norit, while a mixture of Ni cubic and NiO rhombohedral was found in Ni(350°C)@Carbon Norit. The proportion of Ni in the latter was higher than in the reference material due to ratio between reducing agent and nickel precursor and to size effect. For the nanocomposites based of Carbon synthesized, it was not possible to detect the phases present due to strong signal of the carbon matrix.
- The Carbon Norit–based samples presented ferromagnetic behavior similarly to commercial nickel particles. Considering only the results obtained, it is difficult to give more conclusions on the magnetic properties of the nanocomposite samples.

III.3. Study of the nanocomposites hydrogen adsorption properties

III.3.1. Fundamentals of thermodynamics of adsorption in gas phase

The energies released during the adsorption process depend on the nature and the strength of the interactions between the adsorbent and the adsorbate (adsorbed probe molecules). These energies of interaction are a measure of the amount of heat that is released upon adsorption and are known as differential adsorption enthalpies. Moreover, over a certain change in coverage, these adsorption energies can give information on the homogeneity or heterogeneity of the investigated surface. Indeed, an adsorbent presenting an energetically homogeneous surface, i.e. just one type of adsorption sites, would generally present constant enthalpies as a function of surface coverage. While on a heterogeneous surface, different strengths of adsorbent–adsorbate interactions are present; the strongest sites being occupied first, this leads to decreasing adsorption enthalpies as a function of surface coverage. Heterogeneity of the surface can be assigned to pore size distribution or variation of the surface chemistry. Besides, the adsorbate–adsorbate interactions can be sufficiently strong to overlap with the interaction of the probe molecules and the solid resulting for example in an increase of the energy of adsorption with increasing coverage. [50] These three basic interactions, presented in **Figure 3.26**, contribute to the measured differential adsorption enthalpies.

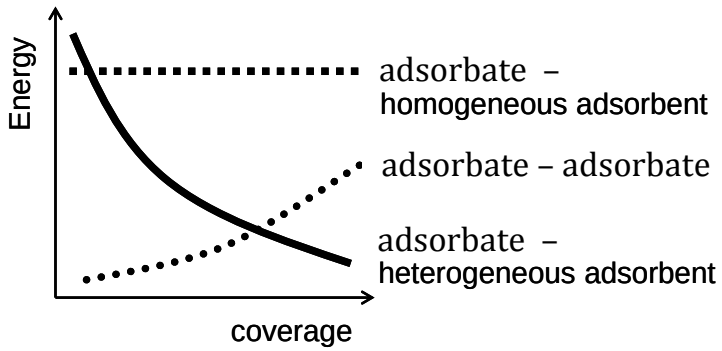

Figure 3.26: Representation of the basic interactions contributing to adsorption energies. [51]

The study of the interactions between a gas and a solid surface can be performed using several techniques. Among them, microcalorimetry appears as a powerful experimental technique for characterizing the surface chemistry of adsorbents and investigating adsorption mechanisms such as phase changes and transitions [52]. Indeed, it is able to highlight the presence of different adsorption sites and can be used in combination with other techniques. For instance, microcalorimetry coupled with manometry is the only technique that gives information about the interactions of the studied probe molecule with the surface by directly measuring the enthalpies of adsorption accurately even at low pressures. This combination of both techniques,

so-called adsorption microcalorimetry, allows the simultaneous measurement of adsorption isotherms and corresponding differential enthalpies.

Principle of adsorption microcalorimetry [51]

Adsorption microcalorimetry measurements can be carried out using different types of calorimeter. The calorimeter used within this work is a Tian-Calvet–type microcalorimeter coupled to a homemade manometric device, **Figure 3.27**. It works under isothermal conditions (constant temperature *T*) and is identified as a diathermal-conduction calorimeter: the heat produced during the adsorption process in the cell is transferred to the device thermocouple through the surroundings temperature by simple conduction.

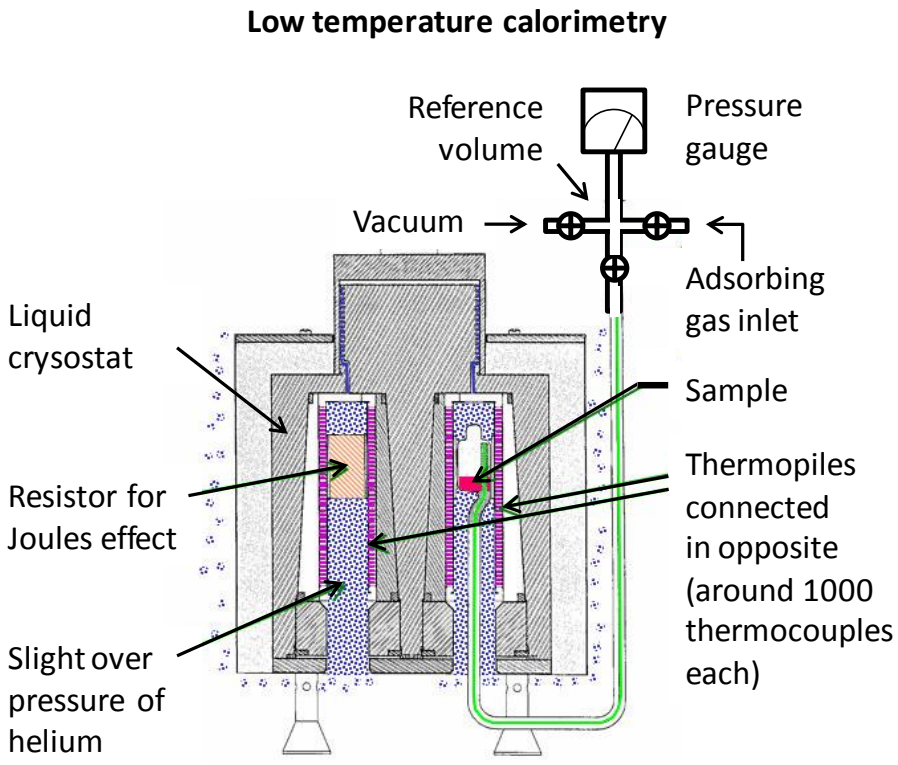

Figure 3.27: Schematic representation of the microcalorimeter coupled with manometric device used within this work.

Using this experimental setup, the enthalpies of adsorption can be obtained as described in the following and in correspondence with **Figure 3.28**.

Over the manometric device, the gas is added to the sample using a point-by-point introduction with increasing pressure. At each introduction of gas (point A in **Figure 3.28**) an exothermic thermal effect is detected and equilibrium (point B in **Figure 3.28**) is attained. The detected peak curve of energy with time has to be integrated to provide an integral (pseudo-differential) molar

enthalpy of adsorption for each dose. Under these conditions the differential enthalpy of adsorption $\Delta_{ads}\dot{h}$ can be calculated with the following equation [50]:

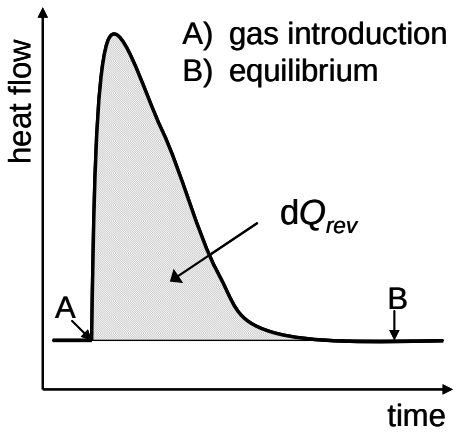

Figure 3.28: Schematic view for the heat flow detected at one gas introduction. [51]

Equation 3.1

$$\Delta_{ads}\dot{\boldsymbol{h}} = \left(\frac{\boldsymbol{dQ_{rev}}}{\boldsymbol{dn^a}}\right)_{\boldsymbol{T}} + \boldsymbol{V_c} \times \left(\frac{\boldsymbol{dp}}{\boldsymbol{dn^a}}\right)_{\boldsymbol{T}}$$

Where:

dQ_{rev}	is the heat reversibly exchanged with the surroundings and as measured by the microcalorimeter at the temperature T
dn^a	is the adsorbed amount of gas after the introduction of each dose
V_c	is the dead space volume of the applied sample cell.
dp	is the increase in pressure

The results of such experiments are thus presented as the (pseudo)differential enthalpies of adsorption, in $-\,\mathrm{kJ.mol^{-1}}$, as a function of pressure or of amount adsorbed (surface coverage). The enthalpies of adsorption $\Delta_{ads}\dot{h}$ associated to the two types of adsorption are in different energy range: $\left|\Delta_{\mathrm{ads}}\dot{\mathrm{h}}\right| \leq 20\ \mathrm{kJ.mol^{-1}}$ (in the region of the energy of liquefaction of a gas) in physisorption while $\left|\Delta_{\mathrm{ads}}\dot{\mathrm{h}}\right| \geq 40\ \mathrm{kJ.mol^{-1}}$ (in the energy range of chemical bond formation) in chemisorption.

III.3.2. Bulk materials

Hydrogen adsorption properties of the bulk materials were investigated with a manometric device coupled with a microcalorimeter at 77 K and low pressures up to 0.8 bars. Two bulk samples, commercial nickel and nickel oxide nanopowders, were studied in order to evaluate the involved enthalpies of adsorption corresponding to the interaction between H_2 and the different type of surfaces: i.e. Ni metallic and Ni oxide. Then measurements of the enthalpies of adsorption for different samples will be presented.

Hydrogen adsorption properties of Ni nanopowder are presented in **Figure 3.29**. The evolution of the amount of H_2 adsorbed (n^{ads}) as a function of pressure is of linear−type which is typically observed when very low quantities of gas are adsorbed [53] (**Figure 3.29 (a)**). One has to remember that the specific surface area of Ni nanopowder is low ($S_{BET} = 5\ m^2.g^{-1}$), thus the surface available for the adsorption is low. The evolution of the enthalpies of adsorption ($\Delta_{ads}\dot{h}$) as a function of surface coverage is presented in **Figure 3.29 (b)**. Starting from a value of about $-17\ kJ.mol^{-1}$, the adsorption enthalpy rapidly decreases to a value fluctuating around $-2/-3\ kJ.mol^{-1}$. These fluctuations are due to a problem of calorimeter stability related to the low adsorbed amounts. The evolution of the adsorption enthalpies as a function of hydrogen coverage is typical of a heterogeneous surface from an energetic point of view, i.e. different adsorption sites are involved in the hydrogen adsorption.

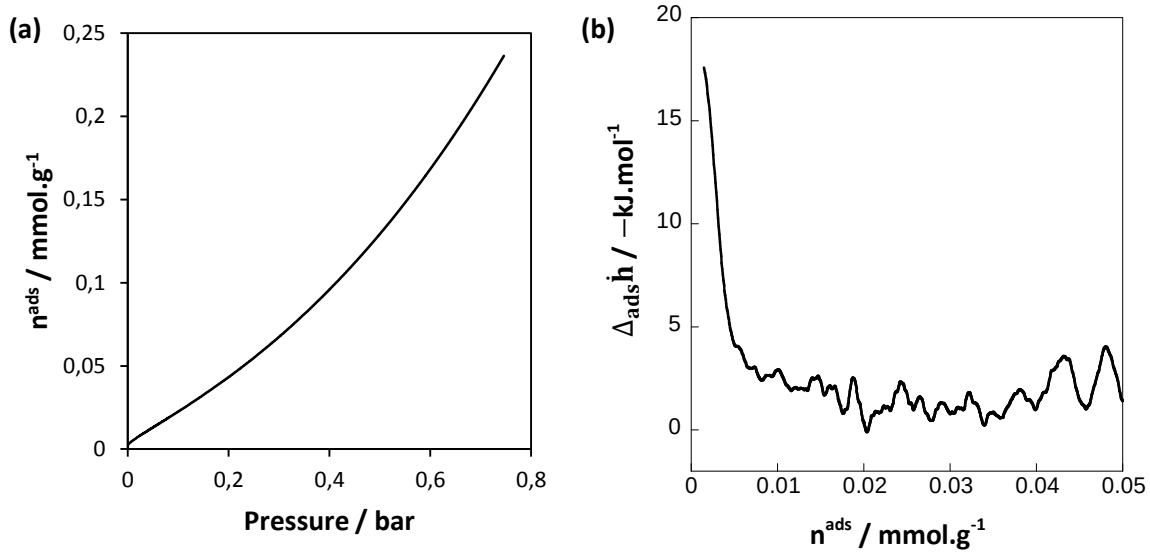

Figure 3.29: Adsorption of hydrogen on Ni nanopowder at 77 K: adsorbed amount as a function of pressure (a) and enthalpies of adsorption as a function of surface coverage (b).

The hydrogen adsorption properties of the different unconfined particles synthesized within this work are summarized in **Table 3.9**. It can be observed that the energies of interaction measured for the materials issued from reduction in liquid phase are higher than those issued from reduction in gas phase. Indeed, for the unconfined particles obtained in the first case, values of enthalpies of adsorption are close to the one of commercial nickel. Whilst, for those obtained after a treatment in gas phase, values of enthalpies are closed to the one found for nickel oxide.

These results allow determining the physical configuration of the different samples. Particles reduced in liquid phase are composed of a surface of metallic nickel and a core containing NiO

(when NiO is present) whereas those reduced in gas phase are either in the reverse configuration or composed entirely of a mixture of both Ni and NiO.

Table 3.9: Enthalpies of adsorption at low coverage of the different samples studied at 77 K.

Sample	$\Delta_{ads}\dot{h}\ /-\mathbf{kJ.mol^{-1}}$
Ni commercial	17
NiO commercial	4
Reduction in liquid phase	
NiO commercial	20
NiAc(400°C)	14
Reduction in gas phase	
NiAc(400°C)	7
NiAc(200°C)	8

- The reduction in liquid phase leaded to the formation of nickel-based particles with a metallic surface exhibiting a value of enthalpies of adsorption close to the one of commercial nickel. This feature will permit having similar energies of interactions in the nanocomposites prepared according to the same procedure, i.e. Ni(200°C)@Carbon and Ni(400°C)@Carbon, giving access to a nanocomposite interesting for hydrogen storage.
- The reduction in gas phase leaded to particles containing NiO at their surface which prevent high energies of interactions with hydrogen.

III.3.3. Nanocomposites

III.3.3.a. Silica-based nanocomposites

The hydrogen properties of the nanocomposites synthesized during this work were investigated. Interpretation of the results obtained for Ni(200°C)@SiO_2 only will be presented since similar results were obtained for both nanocomposites (Ni(200°C)@SiO_2 and Ni(400°C)@SiO_2). The adsorption isotherm of hydrogen at 77 K onto the nanocomposite Ni(200°C)@SiO_2 is presented in **Figure 3.30**.

No multilayers of hydrogen can be formed at 77 K, because the interaction strength between single layers is too weak at temperatures higher than the critical temperature of H_2 (33 K). Therefore, a type *I* isotherm is typically obtained for porous materials at adsorption temperatures higher than the critical temperature of the gas. [54] The shape of the isotherms are then characterized as type *I*, known also as Langmuir–type (or *L*–type), according to IUPAC. Indeed, it describes the formation of a single monolayer on the surface of porous materials.

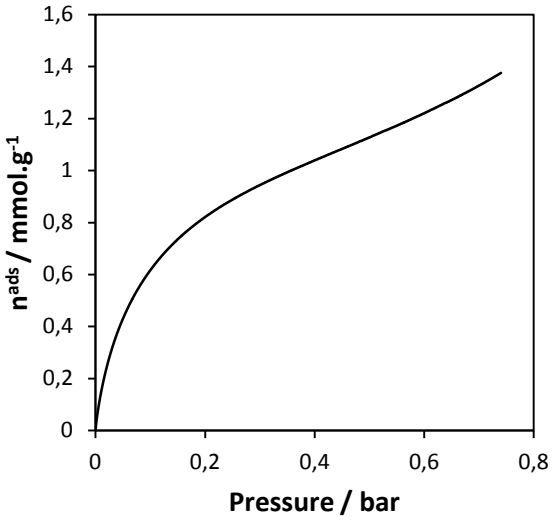

Figure 3.30: Adsorption isotherm of hydrogen onto Ni(200°C)@SiO_2 at 77 K.

The adsorption isotherm of H_2 for Ni(200°C)@SiO_2 starts as a type *I*, but surprisingly beyond 0.4 bars the amount of H_2 adsorbed (n^{ads}) tends to increase as a function of the pressure instead of reaching a plateau as it could be expected for this type of isotherm.

The energies of interactions during adsorption of hydrogen were measured simultaneously. The value of the enthalpies of adsorption ($\Delta_{ads}\dot{h}$) at low surface coverage in Ni(200°C)@SiO_2 is quite low; it is about -4 kJ. mol^{-1}. This value is close to values generally found for oxide surfaces, similarly to the reference unconfined material. This result suggests that the surface of the nanoparticles incorporated in the silica matrix may be composed of NiO. Furthermore, the oxidative environment of silica probably does not help for a stabilization of the nanoparticle surface into its metallic state.

Besides, given the low energies of interactions during H_2 adsorption on Ni(200°C)@SiO_2, one can suppose that the increase in n^{ads} observed during the measurements may be due to experimental incertitude.

III.3.3.b. Carbon-based nanocomposites

The hydrogen properties of the Carbon synthesized during this work were studied. The adsorption isotherm of hydrogen at 77 K onto the carbon is presented in **Figure 3.31**. The shape of the isotherm is characteristic of Langmuir–type: there is an increase of the amount of H_2 adsorbed (n^{ads}) up to reach saturation.

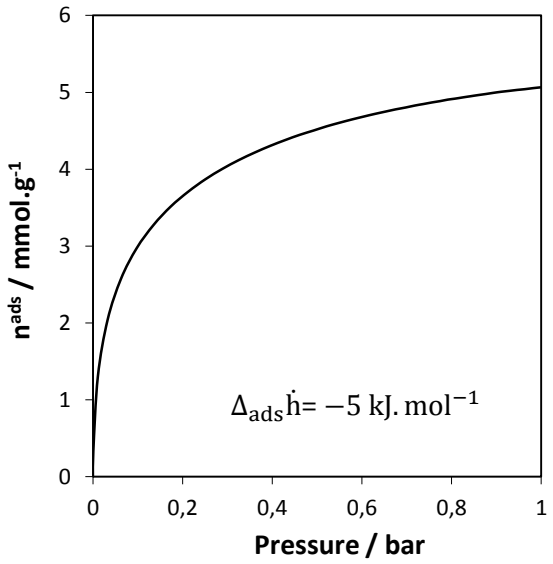

Figure 3.31: Adsorption isotherm of hydrogen on Carbon synthesized at 77 K.

The energies of interactions during adsorption of hydrogen were measured simultaneously. The value of the enthalpies of adsorption ($\Delta_{ads}\dot{h}$) at low surface coverage in the synthesized carbon is about -5 kJ. mol^{-1}. This value is similar to some found in the literature for silica materials as shown in **Table 3.10**.

Table 3.10: Hydrogen adsorption enthalpies at low coverage and 77 K of the Carbon synthesized and some commercial carbons.

Sample	S_{BET} /m^2. g^{-1}	$-\Delta_{ads}\dot{h}$ /kJ. mol^{-1}	H_2 uptake /wt%
Carbon synthesized	700	5	1
Carbon Norit R0.8 [55]	1384	5	2.9
Carbon AX-21_33 [56]	3304	5.53	5.32
Takeda 4A [55]	397	5.7	1.45

The adsorption capacity of porous materials is typically expressed as the gravimetric storage or volumetric storage. [54] The gravimetric storage is referred to the mass of adsorbent and of the adsorbed hydrogen (**Equation 3.2**) while the volumetric storage is related to the volume occupied by the solid (**Equation 3.3**). The total storage capacity can be obtained from the excess adsorption.

Equation 3.2
$$\%_{exc,grav} = \frac{n_{exc} \times M}{n_{exc} \times M + m} \times 100$$

Equation 3.3
$$\%_{exc,vol} = \frac{n_{exc} \times M \times \rho_{bulk}}{m} \times 100$$

Where:	n_{exc}	is the number of moles of gas molecules which are adsorbed in excess	$[mol]$
	m	is the adsorbent mass	$[g]$
	M	is the molar mass of the adsorbed molecule ($M = 2.01588\ g.mol^{-1}$ in the case of H_2)	$[g.mol^{-1}]$
	ρ_{bulk}	is the density of the adsorbent	

The maximum hydrogen adsorbed amount in the carbon synthesized is about 5 mmol. g^{-1} which is equivalent to 1 wt%. This value is far from the one found for Carbon AX-21_33 and Carbon Norit R0.8 but close to the amount adsorbed in Takeda 4A. One has to remember that the hydrogen uptake in the porous sorbent is related to the specific surface area available. The lower specific surface area of the Carbon synthesized as compared to Carbon AX-21_33 and Carbon Norit R0.8 yields in lower hydrogen uptake.

- In conclusion, the silica-based nanocomposites did not show expected enthalpies of adsorption, due to the oxide nature of the surfaces present in the material. The amount of hydrogen adsorbed in the synthesized carbon and the related enthalpies of adsorption give hope for future measurements with the nanocomposites. Indeed, combined with incorporated nickel nanoparticles playing the role of specific adsorption sites, this matrix may lead to a nanocomposite presenting interesting hydrogen adsorption properties.

Summary and prospects

The preliminary study was focused on the synthesis of unconfined nickel nanoparticles using two types of reduction procedures: one in liquid phase using hydrazine as reducing agent and the other in gas phase using hydrogen. Two nickel precursors were used: amorphous nickel acetate and crystalline nickel oxide. These two precursors were obtained after thermal treatments at 200°C and 400°C in air atmosphere, respectively. This study allowed determining the efficiency of the reduction process and the chemical nature and configuration of the nanoparticles synthesized particularly. It has been found that starting from NiAc(200°C) nickel precursor, the reduction process is more efficient independently from the chemical procedure nature (in liquid or gas phase). All the samples exhibited a ferromagnetic behavior. The presence of NiO was shown to decrease the saturation magnetization. Calorimetric measurements during adsorption of hydrogen allowed determining the surface nature of the particles, i.e. metallic or oxide surface. Particles issued from reduction in liquid phase presented values of enthalpies close to the one of commercial nickel showing their NiO–Ni core–shell configuration (when NiO is present). At contrary, particles issued from reduction in gas phase exhibited low enthalpies of

adsorption close to the ones of oxides revealing a reverse Ni–NiO configuration or mixture of Ni and NiO.

Then the incorporation of nanoparticles in the porous systems of the silica and carbon matrices was successful. Nanoparticles of about 7 nm were obtained for the nanocomposites based of silica while approximately 3 nm-sized nanoparticles were obtained for the nanocomposites based of carbon. In the case of silica-based nanocomposites, it was not possible with the reduction conditions used to reduce nickel at the surface; the nanoparticle surface is composed of NiO (as shown by calorimetric measurements). In the case of carbon-based nanocomposites, all results obtained on unconfined particles and on these nanocomposites allow us to predict the efficient reduction of nickel at the surface. Furthermore, hydrogen adsorption properties determined for laboratory-made carbon matrix are very encouraging. High enthalpies of adsorption associated with an interesting adsorption capacity are expected for the carbon-based nanocomposites Ni(200°C)@Carbon and Ni(400°C)@Carbon.

References

[1] Alternative Energies and Atomic Energy Commission (CEA) website: http://www.cea.fr/english-portal/energy/new-energy-technologies

[2] V.A. Yartis, M.V. Lototsky, 'An Overview of Hydrogen Storage Methods' in *Hydrogen Materials Science and Chemistry of Carbon Nanomaterials*, Springer: Netherlands, Vol. 172 (2005) pp. 75–104.

[3] L. Zhou, *Renewable Sustainable Energy Rev.*, 9 (2005) 395.

[4] U. Eberle, M. Felderhoff, F. Schüth, *Angew. Chem. Int. Ed.*, 48 (2009) 6608.

[5] J. Yang, A. Sudik, C. Wolverton, et al., *Chem. Soc. Rev.*, 39 (2010) 656.

[6] E. Fakioglu, Y. Yurum, T.N. Veziroglu, *Int. J. Hydrogen Energy,* 29 (2004) 1371.

[7] F. Schüth, B. Bogdanović, M. Felderhoff, *Chem. Commun.* (2004) 2249.

[8] R. Genma, N. Okada, T. Sobue, et al., *Int Int. J. Hydrogen Energy*, 31 (2006) 309.

[9] B. Sakintuna, F. Lamari-Darkrim, M. Hirscher, *Int. J. Hydrogen Energy,* 32 (2007) 1121.

[10] M.L. Christian, K.F. Aguey-Zinsou, *ACS Nano*, 6 (2012) 7739.

[11] R. Moury; U.B. Demirci; V. Ban, et al, *Chem. Mater.*, 26 (2014) 3249.

[12] Pragma Industries website: http://www.pragma-industries.com/products/hydrogen-storage/

[13] Hydrogen Components Incorporation website: http://www.hydrogencomponents.com/

[14] (a) NEEL Institute website: http://neel.cnrs.fr/

(b) McPhy Energy S.A. website: http://www.mcphy.com/en/

[15] (a) B. Panella, M. Hirscher, S. Roth, *Carbon*, 43 (2005) 2209. (b) W.C. Xu, K. Takahashi, Y. Matsuo, et al., *Int. J. Hydrogen Energy*, 32 (2007) 2504. (c) H.G. Schimmel, G.J. Kearley, M.G. Nijkamp, et al., *Chem. Eur. J.*, 9 (2003) 4764. (d) H.G. Schimmel, M.G. Nijkamp, G.J. Kearley, et al, *Mater. Sci. Eng., B,* 108 (2004) 124. (e) Q.R. Zheng, X. Ji, S. Gao, et al., *Int. J. Hydrogen Energy*, 38 (2013) 10896. (f) Q.R. Zheng, X.H. Wang, S. Gao, *Cryogenics*, 61 (2014) 143.

[16] M. Fujiwara, Y. Fujio, H. Sakurai, et al., *Chem. Eng. Process.*, 79 (2014) 1.

[17] (a) M. Hirscher, B. Panella, *Scr. Mater.*, 56 (2007) 809. (b) H. Furukawa, M.A. Miller, O.M. Yaghi, *J. Mater. Chem.*, 17 (2007) 3197. (c) H.W.Langmi, J.W. Ren, B. North, et al, *Electrochim. Acta*, 128 (2014) 368. (d) E.I. Volkova, A.V. Vakhrushey, M. Suyetin, *Int. J. Hydrogen Energy*, 39 (2014) 8347.

[18] H. Furukawa, O.M. Yaghi, *J. Am. Chem. Soc*, 131 (2009) 8875.

[19] R. Snurr, J. Hupp, M. Kanatzidis, et al., 'New-carbon based porous materials with increased heats of adsorption for hydrogen storage', Northwestern University, 2012. (Powerpoint file access: http://www.hydrogen.energy.gov/pdfs/review12/st023_snurr_2012_o.pdf)

[20] M.C. Tellez-Juarez; V. Fierro, W. Zhao, et al, *Int. J. Hydrogen Energy*, 39 (2014) 4996.

[21] S.K. Bhatia, A.L. Myers, *Langmuir*, 22 (2006) 1688.

[22] W.C. Conner., J.L. Falconer, *Chem. Rev*., 95 (1995) 759.

[23] (a) P. Jain, D. A. Fonseca, E. Schaible, et al, *J. Phys. Chem. C*, 111 (2007) 1788. (b) C.D. Wu, Q.M. Gao, J. Hu, et al., *Micropor. Mesopor. Mater*, 117 (2009) 165. (c) C. Zlotea, R. Campesi, F. Cuevas, et al, *J. Am. Chem. Soc.*, 132 (2010) 2991. (d) W. Zhao, V. Fierro, C. Zlotea, et al, *Int. J. Hydrogen Energy*, 37 (2012) 5072. (e) D. Giasafaki, G. Charalambopoulou, A. Bourlinos, et al, *Adsorption*, 19 (2013) 803.

[24] C. Estournès, T. Lutz, J. Happich, et al, *J. Magn. Magn. Mater.*, 173 (1997) 83.

[25] R. Takahashi, S. Sato, T. Sodesawa, et al., *Micropor. Mesopor. Mater.*, 66 (2003) 197.

[26] (a) S.S.A. Syed-Hassan, C.Z. Li, *Int. J. Chem. Kinet.*, 43 (2011) 667. (b) S.S.A. Syed-Hassan, C.Z. Li, *Appl. Catal., A*, 398 (2011) 187.

[27] K. Yamamoto, Y. Sunagawa, H. Takahashi, et al., *Chem. Commun.*, (2005) 348.

[28] J.S. Jung, W.S. Chae, R.A. McIntyre, et al., *Mater. Res. Bull.*, 34 (1999) 1353.

[29] (a) A.G. Boudjahem, S. Monteverdi, M. Mercy, et al., *J. Catal.*, 221 (2004) 325. (b) A.G. Boudjahem, S. Monteverdi, M. Mercy, et al., *Langmuir*, 20 *(*2004) 208.

[30] R. Wojcieszak, M. Zielinski, S. Monteverdi, et al, *J. Colloid Interface Sci.*, 299 (2006) 238.

[31] Y.P. Zhai, Y.Q. Dou, X.X. Liu, et al., *Carbon*, 49 (2011) 545.

[32] G.A.M. Hussein, A.K.H. Nohman, K.M.A. Attya, *J. Therm. Anal.*, 42 (1994) 1155.

[33] M.A.A. Elmasry, A. Gaber, E.M.H. Khater, *J. Therm. Anal.*, 47 (1996) 757.

[34] J.C. De Jesus, I. Gonzalez, A. Quevedo, et al., *J. Mol. Catal. A: Chem.*, 228 (2005) 283.

[35] M.A. Mohamed, S.A. Halawy, M.M. Ebrahim, *J. Anal. Appl. Pyrolysis* 27 (1993) 109.

[36] A.M. Gadalla, H.F. Yu, *Thermochim. Acta*, 164 (1990) 21.

[37] (a) R. Wojcieszak, Thesis: 'Study of supported nickel catalysts prepared by aqueous hydrazine method. Hydrogenating properties and hydrogen storage. Support effect. Silver additive effect.', Nancy, 2006. (b) Z. Libor, Q. Zhang, *Mater. Chem. Phys.*, 114 (2009) 902. (c) G.Y. Huang, S.M. Xu, G. Xu, et al., *Trans. Nonferrous Met. Soc. China* 19 (2009) 389.

[38] (a) Q. Jeangros, T.W. Hansen, J.B. Wagner, et al, *J. Mater. Sci.*, 48 (2013) 2893. (b) G. Parravano*, J. Am. Chem. Soc.*, 74 (1952) 1194. (c) T. Saarinen, S. Flugleberg, L.E. Lindfors, *Hydrometallurgy*, 43 (1996) 117.

[39] A. Weibel, R. Bouchet, F. Boulc'h, et al., *Chem. Mat.*, 17 (2005) 2378.

[40] Institute of Technical Physics and Materials Science (MFA) Tutorial website: http://alag3.mfa.kfki.hu/mfa/nyariiskola/10_Magneses_kepalkotas/

[41] Basic Electronics Tutorials (by Wayne Storr) website: http://www.electronics-tutorials.ws/electromagnetism/magnetic-hysteresis.html

[42] S.H. Wu, D.H. Chen, *J. Colloid Interface Sci.*, 259 (2003) 282.

[43] B.D. Cullity, C.D. Graham, *Introduction to magnetic materials*, Second Ed., John Wiley and Sons: Hoboken, (2009).

[44] J.H. Hwang, V.P. Dravid, M.H. Teng, et al, *J. Mater. Res*., 12 (1997) 1076.

[45] I.M.L. Billas, A. Châtelain, W.A. de Heer, *Science*, 265 (1994) 1682.

[46] I.S. Lee, N. Lee, J. Park, et al., *J. Am. Chem. Soc.*, 128 (2006) 10658.

[47] Olivier Margeat, Thesis: 'Effets de taille et de surface sur les propriétés physiques de nanoparticules superparamagnétiques', pp. 56–69, Université Paul Sabatier de Toulouse, 2005.

[48] B.I. Nandapure, S.B. Kondawar, M.Y. Salunkhe, et al., *Adv. Mat. Lett.*, 4 (2013) 134.

[49] B. Kisan, P.C. Shyni, S. Layek, et al., *IEEE Trans. Magn.*, 50 (2014)

[50] P.L. Llewellyn, G. Maurin, *C. R. Chim.*, 8 (2005) 283.

[51] C. Knöfel, Thesis: 'Synthesis, characterisation and evaluation of porous materials for the adsorption of carbon dioxide', Aix-Marseille Université, 2009, pp. 35–37.

[52] P. Holmqvist, P. Alexandridis, B. Lindman, *J. Phys. Chem. B*, 102 (1998) 1149.

[53] S. Brunauer, *The adsorption of gases and vapors: Physical adsorption*, Princeton University Press: Princeton, Vol. 1, (1945).

[54] M. Hirscher, *Handbook of Hydrogen Storage: New Materials for Future Energy Storage*, Wiley-VCH Verlag GmBH: Weinheim, (2010).

[55] B. Schmitz, U. Müller, N. Trukhan, M. Schubert, et al, *ChemPhysChem*, 9 (2008) 2181.

[56] M. Schlichtenmayer, M. Hirscher, *J. Mater. Chem*., 22 (2012) 10134.

General conclusions

General conclusions

The aim of this work was to study porous materials, combining a high specific surface area and a functionalization with metal nanoparticles for applications in the field of adsorption in liquid phase, specifically the detection of molecules at low concentrations using Raman spectroscopy, and in gas phase, specifically the hydrogen storage.

Prior to these respective studies, organized porous silicas and porous carbon were synthesized through the sol-gel method using block copolymers as structure directing agents. Materials were characterized using conventional techniques such as nitrogen adsorption/desorption measurements at 77°C and transmission electronic microscopy.

The first application was related to the detection of rhodamine 6G (R6G) molecules at low concentrations adsorbed on nanocomposites based on porous silica matrices in which Ag and Au nanoparticles were incorporated, namely Ag@SiO_2 and Au@SiO_2. The idea developed in this study was the coupling of the thermodynamics properties of R6G adsorption to its Raman response. Firstly, the post-synthesis functionalization of the silica matrices with metal nanoparticles was shown to be successful via reduction in gas phase. Secondly, the adsorption properties, both the construction of isotherms and the determination of adsorption enthalpies, were studied for initial concentrations of R6G ranging from $1\ 10^{-4}$ M to $1\ 10^{-7}$ M. Finally, the Raman response was determined at different points of isotherms.

A preliminary study was performed using SBA-16-based materials (pure SBA-16 matrix and Ag@SBA-16 with particles of 3 nm). It was shown that the pre-concentration properties of the porous silica matrix were sufficiently important to already detect R6G unambiguously without silver nanoparticles at an initial concentration close to $C_i = 5\ 10^{-6}$ M. Furthermore, at a concentration $C_i = 1\ 10^{-6}$ M, a chemical enhancement (CE) mechanism of SERS effect was evidenced with an exaltation factor of roughly 10 with the presence of silver nanoparticles. It was evidenced that the adsorption of R6G on silver nanoparticles was achieved through its ethylamine groups as shown by Raman bands exhibited and the high values of integral adsorption enthalpies.

Then, another silica matrix was used in order to tune easily the nanoparticle size (SEO matrix). It was shown that the type of silica, in terms of surface chemistry and pore size, does not affect the Raman response of adsorbed R6G. Ag and Au nanoparticles were incorporated in the SEO matrix, their mean diameter was found close 6 nm. It was shown that, for initial concentrations

$C_i > 1\ 10^{-6}$ M, the chemical nature of the metal did not affect the Raman response of R6G adsorbed on the nanocomposite substrates: the intensity of Raman bands is linearly correlated to the adsorbed amounts for silver and gold nanoparticles. At lower initial concentrations $C_i = 1\ 10^{-6}$ and $1\ 10^{-7}$ M, the Raman signal of R6G was studied on four different substrates: SEO, Au@SEO and Ag@SEO with a simple or double impregnation (DI). It was shown that the Raman signal of R6G was enhanced for both Ag@SEO solids and the enhancement was more pronounced for Ag@SEO-DI that contains the larger nanoparticles (15 nm). The enhancement factor was found close to 6 and it was possible to detect R6G molecules for very low adsorbed amounts ($N_{ads} = 0.002\ \mu mol.\ g^{-1}$). Finally, the influence of the excitation wavelength and the adsorbed molecule on detection properties was introduced. This last point had clearly emphasized that the detection performances were based on the synergy of experimental factors and features of materials.

In future work, the study of the adsorption properties and Raman response of other model molecules such as pure pyridine and amino/thiol modified pyridine will be performed in order to study the influence of interaction between the solid and the molecule to be detected. Other impregnation processes will also be tested to improve the adsorbed amounts on nanocomposites in order to increase the detection threshold and to work with initial concentration lower than $1\ 10^{-7}$ M. The study of the influence of nanoparticle size on the Raman response is also planned and the work concerning this part is in progress.

The second application was related to the storage of hydrogen in Ni-based nanocomposites, Ni@SiO_2 and Ni@Carbon. An important segment of this study was devoted to the preparation and characterization of nanocomposites. The first part consisted in the determination of experimental conditions for the effective reduction of nickel starting from thermally treated Ni acetate (at 200 or 400 °C). Two reduction processes were tested, one in the liquid phase involving hydrazine as reducing agent and one in gas phase involving hydrogen. In this way, it was shown that, starting from NiAc(200 °C), the reduction process was more efficient independently of the nature of the chemical procedure (liquid or gas phase) than in the case of NiAc(400 °C). Indeed, the reduction was complete in liquid phase and almost complete (77 wt% of Ni) in gas phase for NiAc(200 °C) while for NiAc(400 °C) nickel oxide is predominant (95 to 98 wt%) whatever the reduction process. The second part concerned the post-synthetic functionalization of silica and carbon matrices with nickel-based nanoparticles. In the case of silica, nickel-based nanoparticles with a diameter close to 7 nm were incorporated using reduction in gas phase. In the case of carbon matrices, two types of solids were used: a

commercial activated charcoal (Carbon Norit) and a laboratory-made carbon (Carbon). In this case, particles with diameter smaller than 3 nm in Ni@Carbon were incorporated using the reduction in liquid phase. Then, hydrogen adsorption properties at low temperature and pressure for the unconfined particles and the nanocomposite materials were studied. It was shown that, for unconfined nickel particles reduced in liquid phase, the enthalpies of adsorption were about $-20\ \mathrm{kJ.mol^{-1}}$ for commercial NiO nanoparticles and $-14\ \mathrm{kJ.mol^{-1}}$ for NiAc(400 °C) precursors. These values are closed to the one obtained for commercial Ni ($-17\ \mathrm{kJ.mol^{-1}}$), it thus clearly evidences the presence of Ni metallic surface. While for the unconfined nickel particles reduced in gas phase, the values were lower ($\sim 7-8\ \mathrm{kJ.mol^{-1}}$), indicating either the presence of pure NiO surface or a mixture of Ni/NiO at the surface.

For the nanocomposite Ni(200°C)@SiO_2 obtained from reduction in gas phase, the energies of interactions were seen to be low ($\sim -4\ \mathrm{kJ.mol^{-1}}$). Incorporated nanoparticles were thus in the Ni–NiO core–shell configuration. For the carbon material synthesized, the hydrogen adsorption properties were similar to those obtained in the literature. Studies of hydrogen adsorption properties on nanocomposites using both types of carbon matrices may present good hydrogen properties: high adsorbed amounts associated with high enthalpies of adsorption are expected.

Appendices

Experimentals methods

Table of contents

A. Chemicals

Chemicals were used as received without any further purification.

Solvents

sec-Butanol	$C_4H_{10}O$	Purity > 99%	Acrōs organics
Anhydrous absolute ethanol	C_2H_6O	Purity ≥ 99.9%	Carlo Erba
Distilled water	H_2O	Prepared-in-house	Elga PURELAB UHQ II, Water Purification System

Acids and bases

Hydrochloric acid	HCl	Solution of 35% in H_2O	VWR – BDH Prolabo
Sodium hydroxide	NaOH	Solution of 30% in H_2O	Fischer Chemical
Hydrazine hydrate	$N_2H_4{\cdot}H_2O$	Solution of 100% (64% N_2H_4)	Fischer Chemical

Structure directing agents

Triblock copolymer	Pluronic ® F-127	$PEO_{106}PPO_{70}PEO_{106}$	Powder	Sigma
Diblock copolymer		$PEO_{114}PS_{48}$	Powder	Laboratory-made ICR - CROPS team*

Precursors

Tetramethoxysilane	$SiC_4H_{12}O_4$	Solution – Purity ≥ 99%	Aldrich
Phenol	C_6H_6O	Crystal solids – Purity ~99%	Sigma-Aldrich
Formaldehyde	CH_2O	Solution of 36.5-38% in H_2O	Sigma
Silver (I) nitrate	$AgNO_3$	Solids – Purity ≥ 99.8%	Sigma-Aldrich
Gold (III) chloride hydrate	$HAuCl_4{\cdot}xH_2O$	Solids – Purity 99.999%	Aldrich
Nickel	Ni	Nanopowder – Purity 99,9%	Aldrich
Nickel (II) oxide	NiO	Nanopowder – Purity 99.8%	Aldrich
Nickel (II) acetate tetrahydrate	$C_4H_6NiO_4{\cdot}4H_2O$	Powder – Purity ≥ 99%	Aldrich

Dyes

Rhodamine 6G	$C_{28}H_{30}N_2O_3{\cdot}HCl$	λ_{max} ~530 nm	Powder	Sigma
Methylene blue	$C_{16}H_{18}ClN_3S{\cdot}3H_2O$	λ_{max} ~665 nm	Powder	Fischer Chemical

Porous materials

Activated Charcoal Norit ®	Norit RB3	C	Rods	Sigma-Aldrich – Fluka

(The carbon rods were ground within this work)

Gases

Argon/Hydrogen	Ar/H_2	Molar ratio 95/5	ALPHAGAZ ™	Air Liquide

* ICR: Institut de Chimie Radicalaire, Equipe CROPS (Chimie Radicalaire Organique et Polymères de Spécialité)

B. Textural and structural characterization

B.1. Thermogravimetric analysis (TGA)

The thermal gravimetry allows one measuring the weight loss/gain of a sample as a function of the temperature under different possible oxidizing (air, oxygen) or inert (argon, nitrogen, etc.) atmospheres. An overall view of the thermal stability of a material is then obtained.

The TGA measurements were carried out with a TGA Q500 apparatus (TA Instruments) at Laboratoire Matériaux Divisés, Interfaces, Réactivité, Électrochimie (MADIREL), Marseille. Experiments were performed under dynamic air or inert (Ar or N_2) atmosphere (sample flow rate $60\ \text{mL.min}^{-1}$). The samples (minimum $\sim$15 mg) were thermally treated in a platinum crucible, using most of the time a high resolution setting with a heating rate of 5 or $10°\text{C.min}^{-1.}$ This setting helps defining more precisely the different phenomena occurring during the thermal treatment by reducing the heating rate once a significant change in mass is observed and then allow these phenomena to occur close to thermodynamic equilibrium conditions. The data processing was performed with the TA Universal Analysis software.

This technique was used for various purposes in this work: (i) to determine the degradation temperature of the surfactant template in the as-synthesized matrices of silica and carbon and then establish a calcination route for obtaining the mesoporous silicas SBA16 and SEO and carbon materials, (ii) to estimate the degradation temperature of the synthesized porous silica and carbon matrices and (iii) to investigate the decomposition of the nickel precursor (acetate) bulk and then establish calcination routes for the nickel impregnated samples.

B.2. Powder X-ray diffraction (PXRD) analysis

Powder X-ray diffraction is a widely used technique in material science to obtain information about the crystal structure, crystallinity, organization of solid materials. As the name suggests, the sample is in a powdery form consisting of fine grains (single crystallites): it is a polycrystalline powder. The diffraction pattern presents the X-ray diffraction peaks whose positions and intensities are characteristic of crystallographic structure of chemical elements in the solid sample. Therefore, this technique provides information about the crystal structure and the phase composition of the powder material. Furthermore, the peak broadening can be used in the Scherrer equation† to calculate the crystallite size of the sample.

† Scherrer equation: $\mathbf{t = (0.9 \times \lambda)/(\beta \times \cos \theta_\beta)}$ with t crystallite size, λ wavelength of the X-ray source ($\lambda = 1.54056$ Å), β integral breadth of the diffraction peak corresponding to the Bragg angle θ_β.

XRD patterns were recorded with a Siemens D5000 XRD Diffractometer by Carine Chassigneux at Laboratoire Matériaux Divisés, Interfaces, Réactivité, Électrochimie (MADIREL), Marseille. The apparatus possess a Cu $K_{\alpha 1}$ radiation ($\lambda = 1.54056$ Å) and a Bragg-Brentano geometry, using $\theta - 2\theta$ configuration (the X-ray source is fix and the sample and the detector are mobile). The intensity was taken in steps of 0.04° and associated with a step time of 8 seconds. The samples (~200 mg) were ground prior to analysis. Diffract Plus EVA software was used to study the diffraction patterns in concordance with the Joint Committee for Powder Diffraction Studies (JCPDS) cards from the data base.

The mesoporous silica SBA-16 prepared within this work is amorphous, so no reflection should be observed in wide-angle XRD patterns of this material, only a rough background may appear. The crystal structure of pure nickel and nickel oxide nanoparticles were evidenced in order to be used as references for analyzing the nickel-based unconfined particles as well as the nanocomposite samples and completing data for the study of hydrogen adsorption using microcalorimetry.

B.3. Transmission electron microscopy (TEM)

The transmission electron microscopy is a useful technique in physical characterization of solid materials. Two operating modes are available: the *imaging mode* (2D imaging) to get information about the shape and size of nanoobjects and the *diffraction mode* to define the crystallographic structure (lattice system and unit cell parameters). This method can be combined with energy dispersive X-ray spectroscopy (EDS) (microanalysis of characteristic X-rays) that provides identification and quantification of elements.

TEM micrographs were taken with a JEOL JEM 2010F transmission electron microscope (operating at an acceleration voltage of 200 kV) by Martiane Cabié at Centre Pluridisciplinaire de Microscopie électronique et de Microanalyse (CP2M), Marseille. The samples ($\sim 10 - 15$ mg) were ground and afterwards dispersed in methanol. The suspension was dropped onto a carbon film-coated copper grid and dried in air.

Within this work, the image mode was applied and the TEM images were used: (i) to determine the organization of the porous structures and to confirm the pore size distribution of the silica and carbon samples, (ii) to verify the incorporation of nanoparticles in the porosity of the latter and evaluate their size and (iii) to estimate the crystallite size of the reference materials (commercial Ni and NiO nanoparticles).

B.4. Scanning electron microscopy (SEM)

The scanning electron microscopy is also a useful technique in physical characterization of solid materials. The *imaging mode* allows getting information about not only the shape and size of nanoobjects but also information about their surface. Very high-resolution images can be obtained showing clearly the surface topography (3D imaging) and chemical composition homogeneity (contrast imaging). Besides, as its counterpart transmission electron microscopy, an integrated energy dispersive X-ray micro-analysis (EDS) system provides complementary qualitative and quantitative compositional analysis. Samples can be observed in high vacuum, in low vacuum, in wet conditions (in environmental SEM – ESEM), and at a wide range of cryogenic or elevated temperatures.

SEM micrographs were taken with a FEI Philips XL-30 ESEM (operating at an acceleration voltage of $15 - 20$ kV) by Alain Tonetto at Plateforme de recherche analytique, technologique et imagerie (PRATIM), Fédération des Sciences Chimiques de Marseille, Marseille. The samples ($\sim$100 mg) were ground and afterwards dispersed onto an adhesive surface placed on the sample holder. Before analysis, the samples were coated with an ultrathin layer of gold in order to allow conductivity of the samples and then preventing surface charging effect (due to hindering of the electrons expulsion).

Within this work, the SEM images were used to estimate the crystallite size and morphology of the unconfined nickel-based particles synthesized.

B.5. Inductively coupled plasma-mass spectrometry (ICP-MS)

The inductively coupled plasma-mass spectrometry is an analytical technique used for elemental chemical characterization. A unique capability of ICP-MS is its ability to measure the concentration of specific analyte isotopes. It allows both single and multi-element isotope dilution measurements to be performed on a single sample aliquot (portion of a total amount of a solution). The high sensitivity of the technique, coupled with multi-element detection capability, allows a wide scope of qualitative, semi-quantitative, and quantitative determinations to be achieved over a large dynamic concentration range (minor to ultratrace concentration levels). [1] This technique combines a high-temperature gas plasma (generally inert gas – especially argon since it has the advantageous property of having a minimal reactivity with various species) as an ionization source for the atoms of any elements in the sample and a mass spectrometer with ion detector to separate and determine the different elements by measuring the mass-to-charge ratio of the charged particles.

The ICP-MS measurements were carried out using a Thermo X series II model by Florence Chaspoul at Institut Méditerranéen de Biodiversité et d'Écologie marine et continentale (IMBE), Marseille. Prior to analysis, the samples (~10 mg) were soaked, during 24 h, in a solution containing 2 mL of concentrated nitric acid (HNO_3) and 1 mL of concentrated HCl. Then 3 mL of distilled water was added and the whole solution was subjected to ultrasound for several minutes. The plasma gas used within this work was argon.

Within this work, this technique was used for determining the exact amount of metal (silver and gold) particles that were incorporated in the porous silica matrices. For the different carbon-based nanocomposites, the analysis was hardly feasible since carbon is difficult to dissolved, even in HNO_3.

B.6. Low temperature nitrogen sorption analysis

Nitrogen adsorption/desorption at 77 K is a standard method for characterizing porous materials. Indeed, it permits estimating the specific surface area, the pore size and the pore volume of the solids from the adsorption/desorption isotherms obtained.

The experiments were performed, with an ASAP 2010 apparatus (Micromeritics Instrument) at liquid N_2 temperature (77 K) at Laboratoire Matériaux Divisés, Interfaces, Réactivité, Électrochimie (MADIREL), Marseille. Prior to adsorption, the samples ($\sim 50 - 100$ mg) were degassed for several hours (16 h) under vacuum ($2\ 10^{-3}$ mbar) and heated to 120°C for the removal of all physisorbed species. The weight of samples was determined before and after activation.

The Brunauer–Emmett–Teller (BET) surface areas were obtained with the BET treatment of the isotherms in a relative pressure ($p/p°$) range of $0.05 - 0.35$ for micro-/mesoporous silica-based materials and in a range of 0.0001– 0.1 for microporous carbon-based materials. The average pore sizes were calculated on the basis of the adsorption branch of the isotherms using the Barrett–Joyner–Halenda (BJH) model. The pore volumes were measured with the *t*-plot method. All these calculation methods are developed in the followings.

B.6.1. Phenomenon of adsorption

Adsorption is a phenomenon that occurs when a fluid (gas or liquid solute), the *adsorptive*, accumulates on the surface of a solid or more rarely liquid, the *adsorbent*, forming a molecular or atomic film so-called the *adsorbate*. This process is actually a consequence of the difference of surface energy that is experienced by the surface atoms of the adsorbent. This phenomenon should not be confused with *absorption* by which the fluid penetrates the solid itself through a

diffusion mechanism. The term *sorption* is used in borderline cases where the above distinctions cannot be made. The amount of adsorbate depends on the temperature, the pressure and the interactions between the adsorptive and the adsorbent. The reverse process is defined as *desorption*.

Two types of adsorption can be distinguished: *physisorption* (physical adsorption) and *chemisorption* (chemical adsorption). Contrary to chemisorption where transfer or sharing of electrons occurs, in physisorption only van der Waals bonds are created between the adsorbate and the adsorbent. Consequently, after desorption, the previously physisorbed molecules are chemically unchanged and the adsorbent surface is not modified: the process is reversible. Chemisorption is usually not reversible, but if desorption occurs, the desorbed molecules may be different from the initial solute.

During the phenomenon of adsorption, there is a concentration gradient of the fluid (gas or liquid) between the adsorbent surface and the adsorptive bulk fluid, as schematized in **Figure B.1 (a)**. Indeed, without any information about the adsorbed phase, the local concentration ($c = dn/dV$) can be arbitrarily assumed to decrease gradually with increasing distance (z) from the adsorbent surface up to reach the bulk fluid phase concentration (c^f) at a certain distance (r), at which the influence of the adsorbent is no longer felt. This region between the adsorbent surface and the adsorptive bulk fluid delimits an adsorbed layer defined as the *amount adsorbed* (n^a).

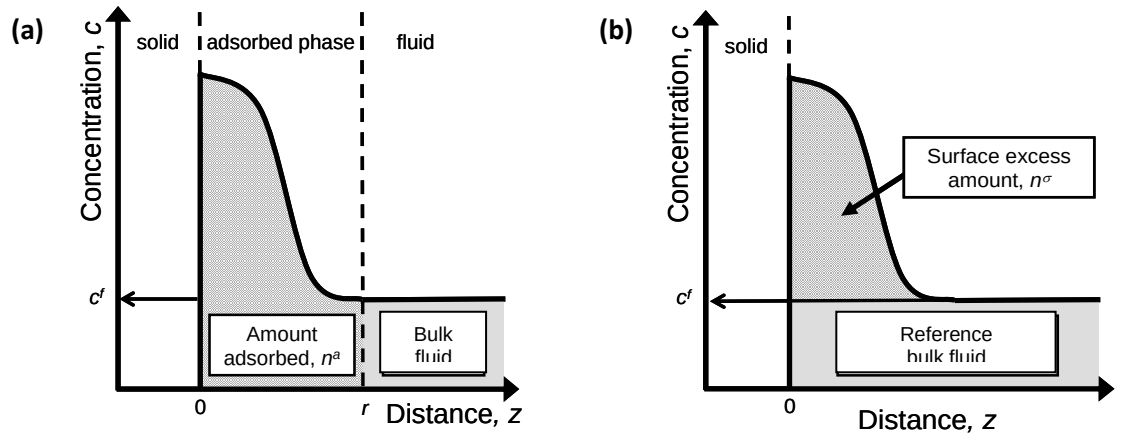

Figure B.1: Schematic representations of the phenomenon of adsorption using the Layer model (a) and the Gibbs representation (b). Adapted from [2].

Using this representation, known as the *Layer model*, this adsorbed amount corresponds to the hatched area:

Equation B.1

$$\mathbf{n^a = A \int_0^r c\, dz}$$

Where: A is the area of the interface on which adsorption can occur

The quantity is generally referred to as *absolute (or total) amount adsorbed* (n^a) and can be expressed as:

Equation B.2 $$\mathbf{n^a = n - c^f \times V^f}$$

Where: n is the total amount of adsorptive fluid in the system

c^f is the adsorptive fluid concentration when adsorption equilibrium is reached (bulk fluid concentration)

V^f is the volume occupied by the adsorptive fluid when adsorption equilibrium is reached (bulk fluid volume)

Thus, the term $c^f \times V^f$ represents the residual adsorptive fluid which is the amount of fluid in the system which is not adsorbed (bulk fluid region). The absolute amount adsorbed is thus the difference between the total amount of fluid in the system and the amount remaining at the bulk concentration. However, in practice, the concentration profile of the fluid or the volume of the fluid at the bulk concentration V^f are parameters difficult to assess.

In 1877, in order to overcome this problem, Gibbs proposed a second representation of the adsorption system: the *Gibbs representation* [2], schematized in **Figure B.1 (b)**. In this representation, the concept of *excess amount adsorbed* or *surface excess amount* (n^σ) is used to describe the amount of fluid near (and often considered 'on') the adsorbent surface at a concentration above that of the bulk fluid phase (c^f). Such representation describes the adsorption system as compared to a reference state in which adsorption does not occur on the surface. The surface excess amount can be expressed as:

Equation B.3 $$\mathbf{n^\sigma = n - c^f \times V^{f,0}}$$

Where: $V^{f,0}$ is the volume of the reference state

The volume of the reference state includes the volumes of the adsorbed phase (V^a) and of the remaining bulk fluid (V^f) respectively, **Equation B.4**. Therefore, the surface excess amount can be expressed as a function of the latter, **Equation B.5**.

Equation B.4 $$\mathbf{V^{f,0} = V^a + V^f}$$

Equation B.5 $$\mathbf{n^\sigma = n - c^f \times V^a - c^f \times V^f}$$

A relationship between the absolute amount adsorbed and the surface excess amount can be then derived:

Equation B.6 $$\mathbf{n^a = n^\sigma + c^f \times V^a}$$

In adsorption experiments, it is usual to measure surface excess amounts. The volume $V^{f,0}$ can be determined relatively easily either from knowledge of the total free volume of the cell and he volume of the adsorbent or from experiments involving an inert gas (such as helium) which is considered not to adsorb.

In cases where the amounts adsorbed are substantial and/or where the experiment does not go to high pressure, $c^f \times V^a$ is negligible as compared to n^σ and it can be assumed: $n^a \approx n^\sigma$. This is notably the case for the adsorption of nitrogen at 77 K (which is often used for the characterization of porous solids) or of most gases at room temperature up to atmospheric pressure. However, in many cases, at higher temperatures and in particular at high equilibrium pressures, the term $c^f \times V^a$ is no more negligible and it is important to estimate the volume of the adsorbed phase.

In the case of highly porous materials, the volume where adsorption can occur (V^a) can be approximated to the total porous volume (V^p) [3] by considering that the amount adsorbed on the external surface is negligible as compared to that adsorbed in the pores:

Equation B.7 $$\mathbf{n^a = n^\sigma + c^f \times V^p}$$

In practice, in gas adsorption (desorption) measurements, the amount adsorbed (n^a) is given per gram of adsorbent for each equilibrium pressure. The representation of the gas – solid equilibrium as a function of the pressure (p) and temperature (T) of the system is called an *adsorption/desorption isotherm*, **Equation B.8**. The pressure can be given in function of the saturation vapour pressure at the temperature of adsorption $p°$ (which is measured separately). The temperature is generally kept constant during experiments.

Equation B.8 $$\mathbf{n^a/m^s = f\,(p)_T}$$

Where*:* m^s is the mass of the adsorbent

B.6.2. Determination of the adsorption/desorption isotherm in gas phase

Equilibrium gas adsorption measurements can be carried out using different methodologies. The most common methods employed are the manometric or volumetric method and the gravimetric method. A simple representation of a manometric device is given in **Figure B.2**.

The adsorption measurements consist of dosing a known amount of adsorptive gas into a reference volume (V_{ref}) and the temperature and pressure are recorded. The reference volume is then opened to the sample volume (V_{sample}) and the system is followed until equilibrium between the sample and the gas is reached.

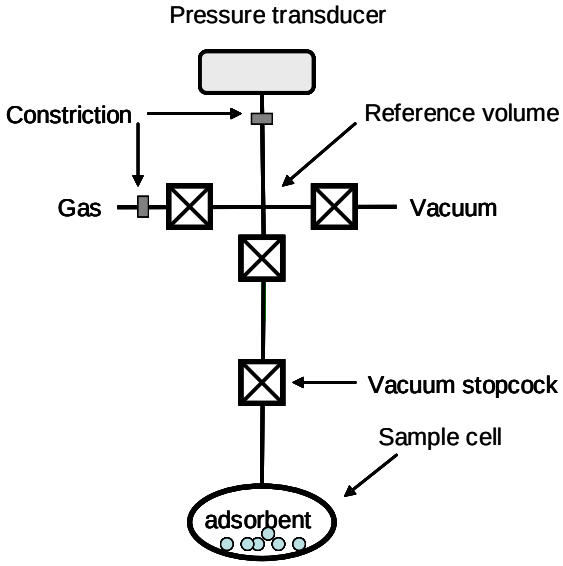

Figure B.2: Schematic representation of a manometric device to measure adsorption isotherms. Adapted from [2].

For each adsorption dose, the amount of gas in the reference volume and sample volume is calculated. This amount can be calculated using the simple ideal gas law ($p \times V = n \times R \times T$) or by a more complicated expression if gas non-ideality has to be taken into account. Using the ideal gas law, the initial amount of gas in the system (n^i) before the adsorption dose is thus:

Equation B.9

$$\mathbf{n^i = n^i_{V_{ref}} + n^i_{V_{sample}} = \frac{p^i_{ref} \times V_{ref}}{R \times T_{ref}} + \frac{p^i_{sample} \times V_{sample}}{R \times T_{sample}}}$$

Where:

$n^i_{V_{ref}}$	is the initial amount of gas in the reference volume	
$n^i_{V_{sample}}$	is the initial amount of gas in the sample volume	
p^i_{ref}	is the pressure in the reference volume	
p^i_{sample}	is the pressure in the sample volume	
R	is the ideal gas constant	$(R = 8.314\ J.mol^{-1}.K^{-1})$

Note that for the initial dose, the initial pressure p^i_{sample} is zero if the sample is degassed under vacuum. The temperatures of the sample volume T_{sample} and reference volume T_{ref} should be taken into account. The gradient in temperature between the sample and reference volumes can also be taken into account.

A similar expression is used to calculate the final amount of gas phase (n^f) after adsorption equilibrium:

Equation B.10
$$\mathbf{n^f = n^f_{V_{ref}} + n^f_{V_{sample}} = \frac{p^f \times V_{ref}}{R \times T_{ref}} + \frac{p^f \times V_{sample}}{R \times T_{sample}}}$$

It should be mentioned that since the reference and sample volumes are in communication, the measured final pressure is the same in each term: $p^f_{ref} = p^f_{sample} = p^f$.

Besides, for following doses:

Equation B.11
$$\mathbf{\frac{p^f \times V_{sample}}{R \times T_{sample}} = \frac{p^{i+1}_{sample} \times V_{sample}}{R \times T_{sample}}}$$

Therefore, the amount adsorbed per dose can be calculated:

Equation B.12
$$\mathbf{n^a = n^i - n^f}$$

As mentioned in the previous sub-section, the gas–solid equilibrium states are presented as the amount of condensed molecules of the analysis gas (n^a) by unit mass of solid (m^s) as a function of the relative pressure $p/p°$ at a constant temperature T, as expressed in **Equation B.13** (based on **Equation B.8**). More generally, the amount adsorbed can be expressed in volume adsorbed [$cm^3.g^{-1}$].

Equation B.13
$$\mathbf{n^a/m^s = f\,(p/p°)}$$

B.6.3. Adsorption isotherm classification

According to the International Union of Pure and Applied Chemistry (IUPAC) recommendation [4], six main types of gas physisorption isotherm can be defined as shown on **Figure B.3 (a)**. Types *I* to *V* were originally proposed by S. Brunauer, L.S. Deming, W.E. Deming and E. Teller in a first classification [5]. Besides, four main types (*H1* to *H4*) of hysteresis loop have been classified [2], as shown on **Figure B.3 (b)**.

Prior to describe the different types of isotherm, a brief recall on the different types of pores should be given. According to the IUPAC recommendation [6], porous materials can be classified into three groups depending on the size of their pores: microporous (pore size smaller than 2 nm), mesoporous (pore size ranging from 2 to 50 nm) and macroporous (pore size larger than 50 nm) materials. It can also be distinguished two types of micropores [7] considering the ratio between their width w and the probe molecule diameter d (e.g. nitrogen) taken as reference:

ultramicropores (w/d lower than 3) and supermicropores (w/d equal or higher than 3). In parallel to this classification, the term 'nanopore' is increasingly used for pores smaller than 100 nm.

The shape of the isotherms is characteristic of the type of porosity (micro-, meso- or macroporosity) of the materials, and the hysteresis loop gives information about the pore shape (tubular, wormlike, ink-bottle, etc.) of the materials. Besides, the shape of the isotherms is closely related to the different adsorption phenomena involved (as described in the followings): in micropores, pore filling occurs at very low pressures while in the case of mesopores, capillary condensation is observed at higher relative pressures.

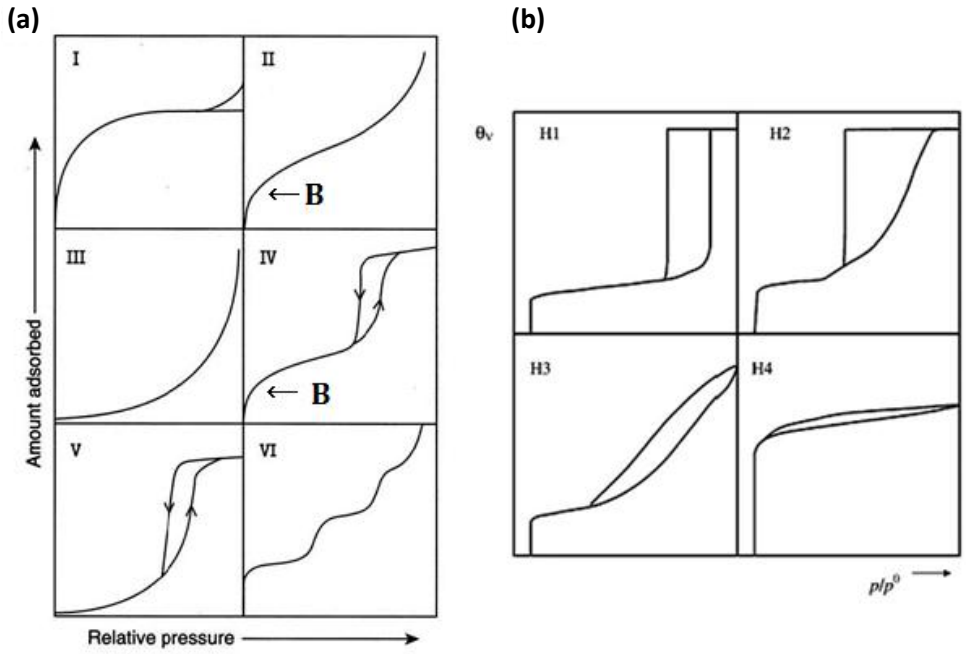

Figure B.3: IUPAC classification of adsorption isotherms [4] (a) and Modern classification of hysteresis loops [2] (b).

The isotherm of type *I* is characterized by a sharp increase of the amount adsorbed at very low relative pressures and then a long plateau over a wide range – representative of saturation of the adsorbent (all pores are filled). It is characteristic of microporous materials and the lower the pores size, the lower relative pressure at which they are filled.

The isotherm of type *II* is represented by a progressive increase of the quantity adsorbed as a function of the relative pressure. It is characteristic of non-porous or macroporous adsorbents (to a limited extent microporous) in which an unrestricted multilayer adsorption on an open and stable surface occurs. The point *B*, arrowed on the **Figure B.3 (a)**, means that the monolayer coverage is complete.

The isotherm of type *IV* is similar to the isotherm of type *II* at the lower relative pressures (in the case of nitrogen adsorption at 77 K, $p/p^0 \leq 0.42$). At higher relative pressures, it is characterized by a steep slope then a plateau of variable size (can be only an induction point): it indicates capillary condensation occurring in the pores of mesoporous materials. Moreover, desorption of nitrogen that has condensed by capillarity is not reversible: it yields in a hysteresis loop between the adsorption and desorption branches of the isotherm.

The isotherms of types *III* and *V* are rarely encountered. They differ from the isotherms of types *II* and *IV* at the lower relative pressures: they are convex instead of concave to the p/p° axis. The absence of the point *B* is interpreted as stronger adsorbate-adsorbate interactions than adsorbate-adsorbent interactions. The materials exhibiting isotherm of type *III* are non-porous while the ones exhibiting isotherm of type *V* are mesoporous; both have weak interactions with the adsorptive which is typical of non-wetting materials.

The isotherm of type *VI* presents several steps. It has been observed for adsorption on relatively energetically homogeneous surface: a step-wise layer-by-layer adsorption process occurs. It is typical of highly ordered uniform surface such as graphite. This type of isotherm is also rarely encountered.

Nota Bene: It should be highlighted that this classification has been created by studying known adsorbents. In practice, gas physisorption isotherms may consist of a mixing of two or more types of isotherm revealing more complex materials.

The hysteresis loop of type *H1* is symmetrical with nearly parallel adsorption and desorption branches. It is characteristic of adsorbents with a narrow distribution of uniform pores and often found in cylindrical pore systems.

The hysteresis loop of type *H2* is asymmetrical, forming a triangular shape with a long and almost flat plateau then steep desorption branch. It is characteristic of adsorbents with pores of tubular or ink-bottle shape with different sizes.

It is generally believed that the shape of the adsorption branch of the hysteresis loop is related to the absence or presence of pore network connectivity and pore blocking effect in the mesoporous materials. Type H_1 hysteresis loop is usually assigned to a mesoporous material made up of unconnected pores, whereas type *H2* hysteresis loop is expected for mesoporous materials with a connected pore structure. [8]

The hysteresis loops of type *H3* and *H4* do not terminate by a plateau at high relative pressures and the limiting desorption boundary curve is therefore more difficult to establish. Their loops

do not close until the equilibrium pressure is at or very close to the saturation vapor pressure. Type *H3* loops are given by the aggregates of platy particles or adsorbents containing slit-shaped pores. Type *H4* is also given by slit-shaped pores but the pore size distribution is mainly in the micropore range.

B.6.4. Brunauer–Emmett–Teller (BET) method

The BET theory [2] is a well-known rule for the physical adsorption of gas molecules on a solid surface. The concept of this theory is an extension of the Langmuir monolayer molecular adsorption to multilayer adsorption with the following hypotheses: (i) gas molecules physically adsorb on a solid in layers infinitely, (ii) there is no interaction between each adsorption layer and (iii) the Langmuir theory can be applied to each layer. Estimating the monolayer capacity of an adsorbent (i.e. the quantity of adsorptive that can be accommodated as a monolayer on the surface of the adsorbent) and the area of the adsorptive molecule, the surface area can, in principle, be calculated. The resulting BET equation in its linear form is expressed in the following equations:

Equation B.14

$$\frac{\boldsymbol{p/p^\circ}}{\boldsymbol{V\times(1-p/p^\circ)}} = \frac{\mathbf{1}}{\boldsymbol{V_m\times C}} + \frac{\boldsymbol{C-1}}{\boldsymbol{V_m\times C}} \times \frac{\mathbf{p}}{\boldsymbol{p^\circ}}$$

Equation B.15

$$\frac{\boldsymbol{p/p^\circ}}{\boldsymbol{n^a\times(1-p/p^\circ)}} = \frac{\mathbf{1}}{\boldsymbol{n_m^a\times C}} + \frac{\boldsymbol{C-1}}{\boldsymbol{n_m^a\times C}} \times \frac{\mathbf{p}}{\boldsymbol{p^\circ}}$$

Where:	V	is the volume of gas adsorbed at p/p°	$[cm^3.g^{-1}]$
	V_m	is the volume of the monolayer	$[cm^3.g^{-1}]$
	n^a	is the amount adsorbed at p/p°	$[mol.g^{-1}]$
	n_m^a	is the amount adsorbed of the monolayer	$[mol.g^{-1}]$
	C	is the BET constant	
	p/p°	is the relative pressure at temperature of adsorption	

The BET constant C is an energetic constant which relates the difference of adsorption energy between the formation of the first layer and the subsequent ones.

By plotting the above linear relationship restricted to a limited region of the adsorption isotherm, generally $0.05 < p/p^\circ < 0.35$, the volume or the capacity of the monolayer (V_m or n_m^a respectively) and the BET constant C can be calculated from the slope s and y-intercept i of the curve, as expressed in **Equation B.16** and **Equation B.17**. The calculation method is so-called the multipoint BET method.

Equation B.16
$$\boldsymbol{n_m^a = \frac{1}{s+i}}$$

Equation B.17
$$\boldsymbol{C = \frac{s}{i} + 1}$$

In addition, the relative pressure corresponding to the formation of the monolayer is given by:

Equation B.18
$$\boldsymbol{\frac{p}{p^\circ} = \frac{1}{\sqrt{C}+1}}$$

Then, using the value of V_m or n_m^a, the specific surface area S_{BET} (surface area A by unit mass of adsorbent m^s) can be calculated with the equation:

Equation B.19
$$\boldsymbol{S_{BET} = \frac{A}{m^s} = \frac{V_m \times N_A \times \sigma}{V_M \times m^s} = \frac{n_m^a \times N_A \times \sigma}{m^s}}$$

Where: N_A is the Avogadro's number $N_A = 6.022\ 10^{23}\ molecule.mol^{-1}$

σ is the adsorbate cross section (for N_2 at 77 K: $\sigma = 16.2$ Å^2)

V_M is the molar volume of the liquid adsorptive $[cm^3.g^{-1}]$

Besides, though numerous materials give linear BET plots in the range $0.05 < p/p^\circ < 0.35$, it is worth noting that in the case of microporous materials the linear region tends to be at lower relative pressures. Therefore, some criteria were proposed in order to determine and validate the pressure range used for the evaluation of the BET surface area:

- The BET equation is limited to the range of pressures where $n^a \times (1 - p/p^\circ)$ increases as a function of p/p°.
- The constant C is exponentially related to the adsorption energy, therefore C is necessarily positive. If a negative value for C is obtained, this indicates that the selected region is outside the valid range of the BET equation.
- The value of the relative pressure corresponding to the formation of the monolayer, given by **Equation B.18**, should fall in the pressure range used to evaluate the surface area.

B.6.5. Barrett–Joyner–Halenda (BJH) method

In a tube, when a gas is condensed at a pressure p lower than its saturation vapor pressure p°, the wall-liquid contact angle ϕ tends to be lower than 90 °: a meniscus can be observed while the liquid is in presence of its vapor, as exemplified in **Figure B.4**. This phenomenon is known as capillary condensation.

The BJH method [9] is based on a model for capillary condensation and evaporation. It is assumed that the relative pressure where the pore condensation occurs depends on the pore radius. The Kelvin equation provides a correlation between meniscus radius and pore condensation pressure. It quantifies the deviation in equilibrium vapor pressure above a curved surface from that above a plane surface at the same temperature. In other words, it gives a basic relationship between curvature and thermodynamic activity of a liquid film. An adequate analytical equation for the statistical film thickness of the adsorbate is also used, see next section.

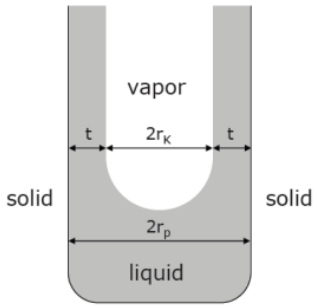

Figure B.4: Schematic representation of a capillary condensation in a tube.

The model is only valid for a limited number of geometries and is a function of the shape of the pore. The Kelvin equation assumes cylindrical mesopores:

Equation B.20

$$\mathbf{r_k = \frac{-2 \times \gamma \times V_M}{R \times T \times \ln(p/p^\circ)}}$$

Where:

r_k	is the Kelvin radius of the pore in which condensation occurs	[Å]
γ	is the surface tension of liquid adsorptive at its boiling point	
V_M	is the molar volume of liquid adsorptive	
R	is the ideal gas constant	$(R = 8.314\ J.mol^{-1}.K^{-1})$
T	is the boiling point of liquid adsorptive	(for N_2, $T = 77\ K$)
p/p°	is the relative pressure	

This equation can be simplified and is given in the following equation:

Equation B.21

$$\mathbf{r_k = \frac{4.15}{\log(p/p^\circ)}}$$

The BJH model correlates the Kelvin radius r_k to pore radius r_p according to the equation:

Equation B.22

$$\mathbf{d_{pore} = 2 \times r_p}$$

Equation B.23

$$\mathbf{r_p = r_K + t}$$

Where:	d_{pore}	is the pore size (pore diameter)	[Å]
	r_p	is the radius of the pore	[Å]
	t	is the thickness of the adsorbed layer	[Å]

The BJH method allows determining the pore size distribution of porous materials.

B.6.6. de Boer method (*t*–plot)

The de Boer method, commonly known as *t*-plot method, developed by de Boer [10], is based on the assumption that the thickness of the absorbed film on pore walls is uniform leading to a so-called statistical thickness t. This theoretical approach gives a direct relationship between the statistical thickness of adsorbed film and the experimental isotherm. The latter can be transformed into a *t*-plot that represents the volume of gas adsorbed in function of the statistical thickness at the corresponding $p/p°$ values. **Figure B.5** presents the *t*-plots of a non-porous system and a system that possesses micropores.

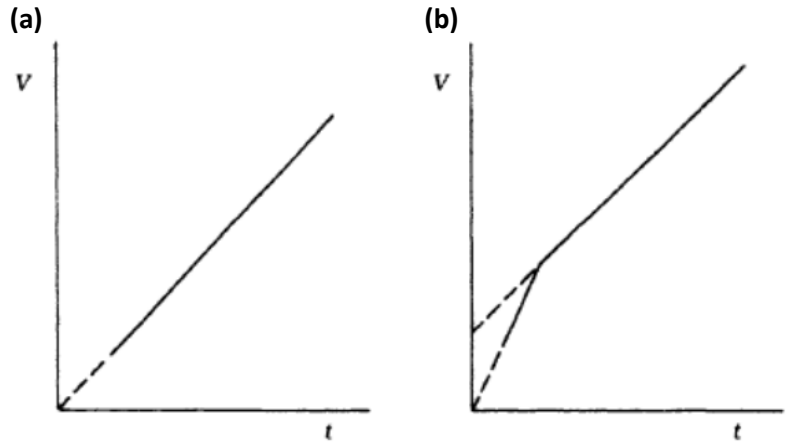

Figure B.5: *t*-plots of a non porous surface (a) and a surface with micropores first filled (b).

For non-porous surfaces, a *t*-plot is a straight line that passes through the origin (**Figure B.5 (a)**). For porous materials, the standard *t*-curve reveals a non-linear region at low pressures and results in a y-intercept different of zero which can be used to obtain information about the micropore volume (**Figure B.5 (b)**). Upward departures from linearity in the multilayer range are interpreted as caused by capillary condensation occurring in the mesopores and the total pore volume can be derived from the extrapolation of the saturation plateau (not shown on **Figure B.5**). Consequently, the volume of micropores and the total pore volume can be estimated and used to calculate the volume of mesopores in the studied system.

C. UV-visible spectroscopy in liquid and solid phase

UV-visible spectroscopy is an analytical technique based on the absorption of the light in the ultraviolet and visible spectral ranges. It allows measuring the absorbance of the samples in transmission or by reflectance as a function of the wavelength. The analysis can be performed in liquid or solid phase and permits qualitative and/or quantitative determination of the analytes.

UV-vis spectra were recorded on a Varian Cary 300 spectrometer at Laboratoire Matériaux Divisés, Interfaces, Réactivité, Électrochimie (MADIREL), Marseille. Measurements in liquid phase were performed in the range of $\lambda = 200 - 800$ nm. Measurements in solid phase were performed in the range of $\lambda = 300 - 800$ nm using an integrating sphere DRA-CA-30I and the solid were ground prior to analysis.

Within this work, this technique was used to: (i) determined the position of the plasmon resonance band of the solid nanocomposite samples Ag@Silica and Au@Silica (the background of the pristine porous silica matrix was subtracted for all of the spectra), (ii) to determine the adsorption properties of the solid substrates (pristine and nanocomposites) towards rhodamine 6G (R6G) and methylene blue (MB) and (iii) to determine the amount of nickel acetate adsorbed in the pristine porous Carbon Norit matrix.

The range of nanocomposite plasmon band gives complementary information about the presence of isolated metallic Ag and Au nanoparticles confined in porous silica host in accordance with the literature.

The study of R6G and MB adsorption properties consist of the study of their adsorption isotherms with respect to the different substrates. Adsorption isotherms represent the excess adsorbed amount versus equilibrium concentration (cf. *Section II.3.1.a.*). Prior to the construction of these isotherms, calibration curves of R6G in ethanol and MB in water were established at their maximum of absorbance band ($\lambda = 531$ nm and $\lambda_{max} = 665$ nm respectively) using the Beer-Lambert law, with reference solutions of known concentration. For all substrate, the isotherm construction was based on the depletion method: (i) 30 mg of solids were immersed into 2 mL of solution of concentration C_i and agitating at 25°C for 24 h to ensure that thermodynamic equilibrium is reached, (ii) after collection of the supernatants by centrifugation, the equilibrium concentrations were determined using the respective calibration curves at their respective maximum of absorbance band, (iii) the corresponding amounts adsorbed on the surface of the different substrates after impregnation were derived knowing the concentration variation (initial/equilibrium) of the supernatants and the solid/liquid (mass/volume) ratio used for the impregnation step (cf. *Section II.3.1.a.* **Equation 2.2**).

The amount of nickel acetate adsorbed in the pristine Carbon Norit matrix was determined similarly at its maximum of absorbance band ($\lambda = 395$ nm) using the depletion method.

D. Adsorption microcalorimetry in liquid phase [11]

The adsorption microcalorimetry measurements give access to the adsorption enthalpies in liquid phase or more precisely to the enthalpies of displacement (cf. *Section II.3.1.a.*).

The experiments were carried out with a passive diathermal microcalorimeter ThermoMetri, TAM 2277 model (Thermal Activity Monitor) by David Bergé-Lefranc at Institut Méditerranéen de Biodiversité et d'Écologie marine et continentale (IMBE), Marseille. Measurements of the adsorption enthalpies were performed at 25°C by a step-by-step titration of suspensions of the different substrates (pristine and nanocomposites) by a stock solution. This analysis procedure was performed with a solution of R6G in ethanol. Integral enthalpies of adsorption were determined after correction of dilution effects.

The studied system (in the cell) exchanges heat with the thermostat. The term 'passive' means that there are no heaters in order to maintain temperature. The calorimeter comprises two cells, a reference one and the measurement one. These cells are maintained in a temperature imposed by thermostated bath with a large volume in order to increase thermal stability. The heat flow exchanges between the system and the thermostat. When the adsorption phenomenon occurs, the heat is transmitted to the thermostat via the thermocouples. The heat released during the adsorption or solvent displacement is measured and the calorimeter quickly returns to the initial temperature due to its high mass and thermal conductivity.

The schematic diagram of the measurement and thermopile principle is presented in **Figure D.1**.

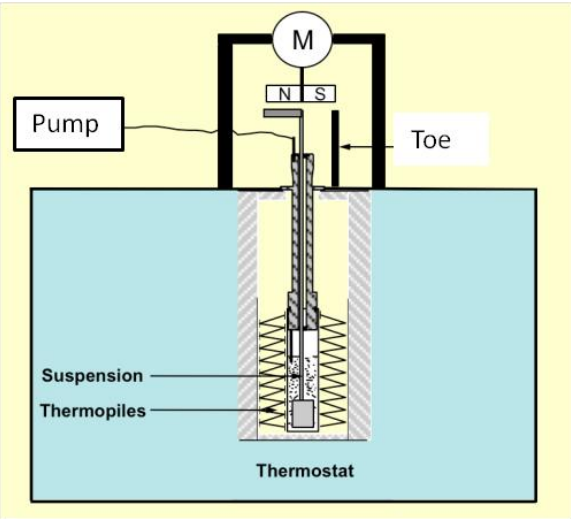

Figure D.1 Schematic diagram representing the measuring cell in the calorimeter. M represents the motor and NS is the magnet.

The setup used is an assembly in closed reactor stirred in a Tian-Calvet–type calorimeter. This means that the heat flow measurement is performed using thermocouples connected in series. These thermocouples are known as thermopiles. Thermocouples connected in series allow a temperature conversion into amplified voltage via a Seebeck effect (generation of a potential difference between two junctions of materials brought to different temperatures). The calorimeter constant used to determine thermal power. These thermopiles are connected in opposition, thereby it allow maintaining symmetry and cancelling external perturbations of thermal origin. The temperature difference between the two cells resulting from adsorption generates a potential difference, the measurement of this electromotive force as a function of time leads to the construction of a thermogram.

However, the heat measured through conduction via thermocouples represents only a portion of the heat dissipated. It is in fact free of those dissipated by convection and radiation. The calorimeter and cell architecture aims to minimize losses by radiation and convection. The measured heat flow (φ), resulting from the temperature difference between the interior of the cell and the thermostat, can be expressed in the form:

Equation D.1 $$\boldsymbol{\varphi = x_{\lambda} \times c \times \sum_{i=1}^{n} \Delta T_i}$$

Where: x_λ is the fraction of the heat flow transmitted by conduction

c is the thermal conductivity $[W.K^{-1}\ per\ unit\ of\ surface]$

ΔT_i $\Delta T_i = T_{cell} - T_{thermostat}$

In this case, the measured signal is not a heat flow since transfer surface is unknown; it is more strictly a thermal flow. Thermopiles are thermal flowmeter whose sensitivity can be expressed as $\mu V/\mu W$.

The voltage (V) of the thermocouples connected in series forming the thermopile can be calculated by summing the response of each thermocouple:

Equation D.2 $$\boldsymbol{V = S_0 \times \sum_{i=1}^{n} \Delta T_i}$$

Where: S_0 is the Seebeck coefficient

Note that S_0 is assumed to be common for all thermocouples forming the thermopile.

The relationship between the two terms of the thermal flow and the response of the thermopile constituting the calorimeter constant k can be expressed as:

Equation D.3 $$\boldsymbol{V = \frac{S_0}{x_{\lambda} \times c} \times \varphi = k \times \varphi}$$

The constant k specific in each calorimeter is determined by comparing the signal obtained from the known heat generated by Joule effect by means of a resistor. A calorimeter is also characterized by its time constant corresponding to the time of half return of the signal to baseline after discontinuation.

Reference and measurement cells are stainless steel cylinders; they have a thread for attaching to the agitation and liquid injection mechanisms. In the initial state, the measurement cell contains the solvent and the solid agitated. Stirring is provided by an electric motor which drives a magnet in a rotating motion. The stainless steel stirrer is driven in turn by the magnet and a abutment blocks the rotation causing a sudden return to its initial position. This type of agitation provides optimum dispersion of the solid and very low drift in the baseline because the magnetic transmission eliminates mechanical perturbations induced by the motor. The reference cell is charged only with the solvent. The solutions are injected into the cells via inox capillaries with a length of about 1.5 m. In calorimetric measurements, a condition to be met is to maintain symmetry between the two cells enabling elimination of any artifact measurement.

The cells placed in the calorimeter at 25°C can be disrupted by evaporation phenomena creating low thermal variations. To avoid this, a liquid injection is carried out also in the reference cell in order to always keep the system symmetrical. Injections in the two cells are made simultaneously at equal flow rates. The frequency of injection is controlled by a computer program controlling the two pumps.

E. Raman spectroscopy

The Raman experiments were performed using a Raman microspectrometer Horiba-Jobin-Yvon, LabRAM, model HR800 with the help of Cédric Pardanaud at Laboratoire de Physique des Interactions Ioniques et Moléculaires (PIIM), Marseille. **Figure E.1** presents the principle of a conventional Raman microspectrometer [12]. The experiments were performed with a laser wavelength (λ_L) of 632.8 nm (~633 nm) or 514.5 nm (~514 nm); with a 50× objective; the numerical aperture was of 0.5 leading to a lateral resolution of ~1 µm and a spectroscopic resolution ~1 cm^{-1}. The measurements at ~405 nm were performed by Jean-Luc Bruneel at Institut des Sciences Moléculaires (ISM), Bordeaux.

Spectra presented in this work are mean spectra made of 16 spectra, each recorded during 25 s. Raman spectra were recorded on different grains to check the homogeneity of adsorbed R6G at the grains scale.

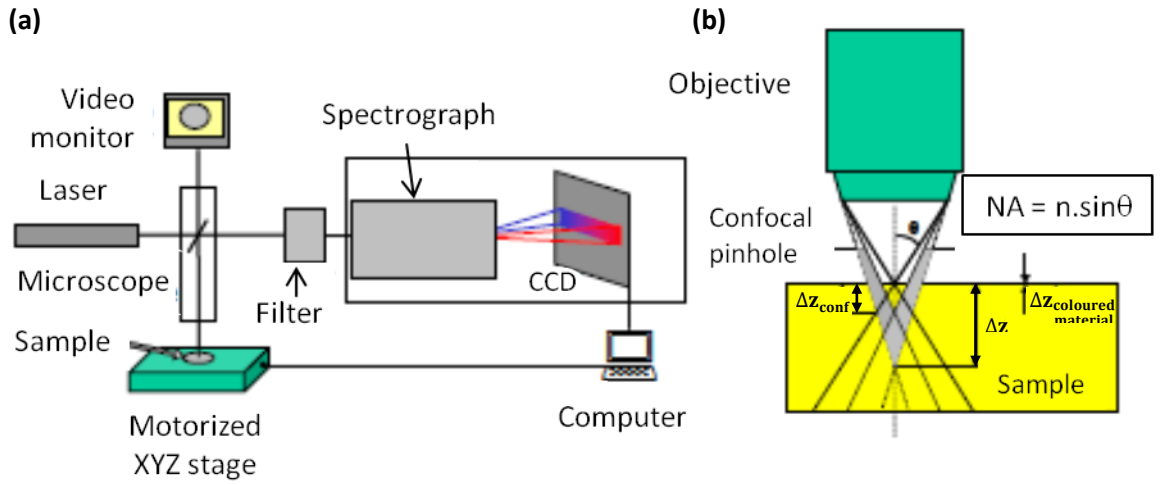

Figure E.1: Principle of a conventional micro-Raman spectrometer (a) and Observation of a sample through a microscope (NA: Numerical Aperture; n: refractive index of the medium separating the objective from the sample). A confocal hole rejects the shadowed light and facilitates a more accurate in-depth analysis ($\Delta z_{conf} < \Delta z$) (b). Adapted from [12].

The laser power is close to 10 mW. μm^{-2}. This power density has a small effect on the baseline intensity caused by absorption–photoluminescence processes that are not discussed here. But it has no effects on the molecular spectroscopic signatures intensity that are of interest here.

F. Low temperature adsorption microcalorimetry coupled with manometry

The low temperature adsorption microcalorimetry was applied to investigate the hydrogen adsorption properties of the studied materials: adsorption isotherm and related enthalpies of adsorption.

The microcalorimetric measurements were carried out at 77 K with pressures up to 0.8 bars in a built-in-house apparatus consisting of a Tian-Calvet–type isothermal microcalorimeter coupled with a manometric device (**Figure F.1**), at Laboratoire Matériaux Divisés, Interfaces, Réactivité, Électrochimie (MADIREL), Marseille. Prior to adsorption measurement, the samples ($\sim 300 - 400$ mg) were degassed overnight at 150°C under vacuum pressure $\sim 1\ 10^{-2}$ mbars for the removal of all physisorbed species. The weight of samples was determined before and after activation.

This technique was used within this work in one hand for determining the amount of hydrogen adsorbed on the porous solids studied, i.e. Ni-based nanocomposites and on the other hand for measuring the adsorption enthalpies for reference materials, unconfined particles synthesized and nanocomposites.

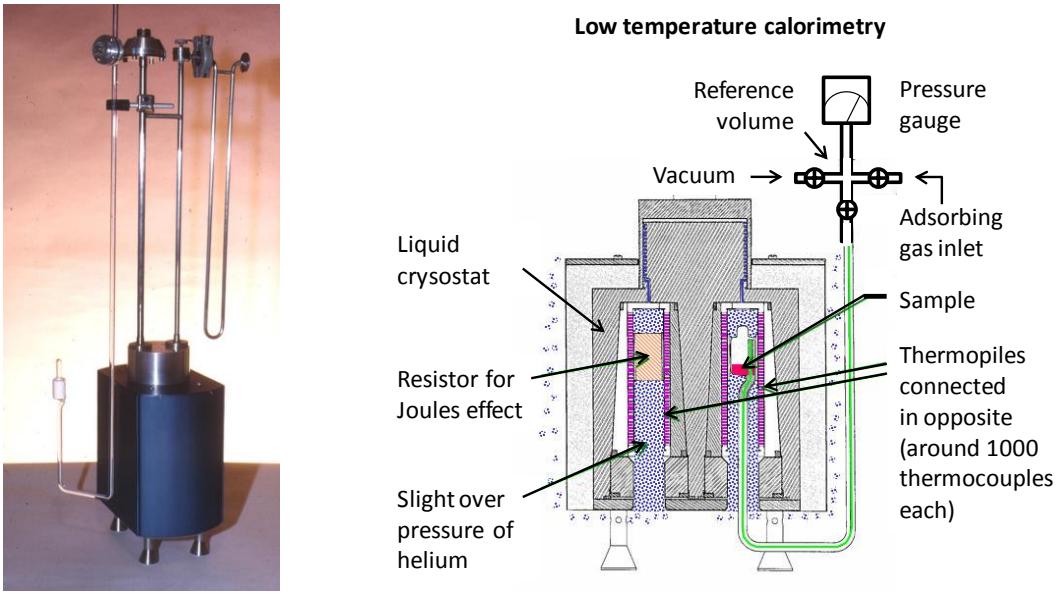

Figure F.1: Tian-Calvet–type microcalorimeter coupled with a manometer (built-in-house).

G. Reduction in gas phase

The reduction in gas phase of the metal precursors (confined or unconfined) into metal nanoparticles was performed using a built-in-house apparatus, presented on **Figure G.1**, at Laboratoire Matériaux Divisés, Interfaces, Réactivité, Électrochimie (MADIREL), Marseille. The reducing gas chosen within this work was hydrogen. Prior to the reduction process, the samples were degassed at room temperature then purged with an argon/hydrogen (95/5 molar ratio) mixture to ensure purity of the atmosphere in the reduction system. Finally, the metal precursors were treated under the same Ar/H_2 atmosphere used for the purge at specific temperatures and heating rates.

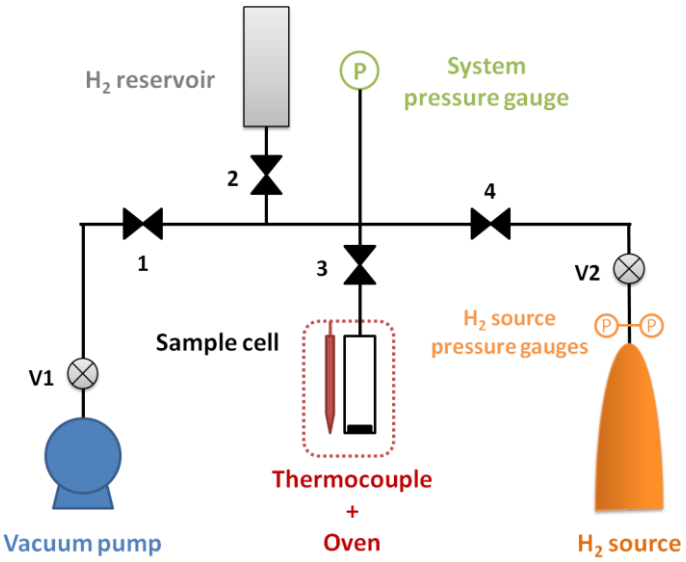

Figure G.1: Schematic diagram of the reduction treatment system (built-in-house).

References

[1] H.E. Taylor, *Inductively Coupled Plasma-Mass Spectrometry: Practices and Techniques*., Academic Press: San Diego, (2000).

[2] F. Rouquerol, J. Rouquerol, K.S.W. Sing, *Adsorption by Powders and Porous Solids: Principles, Methodology and Applications*, First Ed., Academic Press: London, (1999).

[3] (a) A.V. Neimark, P.L. Ravikovitch, *Langmuir*, 19 (1997) 5148. (b) K. Murata, M. El-Merraoui, K. Kaneko, *J. Chem. Phys*., 114 (2000) 4196.

[4] K.S.W. Sing, D.H. Everett, R.A.W. Haul, et al., *Pure Appl. Chem.*, 57 (1985) 603.

[5] S. Brunauer, L.S. Deming, W.E. Deming, et al., *J. Am. Chem. Soc.*, 62 (1940) 1723.

[6] J. Rouquerol, D. Avnir, C.W. Fairbridge, et al., *Pure Appl. Chem.*, 66 (1994) 1739.

[7] F. Rouquerol, L. Luciani, P.L. Llewellyn, R. Denoyel, J. Rouquerol, 'Texture des matériaux pulvérulents ou poreux' in *Techniques de l'Ingénieur, traité Analyse et Caractérisation*, (2003) pp. 1050-1–1050-24.

[8] C. Sangwichien, G.L. Aranovich, M.D. Donohue, *Colloid Surf., A*, 206 (2002) 313.

[9] E.P. Barrett, L.G. Joyner, P.P. Halenda, *J. Am. Chem. Soc.*, 73 (1951) 373.

[10] J.H. de Boer, B.C. Lippens, B.G. Linsen, et al., *J. Colloid Interface Sci.*, 21 (1966) 405.

[11] D. Bergé-Lefranc, Thesis : 'Élimination de toxines urémiques par adsorption sur des matériaux zéolitiques', Aix-Marseille Université, 2006, pp. 47–50.

[12] G. Gouadec, P. Colomban, *Prog. Cryst. Growth Charact. Mater.*, 53 (2007) 1.

Index of figures

Introduction

Chapter 1

Chapter 2

Chapter 3

Appendices

Appendix B

Appendix D

Appendix E

Appendix F

Appendix G

Index of tables

Chapter 1

Chapter 2

Chapter 3